Velocity Fluctuation, Correlation and Rheology in Frictional Granular Shear Flow

A Thesis
Submitted for the Degree of
MASTER OF SCIENCE (ENGINEERING)

by

Bishakhdatta Gayen

ENGINEERING MECHANICS UNIT
JAWAHARLAL NEHRU CENTRE FOR ADVANCED SCIENTIFIC RESEARCH
(A Deemed University)
Bangalore – 560 064

JANUARY 2008

To my parents and the God

DECLARATION

I hereby declare that the matter embodied in the thesis entitled "**Velocity Fluctuation, Correlation and Rheology in Frictional Granular Shear Flow** " is the result of investigations carried out by me at the Engineering Mechanics Unit, Jawaharlal Nehru Centre for Advanced Scientific Research, Bangalore, India under the supervision of Dr. Meheboob Alam and that it has not been submitted elsewhere for the award of any degree or diploma.

In keeping with the general practice in reporting scientific observations, due acknowledgment has been made whenever the work described is based on the findings of other investigators.

Bishakhdatta Gayen

CERTIFICATE

I hereby certify that the matter embodied in this thesis entitled "**Velocity Fluctuation, Correlation and Rheology in Frictional Granular Shear Flow** " has been carried out by Mr. **Bishakhdatta Gayen** at the Engineering Mechanics Unit, Jawaharlal Nehru Centre for Advanced Scientific Research, Bangalore, India under my supervision and that it has not been submitted elsewhere for the award of any degree or diploma.

Dr. Meheboob Alam
(Research Supervisor)

Acknowledgments

I am indebted to Dr. Meheboob Alam for his guidance and patience at every stage of this work, and indeed for teaching me what research is all about. I am fortunate to have him as my research advisor.

I am thankfull to all other faculties of Engineering Mechanics Unit (EMU) in JNCASR for their help and guidance from time to time.

I am very fortunate to have friends like Devranjan, Ashish, Rajaram, Vijay and Priyanka.

I really had good time with with Devranjan and Dhiraj being their room partners. I am also thankful to Harish (poster award winner) and Rajapandian (poster award winner) for valuable discussions. I am gratefull to Onubhab, Kaushik, Ratul, Gayatri, Pinaki, Vivekanand in EMU.

I also thankful to my juniors Sriharsha, Chandrashekar, Vikek Prakash, Snehalata from EMU and Piyush, Soumik, Vibhash, Nisha, Urmimala from CPMU for their company and help during my last few weeks in JNCASR.

Last but not the least I espeacially thank Vini for her moral support during my entire thesis writing work due to which I was able to finish my writing work with in limited time.

List of Publications

1. B.Gayen and M. Alam, Orientational correlation and velocity distributions in a sheared rough dilute granular gas, (Physical Review Letters, 2008, In press)

Abstract

The study of granular materials has received a recent upsurge of interest in physics. This has been motivated by both the relevance of such flows to a wide range of industrial and geological processes, and by the realization that granular materials provide an excellent test bed for a number of fundamental questions in the context of modern fluid dynamics and nonequlibrium statistical mechanics. Most of the theories of granular fluid are based on the Boltzmann or Enskog-Boltzmann equation of inelastic hard spheres. In this regard particle dynamics simulations make a bridge between theory and experiment.

An event-driven molecular dynamics code has been developed which is based on the paper of Lubachevsky (1991) and the book by Rapaport (1995). The computational approach employed in this study mainly consists of initialization, bookkeeping and diagnostic parts. This code is very fast and can handle a large number of particles ($N \sim 10^6$) and has been generalized to three dimensions. It can be used to simulate various kind of plane granular flows (Couette flow, Poiseuille flow, Chute flow, etc.) with rough, frictional particles. For the simplest model of rough, inelastic spheres, two material parameters are needed to characterize the collision process: the normal coefficient of restitution, e, and the tangential coefficient of restitution, β. For a more realistic collision model of rough particles, we have taken into account the effect of Coulomb friction which helps to distinguish between the sliding and the rolling contacts, resulting in a contact-angle (γ) dependent tangential restitution coefficient $\beta(\gamma)$.

With the above code, we have probed various microscopic and macroscopic propreties of unbounded granular shear flow for which a steady linear velocity profile is applied with a constant velocity gradient via shifting the replica images of top and bottom boundaries without deforming the box (Lees-Edwards boundary condition). This code has been tested for bounded shear flow too for which

physical boundaries are required: wall-particle interactions are modeled using the same collision dynamics of particle-particle interaction. For either case, the system is allowed to reach a 'non-equilibrium' steady-state condition by monitoring the temporal evolution of system's kinetic energy.

In this work we have thoroughly examined the effects of particle roughness and rotation on the probability distributions of fluctuating translational and rotational velocities as well as density and spatial velocity correlations in the Boltzmann limit (for which the particle volume fraction, ϕ, is close to zero) of unbounded shear flow. We found that both translational and rotational velocity distribution functions (VDF) are non-Gaussian with stretched exponential tails, except in the limiting cases of perfectly smooth ($\beta = -1$) and rough ($\beta = 1$) particles with elastic collisions ($e = 1$). One important finding is that the translational and rotational velocities are *correlated in direction*. Particle roughness has important effects on orientational and velocity correlations even when the collisions are perfectly elastic ($e = 1$) and the system is homogeneous. Orientational and spatial velociy correlation are responsible for non-Gaussian distributions of translational and rotational velocities.

With increasing system density, the dissipation-induced density inhomogeneity is observed over the whole domain. A pronounced asymmetry about the mean value is observed for the probability distributions of local density, local shear rate and local spanwise rotational velocity. Therefore the calculation of "local" VDF is a proper way to study such inhomogeneous systems. For a moderately dense system ($\phi = 0.3$), an interesting phenomenon is observed for the local VDF of streamwise translational velocity: its tails undergo a transition from an stretched exponential to an under-populated Gaussian distribution with decreasing dissipation and finally to a Gaussian for no dissipation. The VDF of spanwise rotational velocity makes a transition from stretched exponential tails to a Gaussian with decreasing dissipation. For the dense system ($\phi = 0.5$) with dissipation, the VDF for streamwise translational velocity is a Gaussian with under-populated tails. The effect of Coulomb friction on VDFs has been studied for different values of friction coefficient μ for $\phi = 0.3$ with the critical roughness being set to $\beta_0 = 0$. With the incorporation of Coulomb friction, a pronounced asymmetry of the tails of the VDFs of rotational velocities is seen and the skewness of the distribution increases with increasing dissipation.

Lastly, we have calculated some rheologoical properties of unbounded shear flow of rough, frictional particles. Our simulations results on pressure and shear viscosity compare well with the predictions of Lun's (1991) rheological model at small dissipations. The model predictions deteriorate with increasing dissipation which is tied to the inherent assumptions of the underlying model which is valid for quasi-elastic ($e \sim 1$) particles in the prefectly smooth and rough ($|\beta| \sim 1$) limits. Our results on normal stress differences ($\mathcal{N}_1$ and $\mathcal{N}_2$) suggest that a non-Newtonian constitutive model is required for moderately dissipative rough, frictional particles.

List of Figures

Contents

Chapter 1

INTRODUCTION

During the last two decades, much work has been devoted to understanding the rheology (Savage (1984); Campbell (1990); Hutter & Rajagopal (1994)) and, more recently, the dynamics of granular materials (see, for reviews, Jaeger *et al.* (1996); Herrmann *et al.* (1998); Kadanoff (1999); Goldhirsch (2003), Aranson & Tsimring (2006)). In the rapid flow regime in which the particles move around randomly, interacting mainly via instantaneous *dissipative* collisions with negligible interstitial fluid effects, the granular material has been modelled as a system of smooth inelastic hard spheres. The standard statistical mechanical tools of the kinetic theory of dense gases have been modified to develop appropriate rheological models for a continuum description of such fluidized granular materials (Lun *et al.* (1984); Jenkins & Richman (1985); Goldshtein & Shapiro (1995); Sela & Goldhirsch (1998); Montanero *et al.* (1999); Garzo & Dufty (1999)). If the particles are "smooth", their collisions can be characterized by a single parameter , the normal restitution coefficient (e), with the limiting case of $e = 1$ being tied with elastic collisions and no energy loss. It is now well-known that this "added" inelasticity is a source of many interesting and unresolved phenomena in granular flows: clustering (Hopkins & Louge (1991), Goldhirsch & Zanetti (1993), Tan & Goldhirsch (1997), Alam & Nott (1997),Mikkelson *et al.* (2002)); waves and patterns (Forterre & Pouliquen (2002), Conway & Glasser (2004), Alam & Luding (2005), Alam (2006), Aranson & Tsimring (2006)); oscillons (Umbanhowar *et al.* (1996)); segregation and Brazil-nut phenomenon (Rosato *et al.* (1987), Ottino & Khakhar (2000), Möbius *et al.* (2001), Hong *et al.* (2001), Alam *et al.* (2006), Reis & Mullin (2004), Burtally *et al.* (2002)); non-Gaussian velocity fluctuations (Losert *et al.* (1999), Moon *et al.* (2004)).

Real particles are always characterized by some degrees of "roughness", giving rise to surface friction. Consequently, the rotational motion becomes important to deal with rough, frictional particles. Even in the limit of nearly inelastic particles

($e \approx 1$), the added complexity of the rotational motion gives rise to additional hydrodynamics fields: the spin/rotational velocities and the rotational granular temperature (Condiff & Dahler (1964); Theodosopulu & Dahler (1974) ; Dahler & Theodosopulu (1974); Jenkins & Richman (1985); Lun & Savage (1987); Lun (1991); Luding *et al.* (1998*a*); Mirarai *et al.* (2002); Hayakawa (2001); Goldhirsch *et al.* (2005)). It turns out that the translational and rotational temperatures of a granular fluid are not equally partitioned (Lun & Savage (1987); Lun (1991); Huthmann & Zippelius (1997*a*) ; McNamara & Luding (1998)), except in perfect rough limit. More importantly, at finite densities , there is an additional contribution to the stress tensor that renders it "asymmetric"- a signature of the "micropolar" theory (Condiff & Dahler (1964); Kanatani (1979); Mirarai *et al.* (2002)). Another new ingredient associated with rotational motion is the transport via the "couple" stress (i.e. the flux of angular momentum) which becomes important in the presence of boundaries. The implications of the additional hydrodynamics fields, the energy non-equipartition, the asymmetric stress tensor and the couple stress on the dynamical behavior of a granular fluid are not known a *priori*, and have not been investigated rigorously for a driven system.

The molecular dynamics (MD) simulation work of Moon *et al.* (2004) has elucidated the role of friction on pattern formation in oscillated granular layers. They found that while the squire, stripe and hexagonal patterns are stable for frictional particles (that match with experimental results), only the stripe-pattern is stable for frictionless particles. Certain experimental phenomena (e.g. the parametric sloshing of particles, the shock-wave formation, etc.) also occur in MD simulations with and without friction, but there are important differences in the details of these phenomena. There has been some work on the 'rotationally-driven' granular fluid (Cafiero *et al.* (2002); Luding *et al.* (2003)). These authors showed that a granular fluid can be made spatially homogeneous even at very high dissipation levels by transferring energy from the rotational degrees of freedom to their translational counterpart, even though its (translational) velocity distribution function shows large deviations from a Gaussian. They also explained some recent experimental results (see, for details, Luding *et al.* (2003)) by driving on both the translational and the rotational degrees of freedom. The consensus that emerges from the above discussion is that the rotational motion should not be neglected for a realistic modelling of dynamics and pattern formation in granular media even in the dilute limit.

To develop constitutive models of rough granular gases, a systematic study of correlations and the distribution functions of both 'translational' and 'rotational' fluctuating velocities is of fundamental interest. While the deviation of translational velocity distribution functions (VDF) from a Gaussian has been extensively studied using theory (Esipov & Pöschel (1997)), van Noije & Ernst (1998)), Goldhirsch & Tan (1996)), simulation (Cafiero *et al.* (2000), Moon *et al.* (2004)a) and experiment (Losert *et al.* (1999); Rouyer & Menon (2000)), similar results on 'rotational' VDFs are very scarce. The high-velocity tails of translational VDFs have been characterized in terms of stretched exponentials or power-laws (Moka & Nott (2005); Vijaykumar & Alam (2007)).

For a rough granular gas, one needs to probe possible 'orientational' correlations between translation and rotation (Brilliantov *et al.* (2007)), in addition to standard density and velocity correlations. It has been recently established (Brilliantov *et al.* (2007)) that such orientational/directional correlations are strong and the limit of smooth granular gas is *singular* in a heated granular gas. The last result readily raises doubts about the validity of the hydrodynamic theories (Goldhirsch *et al.* (2005)) that are built on Chapman-Enskog-type perturbation expansions around the "smooth" limit of vanishing roughness.

The present thesis deals with particle dynamics simulations of frictional granular materials. The first part of this thesis is to develop an efficient event-driven code to simulate three dimensional plane granular flows (Couette flow, Poiseuille flow, Chute flow, etc.). The rest of the thesis deals with probing various microscopic(velocity fluctuations, correlations, etc) and macroscopic (rheology) properties of unbounded granular shear flow.The collision model for this work is the well known inelastic hard-sphere model that incorporates particle surface roughness and Coulomb friction.

1.1 Organisation of thesis

Chapter 2

In this chapter we start our work with modelling the rough granular particles and their collision dynamics based on both constant-β and variable-β models. Then we discuss about our developed code on the basis of the algorithm given by Lubachevsky (1991) and Rapaport (1995) for both unbounded and bounded granular shear flows. Finally, we will highlight on the method of averaging, followed by validation of our code.

Chapter 3

All results in this chapter are taken for a dilute system (with a particle volume fraction $\phi = 0.01$), well known as the Boltzmann limit. We calculate velocity distribution functions (VDFs) for both translational and rotational velocities over a wide range of normal and tangential restitution coefficients. Then we study the pair and velocity correlation functions and the effect of particle surface roughness on correlation functions. We end this chapter by studying possible "orientational" correlation between translational and rotational velocities.

Chapter 4

The effects of system density (non-Boltzmann limit) on VDFs, density and velocity correlations are studied in this chapter. Here we work on moderately dense and dense granular flows having particle volume fractions of $\phi = 0.3$ and 0.5. The effect of Coulomb friction on various microscopic properties is studied for a system with $\phi = 0.3$. Related results for a system density of $\phi = 0.1$ are shown in Appendix I. The results on density and velocity correlations are shown in Appendix II.

Chapter 5

In this chapter, various rheological quantities like pressure, shear stress, shear viscosity and normal stress differences ($\mathcal{N}_1, \mathcal{N}_2$) are computed and compared with the theoretical prediction given by Lun (1991). The effect of particle roughness and Coulomb friction on normal stress differences are studied in detail.

Chapter 2

COLLISION MODEL AND SIMULATION METHOD

In this chapter, we describe the collision model and the simulation methodology. Our simulation is based on inelastic hard spheres for which the interaction potential $\phi(r)$ is purely repulsive:

$$\phi(r) = \begin{cases} \infty & r < d \\ 0 & r \leq d \end{cases} \tag{2.1}$$

where d is the diameter of the hard sphere. In the absence of any external force, the particles move in straight lines at a constant speed between collisions and change their velocities immediately when a collision occurs. This means that the collisions are instantaneous and the impulsive force comes in the picture at the moment of their collision at the contact point.

2.1 Collision Model for Rough Particles

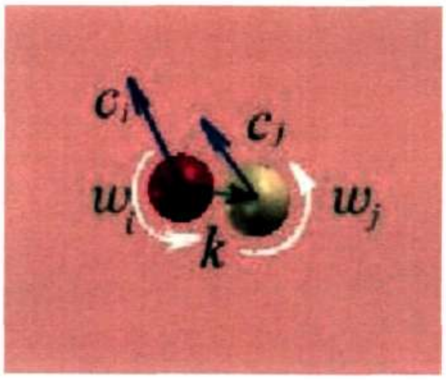

Figure 2.1: Schematic diagram of two particles just before collision

We consider a monodisperse system of rough, inelastic spheres of size d, mass

m, and the moment of inertia I, interacting via hard-sphere potential. The *pre-collisional* translational and angular velocities of particle i are denoted by $\mathbf{c}_i$ and ω_i, respectively, and the corresponding *post-collisional* velocities are denoted by the primed symbols, $\mathbf{c}_i'$ and ω_i'. Let $\mathbf{k}_{ij} = \mathbf{z}_j - \mathbf{z}_i = \mathbf{k}$ be the unit vector directed from the center of the i-th particle to that of j-th particle. The total pre-collisional relative velocity at contact, $\mathbf{g}_{ij}$, between particle i and j is given by

$$\mathbf{g}_{ij} = \mathbf{c}_{ij} - \frac{1}{2}d\mathbf{k}\times(\omega_i + \omega_j), \tag{2.2}$$

where $\mathbf{c}_{ij} = \mathbf{c}_i - \mathbf{c}_j$ is the translational velocity of particle i relative to j,

2.1.1 Constant-β model

For the simplest model of rough, inelastic spheres, two material parameters are needed to characterize the collision process (Lun & Savage (1987),Lun (1991),Gayen & Alam (2006)): the normal coefficient of restitution, e, and the tangential coefficient of restitution, β. The former is an indicator of the inelasticity of a particle and the latter an indicator of its surface roughness. The pre- and post-collisional velocities of the colliding particles are related via the following expressions:

$$\mathbf{k}\cdot\mathbf{g}_{ij}' = -e(\mathbf{k}\cdot\mathbf{g}_{ij}), \quad \mathbf{k}\times\mathbf{g}_{ij}' = -\beta(\mathbf{k}\times\mathbf{g}_{ij}) \tag{2.3}$$

In general, $0 \le e \le 1$ and $-1 \le \beta \le 1$. For collisions between perfectly smooth particles $\beta = -1$, with increasing value of β being an indicator of the increasing degrees of particle surface friction. The value of $\beta = 0$ represent the case for which the particle surface friction and inelasticity are sufficient to eliminate the post-collisional tangential relative velocities. For $0 < \beta \le 1$, the *spin-reversal* occurs after a collision (Maw *et al.* (1981)), and the case of $\beta = 1$ corresponds to the collision between perfectly rough particles.

From the conservation laws of linear and angular momemtum, the relationship between pre- and post-collisional velocities can be written as

$$\begin{aligned} m\left(\mathbf{c}_i - \mathbf{c}_i'\right) &= m\left(\mathbf{c}_j' - \mathbf{c}_j\right) = \mathbf{J}, && (2.4)\\ I\left(\omega_i' - \omega_i\right) &= I\left(\omega_j' - \omega_j\right) = -\frac{1}{2}d\left(\mathbf{k}\times\mathbf{J}\right), && (2.5) \end{aligned}$$

with $i \neq j$ and the collisional impulse is given by

$$\mathbf{J} = m\eta_2 \mathbf{g}_{ij} + m\,(\eta_1 - \eta_2)\,\mathbf{k}\,(\mathbf{k}\cdot\mathbf{g}_{ij})\,, \tag{2.6}$$

with

$$\eta_1 = \frac{1}{2}(1+e),\;\; \eta_2 = \frac{1}{2}(1+\beta)/K(1+K),\;\; K = 4I/(md^2) \tag{2.7}$$

Here K is the nondimensional moment of inertia of a particle: $K = 2/5$ for solid spheres, $2/3$ for a thin-shell sphere (i.e. the mass m is uniformly distributed over its surface), and 0 when the mass m is concentrated at the centre of the sphere (i.e. for point particles).

2.1.2 Coulomb Friction: Variable-β model

For a more realistic collision model of rough particles, we have taken into account the effect of Coulomb friction which helps to distinguish between the sliding and the rolling contacts (Maw *et al.* (1981) ;Walton (1993); Luding *et al.* (1998*b*); Jenkins & Zhang (2002);Goldhirsch *et al.* (2005)). Coulomb's law connects the normal and tangential forces at contact. If the tangential impulse is less than the product of the friction coefficient and the normal impulse, i.e., $|\mathbf{k}\times\mathbf{J}| < \mu\,|\mathbf{k}\cdot J|$, the sticking contact occurs, where μ is the coefficient of friction. The surface tangential velocity is written as

$$\mathbf{k}\times\mathbf{g}'_{ij} = -\beta_0\,(\mathbf{k}\times\mathbf{g}_{ij}) \tag{2.8}$$

where β_0 is a phenomenological constant, characterising the restitution of velocity in the tangential direction for sticking contacts, with $-1 \leq \beta_0 \leq 1$. From the experimental data of Maw *et al.* (1981), Lun and Bent (1994) found that the values of β_0 and μ for the commercial ball bearings are 0.4 and 0.123, respectively. Foerster *et al.* (1994) did some experiments with glass particles for which $\beta_0 = 0.44$ and $\mu = 0.09$.

When the tangential impulse is greater or equal to the product of the friction coefficient and the normal impulse, the sliding contact occurs and the following equality holds:

$$|\mathbf{k}\times\mathbf{J}| = \mu\,|\mathbf{k}\cdot\mathbf{J}|\,. \tag{2.9}$$

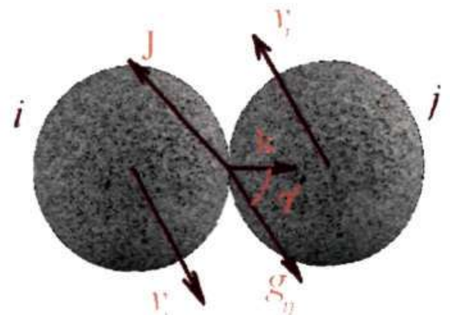

Figure 2.2: Schematic picture of the velocities of two colliding particles at contact

From (2.6) and (2.9), the tangential coefficient of restitution can be found explicitly as

$$\beta = -1 + \mu(1+e)\left(1 + \frac{1}{K}\right)\frac{|\mathbf{k}\cdot\mathbf{g}_{ij}|}{|\mathbf{k}\times\mathbf{g}_{ij}|}. \tag{2.10}$$

This can be rewritten in terms of the impact angle which is defined as the angle between the contact vector $\mathbf{k}$ and the relative velocity at the contact of two particles, as shown in figure 2.2:

$$\beta = -1 + \mu(1+e)\left(1 + \frac{1}{K}\right) cot\gamma. \tag{2.11}$$

It follows from figure 2.2, $0 \le \gamma \le \pi/2$. Let us define a critical angle γ_0 such that when $\gamma > \gamma_0$ there is sliding (Coulomb friction) during a collision and when $\gamma \le \gamma_0$ there is sticking (or the particles are 'rough'); at $\gamma = \gamma_0$, $\beta = \beta_0$. The critical angle is given by

$$cot\gamma_0 = \frac{K(1+\beta_0)}{\mu(1+e)(1+K)} \tag{2.12}$$

For simulations the value of β is taken from $\beta(\gamma)$ and β_0 :

$$\beta(\gamma) = min\left\{\beta_0, -1 + \mu(1+e)\left(1 + \frac{1}{K}\right) cot\gamma\right\}. \tag{2.13}$$

This collision angle dependent model will henceforth be referred to as "variable-β" model.

2.1.3 Wall-Particle Collision Model

When a particle collides with a wall we assume it collides with a rough surface of infinite mass. As the walls are rough, particle's tangential as well as rotational velocity change after the collision. We use e_w and β_w to denote normal and tangential restitution coefficients for particle-wall interactions. The collision rule for constant-β_w model is:

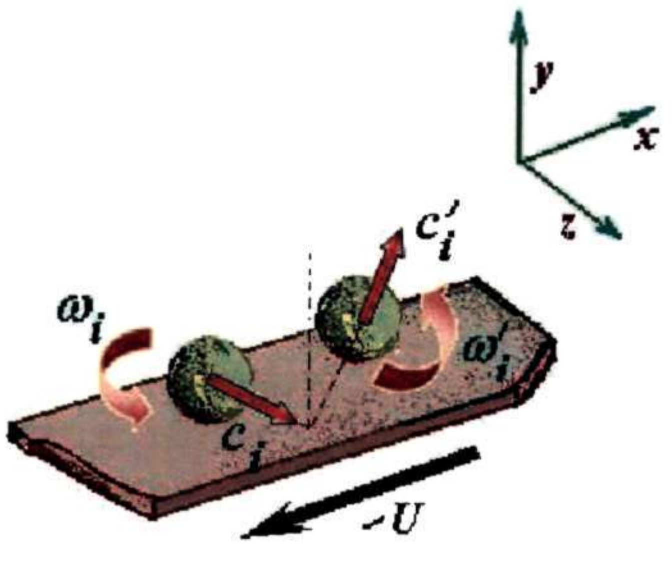

Figure 2.3: Close view of wall collision for ith particle

$$\mathbf{n_y}\cdot\mathbf{g}^{w\prime}_{i} = -e_w(\mathbf{n_y}\cdot\mathbf{g}_i^w), \;\; \mathbf{n_y}\times\mathbf{g}^{w\prime}_{i} = -\beta_w(\mathbf{n_y}\times\mathbf{g}_i^w), \tag{2.14}$$

Here the unit vector can easily be found from figure 2.3 (see also figure 2.11) as $\mathbf{n_y}$ and $-\mathbf{n_y}$ when the particle interaction is with upper and lower walls, respectively; $\mathbf{g_i^w}$ and $\mathbf{g_i'^w}$ are, respectively, the pre-collisional and post-collisional relative velocity at wall-particle contact. Similarly, we can obtain an expression for wall-particle impulse:

$$m\left(\mathbf{c}_i - \mathbf{c}_i'\right) = \mathbf{J_w},\;\; I\left(\omega_i' - \omega_i\right) = -\frac{1}{2}d\left(\mathbf{n}_y \times \mathbf{J_w}\right), \tag{2.15}$$

and

$$\mathbf{J_w} = 2m\eta_2^w \mathbf{g}_i^w + 2m\left(\eta_1^w - \eta_2^w\right)\mathbf{k}\left(\mathbf{k}\cdot\mathbf{g}_i^w\right), \tag{2.16}$$

where $\mathbf{J_w}$ is the impulse for wall-particle collision and

$$\eta_1^w = \frac{1}{2}(1+e_w),\;\; \eta_2^w = \frac{1}{2}(1+\beta_w)/K(1+K). \tag{2.17}$$

For a realistic model of wall-particle collision, we take into account Coulomb friction. Here β_0^w and μ_0^w represent the collisional properties for wall-particle interaction. Similarly, as before the unit vector must be replaced by $\mathbf{n_y}$ and $-\mathbf{n_y}$ when the particle interaction is with upper and lower walls, respectively. We define γ^w and γ_0^w as the impact angle and the critical angle for wall-particle interaction. If the tangential impulse is less than the product of the friction coefficient and the normal impulse, i.e., $|\mathbf{n_y}\times\mathbf{J}_w| < \mu_w\,|\mathbf{n_y}\cdot\mathbf{J_w}|$, the sticking contact occurs for which the surface tangential velocity is

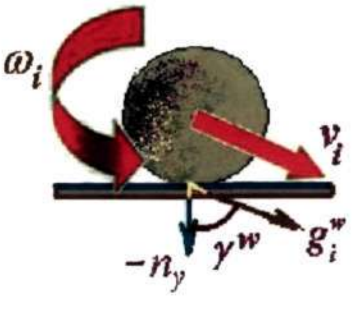

Figure 2.4: Schematic picture of the velocity of a colliding particle at wall

$$\mathbf{n_y}\times\mathbf{g}^{w\prime}_{i} = -\beta_0^w \left(\mathbf{n_y}\times\mathbf{g}_i^w\right). \tag{2.18}$$

When the tangential impulse is greater or equal to the product of the friction coefficient and the normal impulse, sliding contact occurs and the following equality holds:

$$|\mathbf{n_y}\times\mathbf{J}_w| = \mu_w\, |\mathbf{n_y}\cdot\mathbf{J}_w|\,. \tag{2.19}$$

From (2.16) and (2.19), the tangential coefficient of restitution can be found explicitly as

$$\beta_w \;=\; -1+\mu_w(1+e_w)\left(1+\frac{1}{K}\right)cot(\gamma^w). \tag{2.20}$$

From figure 2.4 the range of γ^w is defined as: $0 \leq \gamma^w \leq \pi/2$. As in particle-particle interaction, a critical angle γ_0 is defined such that when $\gamma^w > \gamma_0^w$ there is sliding (Coulomb friction) during collision, when $\gamma^w \leq \gamma_0^w$ there is sticking; at $\gamma^w = \gamma_0^w$, $\beta_w = \beta_0^w$. For simulations the value of β^w is taken from $\beta_w(\gamma^w)$ and β_0^w:

$$\beta_w(\gamma^w) = min\left\{\beta_0^w, -1+\mu_w(1+e_w)\left(1+\frac{1}{K}\right)cot(\gamma^w)\right\}. \tag{2.21}$$

2.2 Algorithm for Event-Driven Simulation

2.2.1 Algorithm: Unbounded Shear Flow

The computational approach employed in this study mainly consists of initialization, book-keeping and diagnostic parts. The present algorithm is based on the paper of Lubachevsky (1991) and the book by Rapaport (1995). In the first part, the positions of particles are initialized in a control volume of specific dimension. Their translational and rotational velocities are taken from a Gaussian distribution randomly. The average initial velocity is set to zero for both velocities. The outline of the algorithm is provided below (Lubachevsky (1991)) followed by discussions.

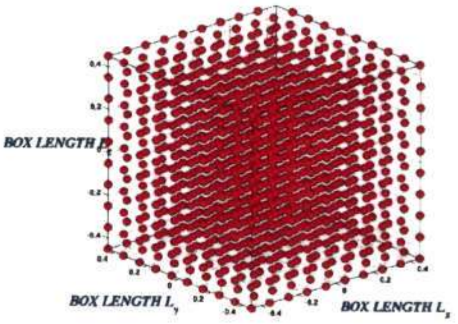

Figure 2.5: Initially particles are placed in a 3D box

Initialisation

$timenow = 0$;
$endtime =$ timbig;
$Ndim \quad = 3$;

$$\left.\begin{array}{ll} new(i) & \leftarrow 1 \\ old(i) & \leftarrow 2 \\ time[i,1] & \leftarrow 0 \\ partnr[i,1] & \leftarrow \Lambda \\ state[i,1] & \leftarrow \text{initial state of } i \text{ th component} \end{array}\right\}_{i=1\forall N}$$

```
while timenow < endtime do {
  timenow ← $min\,[time\,[i, new[i]]]_{1 \le i \le N}$
    $i^*$ ← index for minimum time (i.e. timenow)
  $jj$ ← partnr[$i^*, new[i^*]$]
  if { $jj > 0$ then /"state update required"/ ;
    state1 ← advance($state\,[i^*, old[i^*]]\,, time\,[i^*, old[i^*]]\,, time\,[i^*, new[i^*]]$) ;
    $state\,[i^*, new[i^*]] \leftarrow cellcrossing\,[state1]$;
    if cellcrossing in boundary special treatment for $state\,[i^*, new[i^*]]$ ;
    if {$1 \le jj \le N$ /" two-component interaction"/
      stat2 ← advance($state\,[jj, old[jj]]\,, time\,[jj, old[jj]]\,, time\,[jj, new[jj]]$) ;
      $(state\,[i^*, new[i^*]]\,, state\,[jj, new[jj]]) \leftarrow processcollision\,[state1, state2]$
```

```
        $partnr\,[jj, new[jj]] \leftarrow -i^*$ /" no update for $jj$ "/ ;
        $new[jj] \leftarrow old[jj]; old[jj] \leftarrow 3 - new[jj]$ ;
      } /" end two-component interaction"/ ;
    $new[jj] \leftarrow old[i^*]; old[i^*] \leftarrow 3 - new[i^*]$ ;
  } /"end state update required clause"/ ;
  call for predictevent /" to get the value P and Q /"
    $P \leftarrow min_{j \in A(i^*)} P_{i^*j},\ where A(i^*) = \{1 \le i \le N, j \ne i^*,$
    $time\,[j, new[j]] \ge P_{i^*j}\}$;
    if$P < +\infty$ then$jj$ $\leftarrow$an index which supplies this minimum (i.e. P) and
    $Q \leftarrow min_{k \in B} Q_{i^*k},\ where B = \{1 \le k \le Ndim\}$;
    if $Q < +\infty$ then $k^*$ $\leftarrow$an index which supplies this minimum (i.e. Q)
    $R \leftarrow min\{P, Q\}$; $time\,[i^*, new[i^*]] \leftarrow R$ ;
    if $R < +\infty$ then
      if $P < Q$ then $partnr\,[i^*, new[i^*]] \leftarrow N + k^*$
      else { /" case $Q \ge P$ "/
      $time\,[jj, new[jj]] \leftarrow R$;
      $m \leftarrow partnr\,[jj, new[jj]]$ ;
        $partnr\,[jj, new[jj]] \leftarrow jj$; $partnr\,[jj, new[jj]] \leftarrow i^*$;
        if $m \ne \Lambda$ and $m \ne i^*$ then $partnr\,[m, new[m]] \leftarrow \Lambda$ ;
      } /" end $Q \ge P$ clause
  } /"end while loop"/
```

Periodic Boundary

Periodic boundary conditions are intended to mimic very large systems i.e., the investigated system is thought to be much larger than the simulated number of particles. The particles are contained within a primary simulated volume; when a particle leaves one side of this volume, it re-enters from the opposite side as shown in figure 2.6. Thus, periodic boundary conditions allow the simulation to proceed as if the primary volume was surrounded by identical copies of itself.

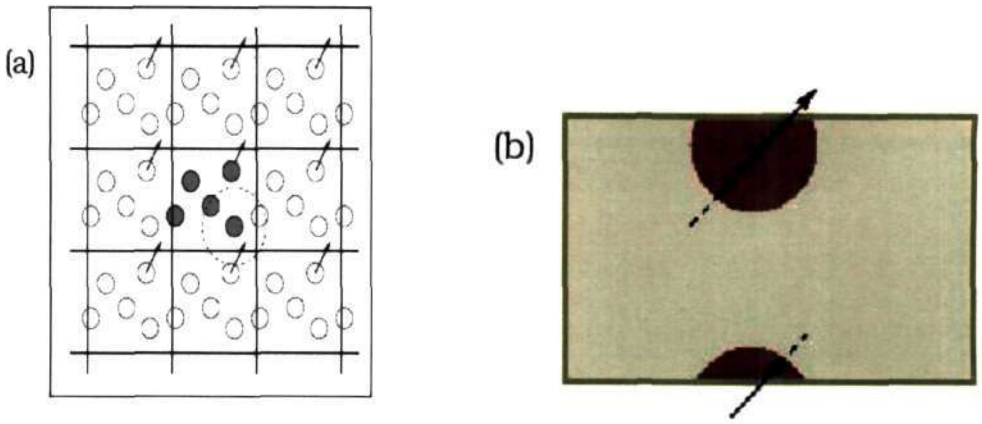

Figure 2.6: The basic simulation volume (particles are of black color) is repeated in all dimensions an infinite number of times. Here the neighbor volumes are drawn in grey.

Shear Boundary : Lees-Edward Boundary Condition

For the case of unbounded shear flow, some modifications are needed on the top and bottom boundaries. According to Lees-Edwards boundary condition (Lees & Edwards (1972)), a steady linear velocity profile is applied with a constant velocity gradient via shifting the replica images of top and bottom boundaries without deforming the box. The idea is to replace sliding walls by sliding replica system: layers of replicas that are adjacent in the y-direction move with a relative velocity $\dot{\gamma} L_y \mathbf{n_x}$ (see figure 2.7), which ensures periodicity at a shear rate $\dot{\gamma}$. Here L_x, L_y and $L_z$are dimensions of the simulation box along x, y and z directions, respectively and $\mathbf{n_x}$, $\mathbf{n_y}$ and $\mathbf{n_z}$ are the respective unit vectors. The coordinate system is fixed at the centre of the simulation box. A particle crossing a y-boundary requires special treatment because the x-components of its position and velocity are both discontinuous (not for the replica system just entered but relative to the opposite side of the region itself into which the particle is actually inserted). The velocity change, whenever

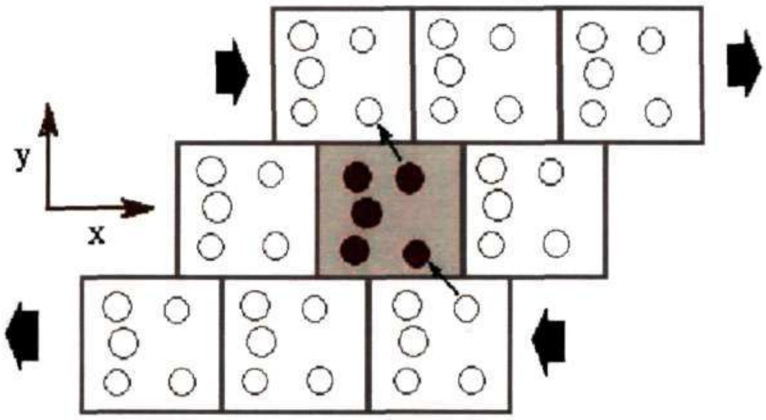

Figure 2.7: Homogeneous shear boundary conditions (box with colour balls is the simulation box)

a ± y-boundary is crossed, is $\mp\dot{\gamma}L_y\mathbf{n_x}$, and the coordinate change is $\mp d_x\mathbf{n_x}$, where the total relative displacement of the neighboring replicas, only meaningful over range $-L_x/2 \leq d_x \leq L_x/2$, is given by $d_x = (\dot{\gamma}L_y t + L_x)\text{mod}(L_x - L_x/2)$. Note that since the x-coordinate changes when a y-boundary is crossed, an additional correction for periodic wraparound in the x-direction may be needed. Interactions that occur between particles separated by the y-boundary require an offset value of $-d_x$.

When using the cell method (*Allen&Tildesley* (1987)) for the interaction calculation, the range of neighbor cells in the x-direction for adjacent cells on the opposite sides of the y-direction must extend over four cells, rather than the usual three, to allow for the fact that the cell x-edges of the sliding replicas are not usually aligned. If there are M_x cells on an edge, the additional cell offset across the ± y-boundary is $\Delta M_x = \text{Int}[M_x(1 \mp d_x/L_x)] - M_x$ (Rapaport (1995)).

Predict Event

Predicting future events after a collision or cell crossing is carried out by the subroutine "Predictevent".

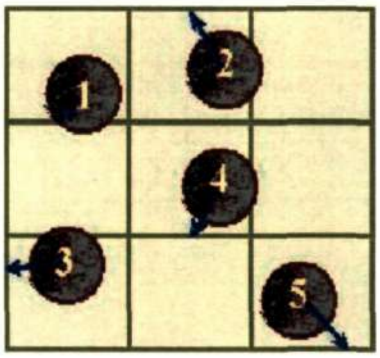

Figure 2.8: Particle are scheduled for cellcrossing event

Cellcrossing Event :
The first part of the routine looks at possible cell-boundary crossings in all directions and picks the earliest one. In figure 2.8 we are showing a snapshot at a particular time with five particles in x-y plane (z plane is not shown for clarity). The space is divided into nine cells. Next we calculate the time for cell-crossing and keep track of only minimum time required for this event for all particles. That time is defined in the above algorithm by Q_{ik} for the ith particle.

$$Q_{ik} \overset{\text{def}}{=} cellcrossingtime\left(state\left[i, old[i]\right], time\left[i, old[i]\right], k\right) \tag{2.22}$$

where $1 \leq i \leq N$ and $1 \leq k \leq Ndim$. Here $Ndim$ is taken as 3 for 3D simulation i.e. k can take value 1,2 and 3 according to cell-crossing in the x,y and z directions, respectively. After that $Q \overset{\text{def}}{=} min\left[Q_{ik}\right] = Q_{ik^*}$, and k^* is an index which provides this minimum (i.e. Q)

Collision Event :
The second part of the algorithm examines every particle in cells that must be scanned for all possible collisions and determines whether a collision is possible or not. The interesting dynamics of hard-sphere system is embodied in collision rules;

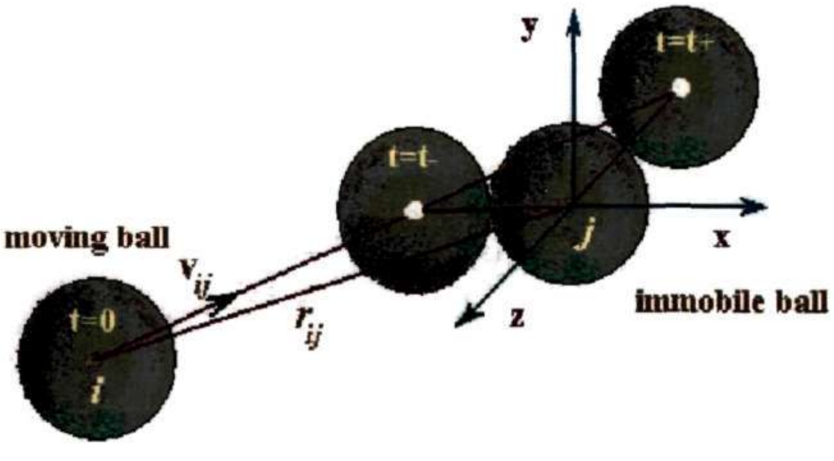

Figure 2.9: Geometrical meaning of two solutions of $|\mathbf{r_{ij}} + \mathbf{c_{ij}}\tau| = d$

between collisions nothing happens and the particles move in straight lines (if there is no body force). Consider two identical particles i and j separated by a distance $\mathbf{r_{ij}} = \mathbf{r_i} - \mathbf{r_j}$ and having a relative velocity $\mathbf{c_{ij}} = \mathbf{c_i} - \mathbf{c_j}$. These particles will collide when their separation becomes equal to their diameter d; if this happens it will occur at some time τ in the future, where τ is the smaller positive solution of

$$|\mathbf{r_{ij}} + \mathbf{c_{ij}}\tau| = d, \tag{2.23}$$

which is a quadratic equation in τ:

$$\tau^2 c_{ij}^2 + 2b_{ij}\tau + r_{ij}^2 - d^2 = 0. \tag{2.24}$$

If $b_{ij} = \mathbf{r_{ij}} \cdot \mathbf{c_{ij}} > \mathbf{0}$, then the particles are going away from each other and they will not collide. If $b_{ij} > 0$, it may still be true that $b_{ij}^2 - c_{ij}^2 \left(r_{ij}^2 - d^2\right) < 0$, for which eqn. 2.24 has complex roots and again no collision occurs. For other cases (assuming that the spheres are not overlapping), two positive roots arise, the smaller of which corresponds to impact

$$\tau = \frac{-b_{ij} - \left[b_{ij}^2 - c_{ij}^2 \left(r_{ij}^2 - d^2\right)\right]^{1/2}}{c_{ij}^2}. \tag{2.25}$$

We store this value $[\tau + timenow]$ to P_{ij} which is defined as:

$$P_{ij} \overset{\text{def}}{=} collisiontime\left(state\left[i, old[i]\right], time\left[i, old[i]\right], state\left[j, old[j]\right], time\left[j, old[j]\right]\right) \tag{2.26}$$

where $1 \leq i, j \leq N$. Now $P \overset{\text{def}}{=} min\left[P_{ij}\right] = P_{ijj}$ and jj is that particular interacting particle which supplies this minimum i.e. P.

After getting P and Q, we have to compare their values to predict the final future event for the ith particle.

Case 1:

$\mathbf{Q} < \mathbf{P}$; ith particle is scheduled for cellcrossing event. It is indicated by $partnr\left[i, new[i]\right]$ array.

$$partnr\left[i, new[i]\right] \leftarrow N + k^*$$

Case 2:

$\mathbf{Q} \geq \mathbf{P}$; ith particle is scheduled for collision event with jjth particle. It is indicated by

$$\begin{aligned} partner\left[i, new[i]\right] &\leftarrow jj, \\ partner\left[jj, new[jj]\right] &\leftarrow i, \end{aligned}$$

Delayed Update

Event-driven algorithms are the best choice for models where discrete instantaneous events occur asynchronously. In this algorithm, if at time t, an event involving particle i is processed, only the state of that particle is examined and explicitly modified (Rapaport (1980); Lubachevsky (1991)). The states of most other particles need not be known at t and are not examined by the algorithm. Therefore the application of **advance**, **cellcrossing** or **propcesscolision** should be delayed until the latest possible moment when the scheduled event is being processed. This saves computational time. If their is no external force (gravity, magnetic field etc.) in the system, the **advance** event of the ith particle can be written schematically as:

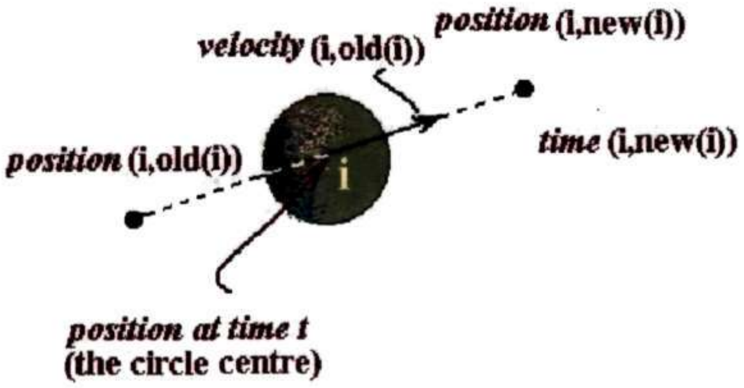

Figure 2.10: One particle is shown at time t i.e. timenow. Its state is required to be updated via *cellcrossing* or *pre-collisional* event

Advance Event:

$$\left.\begin{aligned} position\,(i,new(i)) &\leftarrow position\,(i,old(i)) + \\ &\quad (time\,(i,new(i)) - time\,(i,old(i)))\,velocity\,(i,old(i))\,, \\ velocity\,(i,new(i)) &\leftarrow velocity\,(i,old(i)) \end{aligned}\right\}$$

Here two arrays $new[1:N]$ and $old[1:N]$ with elements equal 1 or 2 are maintained. The value $new[i]$ is the pointer to the new event for component i and the value $old[i]$ is the pointer to the old event for component i. When $new[i]$ is updated, $old[i]$ is updated immediately after, so that relation $new[i] + old[i] = 3$ remains invariant.

2.2.2 Algorithm: Bounded shear flow

Figure 2.11 shows a schematic diagram of bounded granular Couette flow which is a simple geometry where both shear and physical boundary interactions exist. To simulate Couette flow we use the same algorithm for unbounded flow with some modifications. In our simulation of granular Couette flow, we place two physical walls at L_y distance apart in y-direction. The upper and lower walls are moving

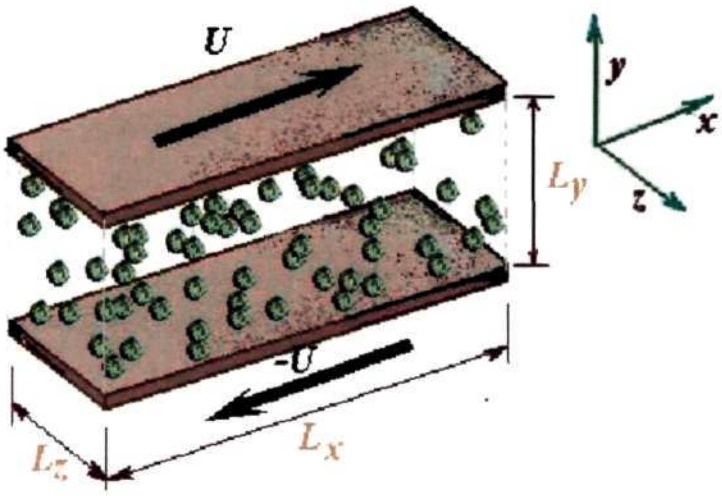

Figure 2.11: Schematic view of bounded shear flow.

with $+U\mathbf{n_x}$ and $-U\mathbf{n_x}$, respectively. In other directions, we are putting periodic boundary conditions. The algorithm is as follows:

Initialisation

```
$timenow = 0$ ;
$signal = 0$ ;
$endtime =$ timbig;
$Ndim = 3$ ;

$$\left.\begin{array}{ll} new(i) & \leftarrow 1 \\ old(i) & \leftarrow 2 \\ time[i,1] & \leftarrow 0 \\ partnr[i,1] & \leftarrow \Lambda \\ state[i,1] & \leftarrow \text{initial state of } i \text{ th component} \end{array}\right\}_{i=1\forall N}$$

1. while timenow $<$ endtime do {
2.   timenow $\leftarrow min\,[time\,[i, new[i]]]_{1\leq i\leq N}$
       $i^* \leftarrow$ index for minimum time (i.e. timenow)
3.   $jj \leftarrow$ partnr$[i^*, new[i^*]]$
```

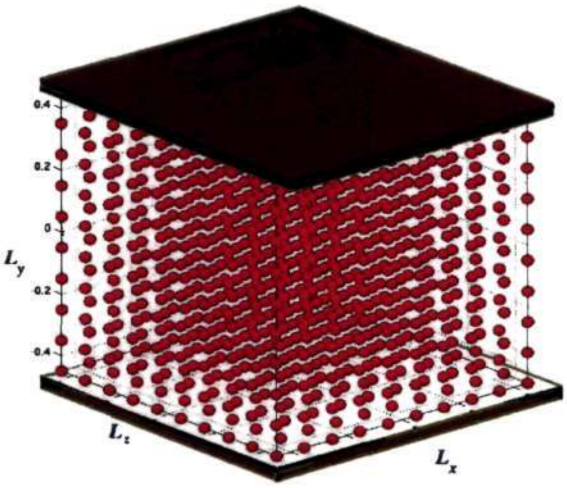

Figure 2.12: Schematic of the initial arrangement of particles in a 3D box with physical walls

```
if { $jj > 0$ then /"state update required"/ ;
  state1 $\leftarrow$ advance($state\,[i^*, old[i^*]]\,, time\,[i^*, old[i^*]]\,, time\,[i^*, new[i^*]]$) ;
  $state\,[i^*, new[i^*]] \leftarrow cellcrossing\,[state1]$;
  if cellcrossing in boundary special treatment for $state\,[i^*, new[i^*]]$ ;
  if {$1 \leq jj \leq N + Ndim + 1$ /" wall-particle interaction interaction"/
    $state\,[i^*, new[i^*]] \leftarrow wallcollision\,[state1]$
  } /" end wall particle interaction"/ ;
    if {$1 \leq jj \leq N$ /" two-component interaction"/
      stat2 $\leftarrow$ advance($state\,[jj, old[jj]]\,, time\,[jj, old[jj]]\,, time\,[jj, new[jj]]$)
    $(state\,[i^*, new[i^*]]\,, state\,[jj, new[jj]]) \leftarrow processcollision\,[state1, state2]$
    $partnr\,[jj, new[jj]] \leftarrow -i^*$ /" no update for $jj$ "/ ;
    $new[jj] \leftarrow old[jj]; old[jj] \leftarrow 3 - new[jj]$ ;
  } /" end two-component interaction"/ ;
$new[jj] \leftarrow old[i^*]; old[i^*] \leftarrow 3 - new[i^*]$ ;
} /"end state update required clause"/ ;
call for predictevent /" to get the value P and Q /"
  $P \leftarrow min_{j \in A(i^*)} P_{i^*j},\ where A(i^*) = \{1 \leq i \leq N, j \neq i^*,$
  $time\,[j, new[j]] \geq P_{i^*j}\}$;
```

```
      if $P < +\infty$ then$jj$ ←an index which supplies this minimum (i.e. P) and
    $Q \leftarrow min_{k \in B} Q_{i^*k},\ where B = \{1 \le k \le Ndim\}$;
      if $Q < +\infty$ then $k^*$ ←an index which supplies this minimum (i.e. Q)
    $R \leftarrow min\{P, Q\}$; $time\,[i^*, new[i^*]] \leftarrow R$ ;
    if $R < +\infty$ then
      if $P < Q$ then $partnr\,[i^*, new[i^*]] \leftarrow N + k^*$
        if event is wall collision then $partnr\,[i^*, new[i^*]] \leftarrow N + Ndim + 1$
      else { /" case $Q \ge P$ "/
      $time\,[jj, new[jj]] \leftarrow R$;
      $m \leftarrow partnr\,[jj, new[jj]]$ ;
      $partnr\,[jj, new[jj]] \leftarrow jj$; $partnr\,[jj, new[jj]] \leftarrow i^*$;
      if $m \ne \Lambda$ and $m \ne i^*$ then $partnr\,[m, new[m]] \leftarrow \Lambda$ ;
      } /" end $Q \ge P$ clause
  } /"end while loop"/
```

From the above algorithm, it is clear that except the *predictevent* the rest of the algorithm is same as in the unbounded case. In the *predictevent* subroutine, besides calculating cell-crossing time for a particle we have to take into account the time taken by the particle to collide with physical walls in both directions of y-axis. The minimum time is stored in Q. If the time taken for wall-collisions is minimum, then $signal \leftarrow 1$ and we update its *partnr* array as:

$$partnr\,[i, new[i]] \leftarrow N + Ndim + signal$$

On the other hand, if the time taken for the cellcrossing event is minimum, then $signal \leftarrow 0$ and we update *partnr* array as in the unbounded case (section 2.2.1).

2.3 Method of Averaging and Macroscopic Quantities

In simulations of granular flow, the energy is supplied in the form of shear force applied to the domain. This energy is then transferred from mean flow to random motion of particles via shear work. The energy is always dissipated due to

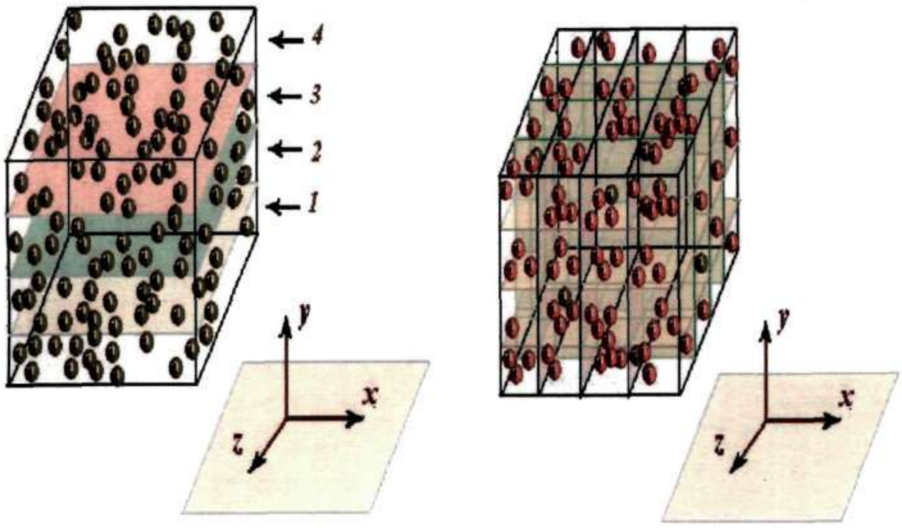

Figure 2.13: (a) Schematic diagram for bin-wise averaging and (b) cellwise averaging method

particle-particle and wall-particle (bounded flow) interactions. Therefore, a non-equilibrium steady-state (Campbell (1990), Lun & Bent (1994), Tan & Goldhirsch (1997), Alam & Luding (2003), 2003a, 2005, 2005) is achieved after the dissipation and production balance. Monitoring system's kinetic energy with time is one way to get an idea about the steady-state. The statistical measurements of various quantities are performed only when system has reached steady-state condition. After the steady-state condition, the microscopic properties of the flow, local mean velocity (u), granular translational temperture (T), rotational temperature (θ) and system density (ϕ), remain invariant in time.

All the statistical quantities are calculated based on two procedures. One is binwise averaging method where the whole simulation box is divided into a number of bins across the channel height. The schematic diagram for "binwise" averaging method is shown in figure 2.13(a). Translational (T) and rotational (θ) energies have been calculated based on binwise averaging method and their temporal evolution are shown in the main panel of figure 2.14(a); inset shows their ratio. Figure 2.14(b) shows the same as in figure 2.14(a), but all results are based on "cell-wise"

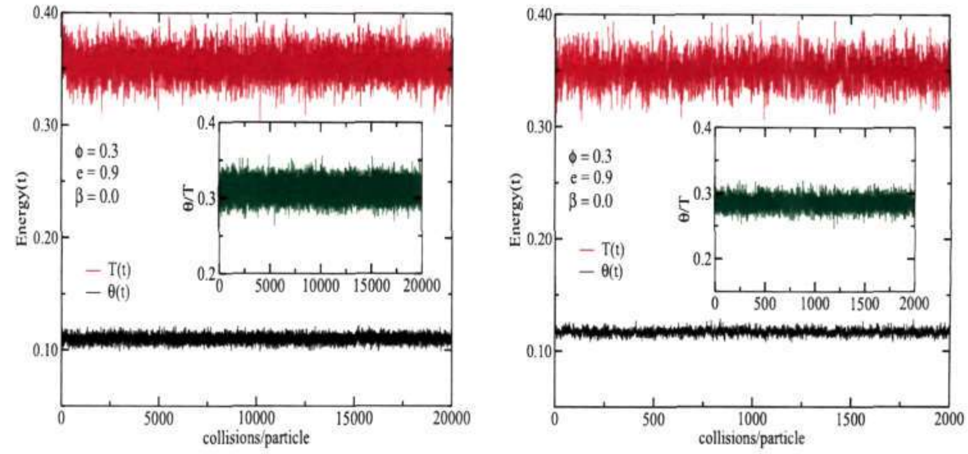

Figure 2.14: (a) Temporal evolution of translational and rotational energy, calculated based on binwise averaging method (main panel); inset shows temporal evolution of their ratio. and (b) Same as (a), but energy is calculated based on cellwise averaging method with 3x3x3 cells. Total number of particles is N = 1000.

averaging method. There is no pronounced difference observed for results based on two methods. But with the increase of system size, along with collisional dissipation, the density inhomogeneity is not only observed across the channel height but also over the whole system. Then we need another method where the whole system is divided into a number of cells shown in figure 2.13(b) and the local mean quantity is calculated based on "cell-wise averaging" method. Extensive comparison between two methods will be discussed in chapter 4. After imposing the cellwise averaging method, the macroscopic quantities can be calculated as follows:

$$\phi_k = \frac{\pi}{6}\frac{N_k d^3}{V_k} \tag{2.27a}$$

$$\mathbf{u^k} = \langle \mathbf{c^k} \rangle = \frac{1}{N_k}\sum_j \mathbf{c_j} \tag{2.27b}$$

$$\omega^{\mathbf{k}} = \langle \omega^{\mathbf{k}} \rangle = \frac{1}{N_k}\sum_j \omega_{\mathbf{j}} \tag{2.27c}$$

$$T = \frac{1}{3}\langle \mathbf{C} \cdot \mathbf{C} \rangle \tag{2.27d}$$

$$\theta = \frac{I}{3m}\langle \mathbf{\Omega} \cdot \mathbf{\Omega} \rangle \tag{2.27e}$$

where d is the diameter and m is the mass of a particle, taken as unity, N_k is the number of particles and V_k is the volume of the kth cell. Here $\mathbf{c}$ and $\mathbf{C} = \mathbf{c} - < \mathbf{c} >$ are the instantaneous and fluctuating translational velocities, respectively; ω and $\mathbf{\Omega} = \omega - \langle \omega \rangle$ are instantaneous and fluctuating (peculiar) roatational velocities, respectively; $\langle \mathbf{c^k} \rangle$ and $\langle \mathbf{\Omega^k} \rangle$ denote the mean translational and roational velocity of kth cell, respectively. T and θ are the translational and rotational granular temperatures, respectively; I is the moment of inertia of a particle.

2.4 Code Validation

2.4.1 Unbounded Shear flow

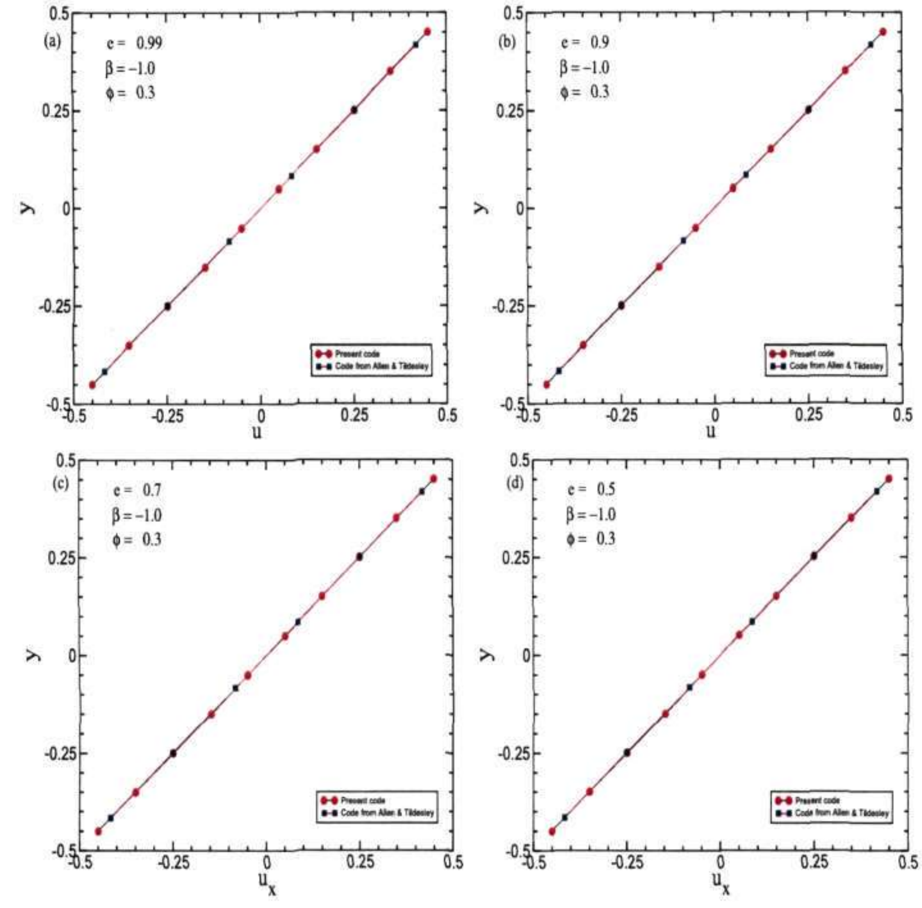

Figure 2.15: Effect of e on streamwise velocity profile for unbounded shear flow.

For the validation of our code, we compare the results based on Allen & Tildesley code and our code. This is very well-known code that can deal with small system size without having any efficient features that present code has, like delayed update, cell-crossing event etc. Results are based on simulations of $N = 1000$ and unit shear rate; in all cases we maintain a volume fraction $\phi = 0.3$ and unit cubic section for simulation. Figure 2.15 shows streamwise velocity profile for (a) $e = 0.99$, (b) $e = 0.9$, (c) $e = 0.7$ and (b) $e = 0.5$. This profile is independent of any restitution parameter.

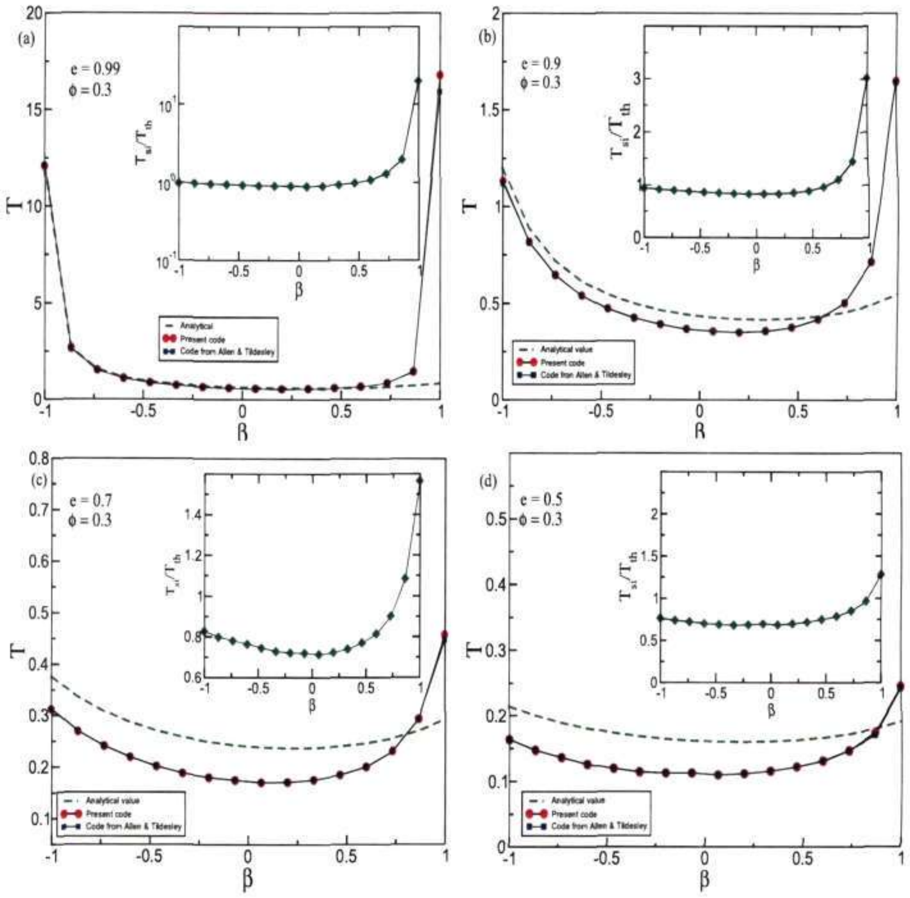

Figure 2.16: Effect of β on translational temperature for unbounded shear flow.

Figure 2.16 shows the effect of tangential restitution coefficient on translational temperature. Simulation results agree with analytical results (5.11 in Chapter 5) in the elastic limit ($e \simeq 0.99$) except for rough particles. For rough particles ($\beta \simeq 1.0$), the simulation results deviate from analytical results with increasing value of e. This deviation is shown in insets of figure 2.16 which shows the ratio of simulation and analytical temperatures.

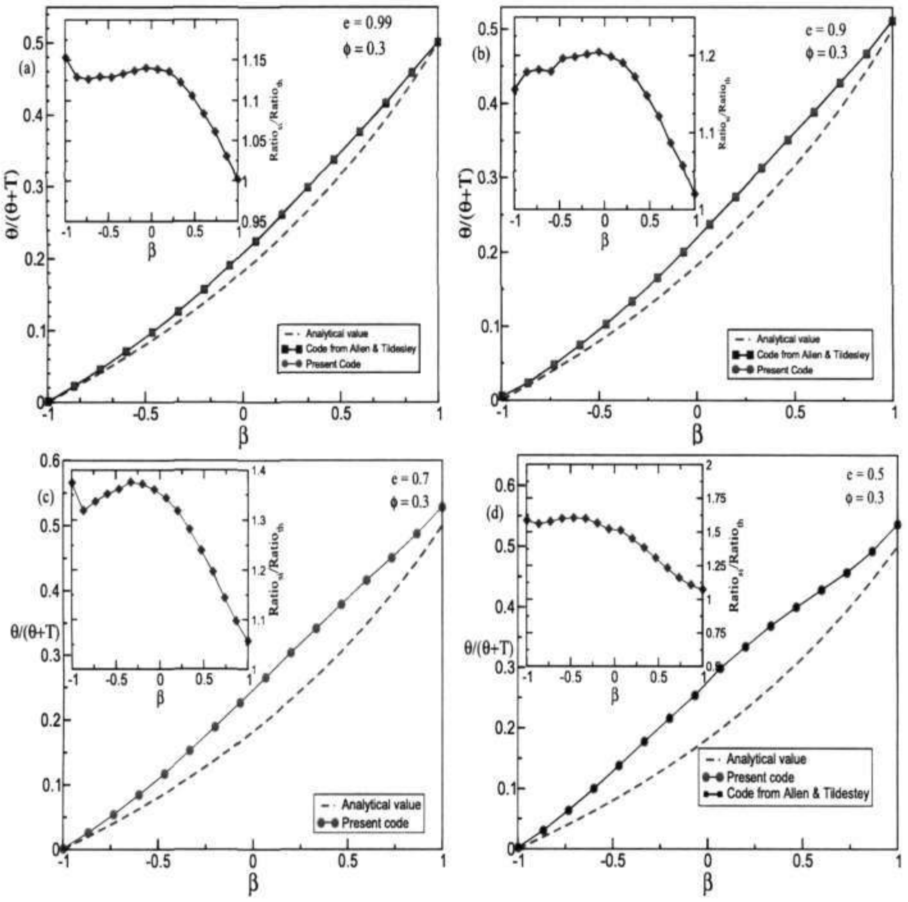

Figure 2.17: Effect of β on temperature ratio for unbounded shear flow.

The ratio of rotational and translational temperatures, $\theta/(\theta+T)$, is shown in figure 2.17; each inset shows the deviation from theoretical values. Here we are getting large deviation at intermediate values of β. For perfectly rough particles ($\beta = 1.0$) with $e = 1$, translational and rotational granular temperatures are equally partitioned. At the other extreme, i.e. for perfectly smooth particle ($\beta = -1.0$), $\theta = 0$, i.e. all the energies are contained in translational degrees of freedom. This result agrees with simulation results in figure 2.18 taken from previous work (McNamara & Luding (1998)).

In figure 2.19 we show results for spanwise rotational velocity ω_z. At $\beta = -1.0$, the bridge for the transfer of energy from the translational to rotational degrees of freedom through collision dynamics breaks down. For $\beta \sim -1$, the transfer

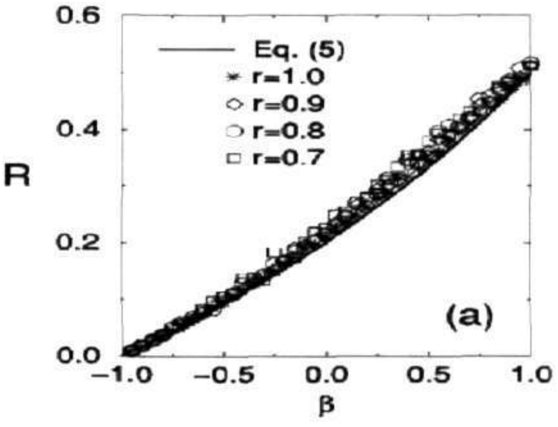

Figure 2.18: Figure from McNamara & Luding (1998) showing temperature ratio with tangential restitution coefficient.

of energy from the translational to rotational degrees occur at a very slow rate. Therefore, we have to go for higher number collisions to get a value of ω_z close to the analytical one. Figure 2.19 also shows that the magnitude of ω_z varies with the value of e.

2.4.2 Bounded Shear flow

For bounded shear flow too, we have compared results from the code based on the algorithm given in Allen & Tildesley (1987) with those from our present code. All results are shown for $N = 1000$, with $\phi = 0.3, e_w = 0.9, \beta = 1.0 = \beta_w$ for different values of e.

Figure 2.20 shows the streamwise velocity profile across the channel height for different values of normal restitution coefficient. We are getting considerable slip at the wall. We see that the profile deviates from a straight line as we increase inelasticity. For $e = 0.5$ and $e = 0.7$, the velocity gradient is higher near the wall compared to the centre of the channel.

In figure 2.21 the volume fraction is plotted across the channel height, with parameter values as in figure 2.20. Here we clearly see variations of density across the channel height; lower density exists near the wall and higher density is prevailing

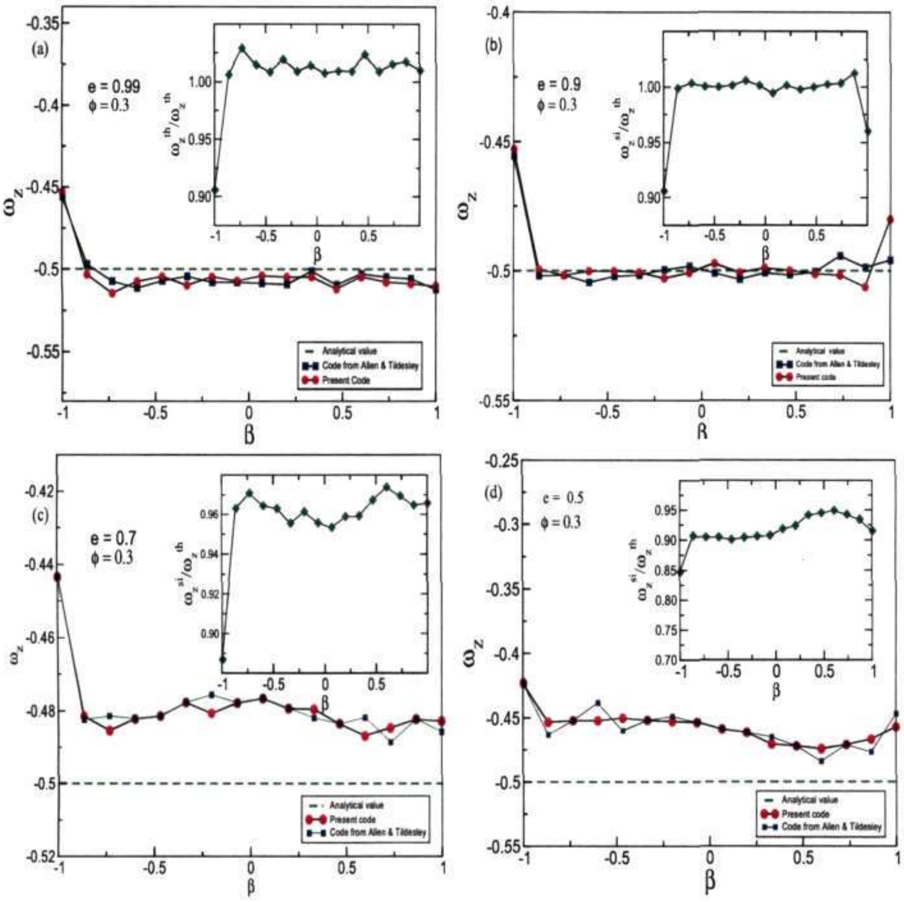

Figure 2.19: The effect of β on the spanwise rotational velocity for unbounded sheared flow taken from present code and Allen & Tildesley.

around the channel-centre. If we decrease restitution coefficient we get an increase in density variation. In the elastic limit, i.e $e \simeq 1.0$, the density is almost constant apart from the vicinity of two walls.

Granular translational temperature profile is shown in figure 2.22. Both codes agree with each other for different values of e. In the elastic limit the temperature is almost constant across the channel. With the decrease of e, the temperature variation becomes prominant across the channel height. The reason behind large temperatures near the wall is due to the low density and large velocity gradients there. Due to this large velocity gradient, the impact velocity of particles is large which results in a higher random velocity of the particles. This enhances granular temperature at walls. When this temperature comes through particle-particle

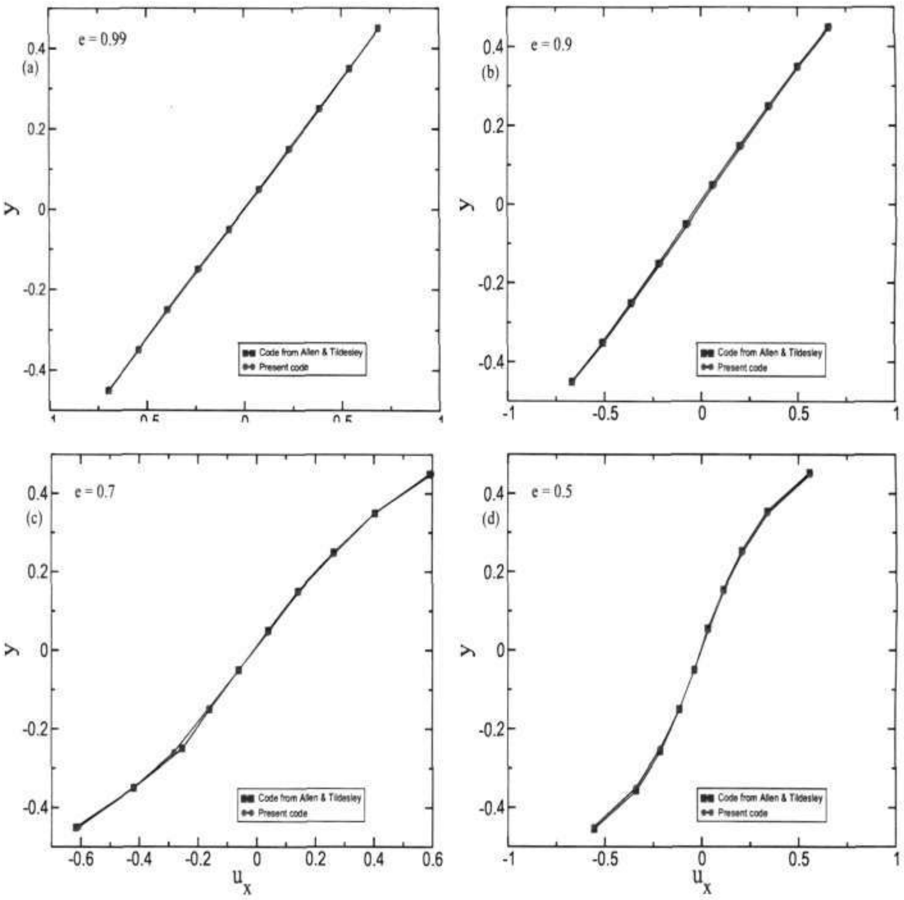

Figure 2.20: Velocity profile across the channel height for $\phi = 0.3$, $\beta = 1 = \beta_w$ and $e_w = 0.9$

collisions, it is also dissipated via collisional inelasticity. Therefore, for inelastic particles, at lower concentration part the dissipation is also low which results in a higher temperature. In the elastic limit, due to the uniformness of velocity gradient and density, temperature remains constant across the channel.

Figure 2.23 shows the particle spanwise rotational velocity across the channel height. It shows higher magnitude of rotational velocity near the walls due to large torques given by the walls. Near the centre of the channel the rotation velocity is almost uniform. The reason behind the jaw-like structure in figure 2.23 becomes clear if we consider particle dynamics near the wall (see figure 2.24).

A drastic change in the rotational velocity occurs near the boundary region of thickness of the order of a particle diameter. This is due to different ways of

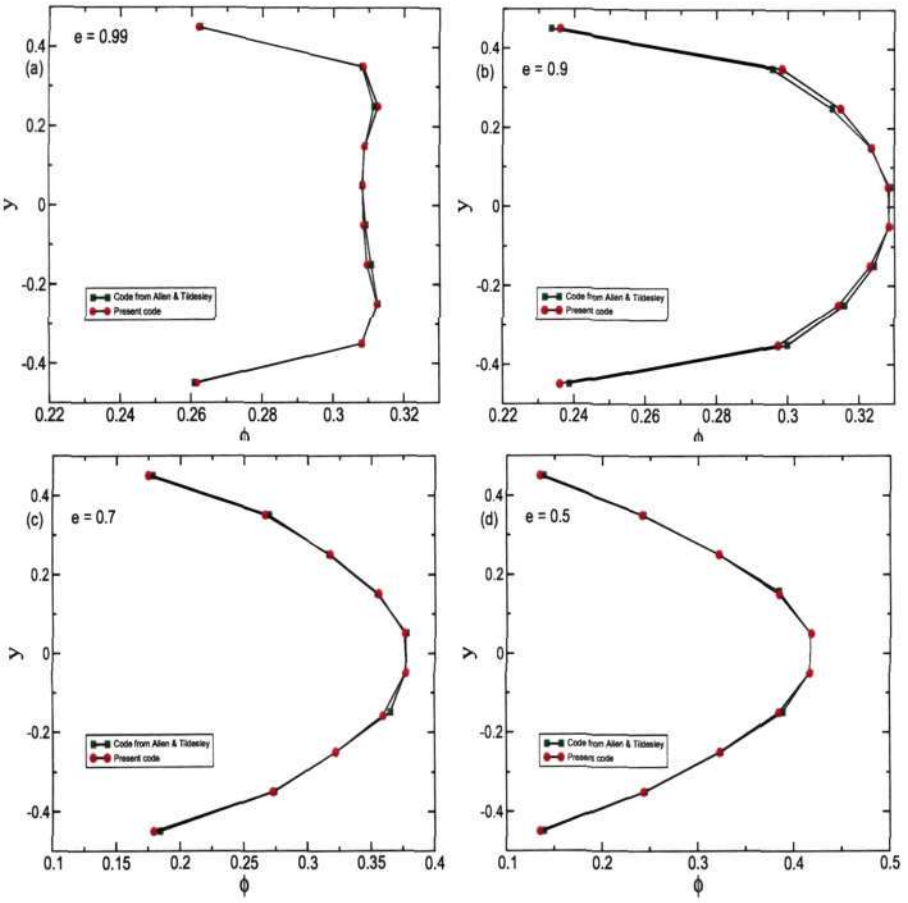

Figure 2.21: Density variation across the channel height, with parameters values as in figure 2.20.

generation of angular momentum. In the shear flow of granular particles (Alam & Luding (2003), Alam & Luding (2005)), most of the collisions occur on the upstream faces of a particle (see figure 2.25). Due to these two types of collisions, a colliding particle gets a clockwise rotation i.e. half of the shear rate induced in the system. In the centre part of the channel, the boundary effect is less and the magnitude of rotational velocity is close to half of the shear rate. On a collision with the wall, a particle gets a large value of rotation which is proportional to the slip velocity. Therefore just near the wall a large clockwise rotation is added to the particle. But a particle just below the first layer from wall experiences a counter clockwise field set by the first layer (see the bottom part of figure 2.24). Due to these two effects near the wall, the magnitude of the rotational velocity is

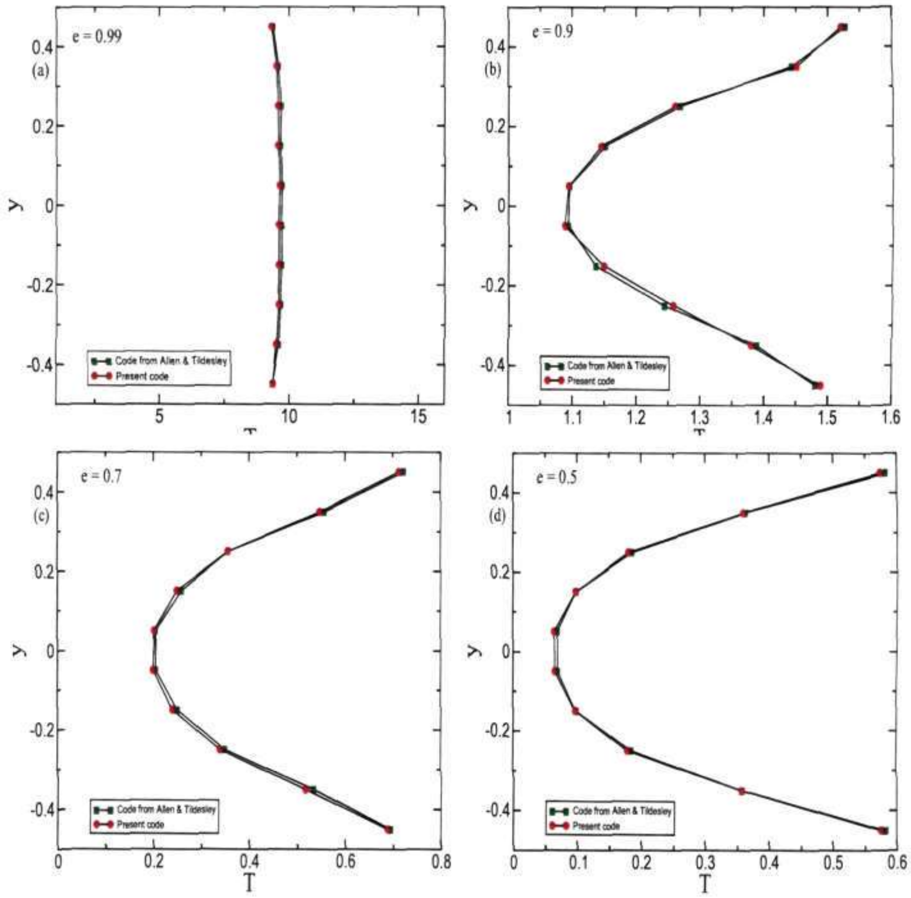

Figure 2.22: Temperature profile across the channel, with parameters values as in figure 2.20.

less compared to other regions. This gives rise to two peaks near the walls in figure 2.23.

The profiles of rotational temperature, θ, and temperature ratio, θ/T, are shown in figures 2.26 and 2.27, respectively. If we decrease e, a distinct difference between regions near the wall and the centre of the channel becomes visible. Due to large shear rates and low particle concentration near the wall, the transitional temperature lower in that region.

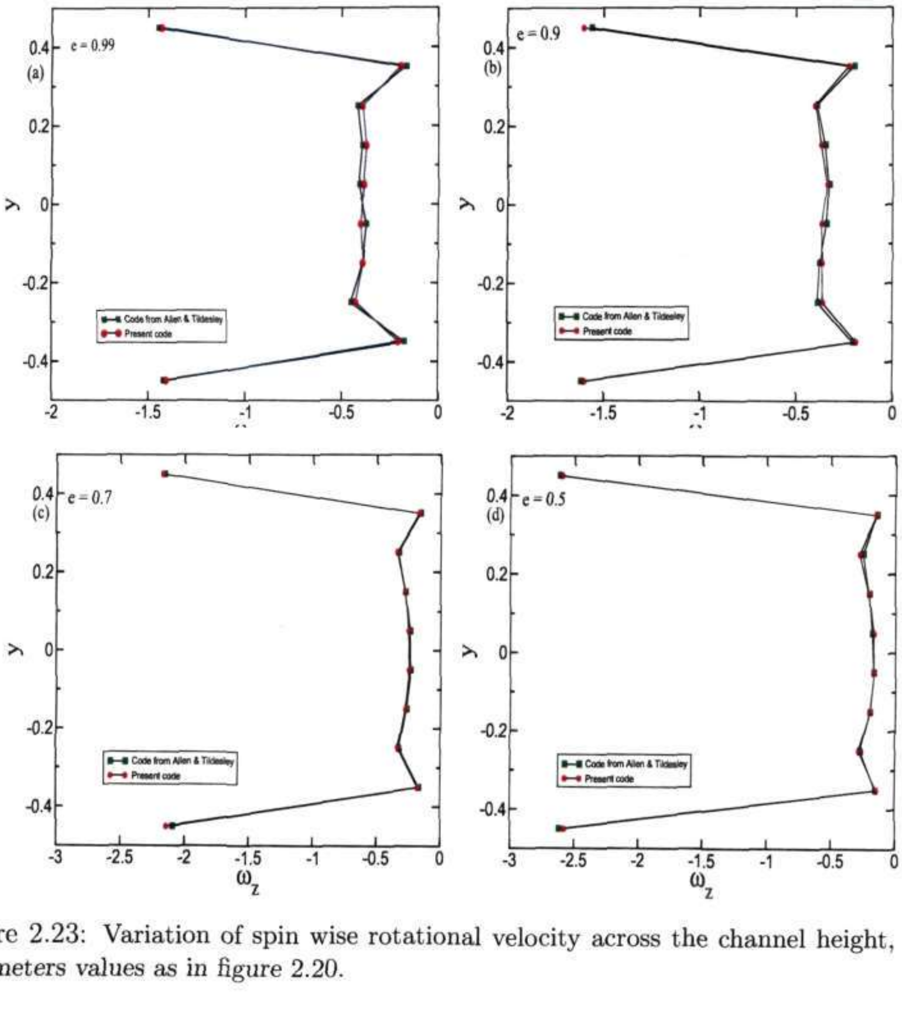

Figure 2.23: Variation of spin wise rotational velocity across the channel height, with parameters values as in figure 2.20.

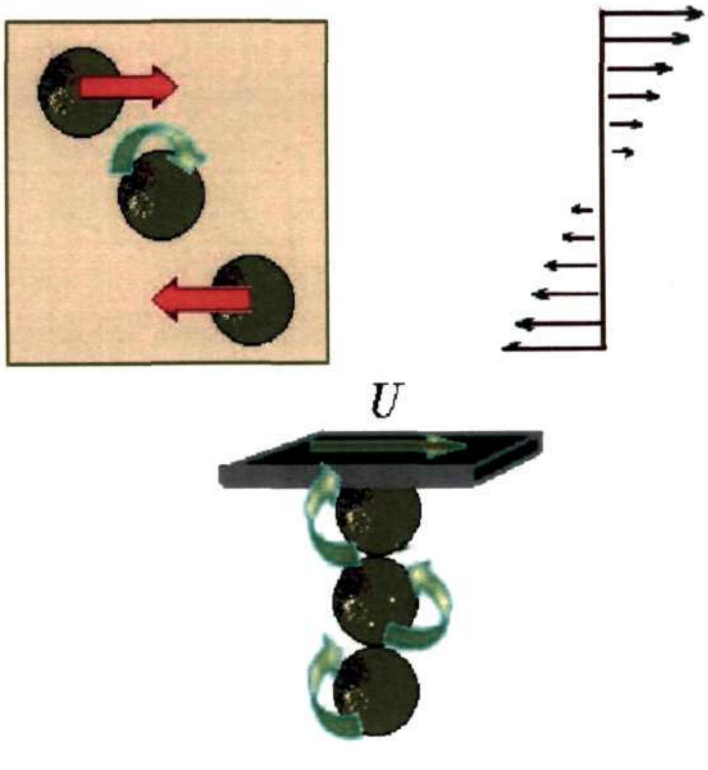

Figure 2.24: Top portion of figure shows rotation governed by shear field and bottom shows rotation due wall motion.

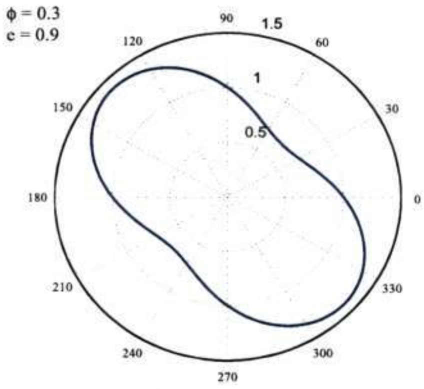

Figure 2.25: Plot for collision angle distribution for $\phi = 0.3$ and $e = 0.9$ in 2D (Alam & Luding (2003)). The collision angle is defined as the angle between the contact vector and the x-axis (measured anticlockwise from positive x-axis. Note that the collisions are more likely in the second ($\pi/2 < \theta_c < \pi$) and fourth ($3\pi/2 < \theta_c < 2\pi$) quadrants which is due to the antisymmetric velocity profile in shear flow.

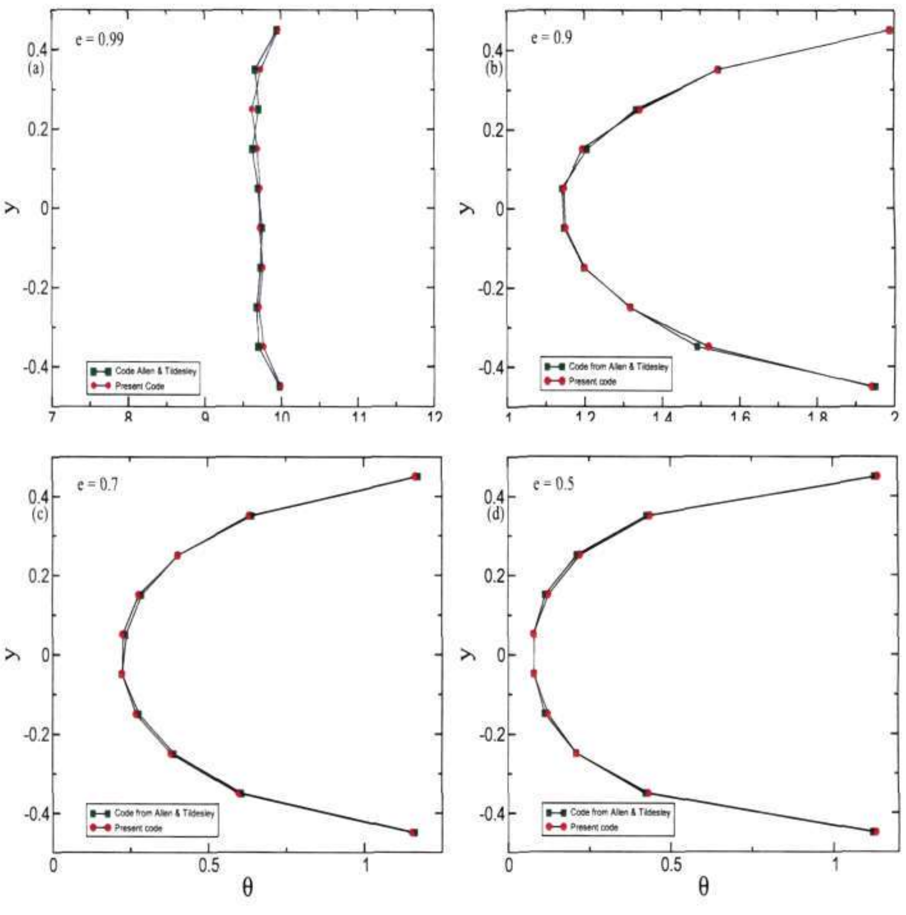

Figure 2.26: Variation of rotational temperature across channel height, with parameters values as in figure 2.20.

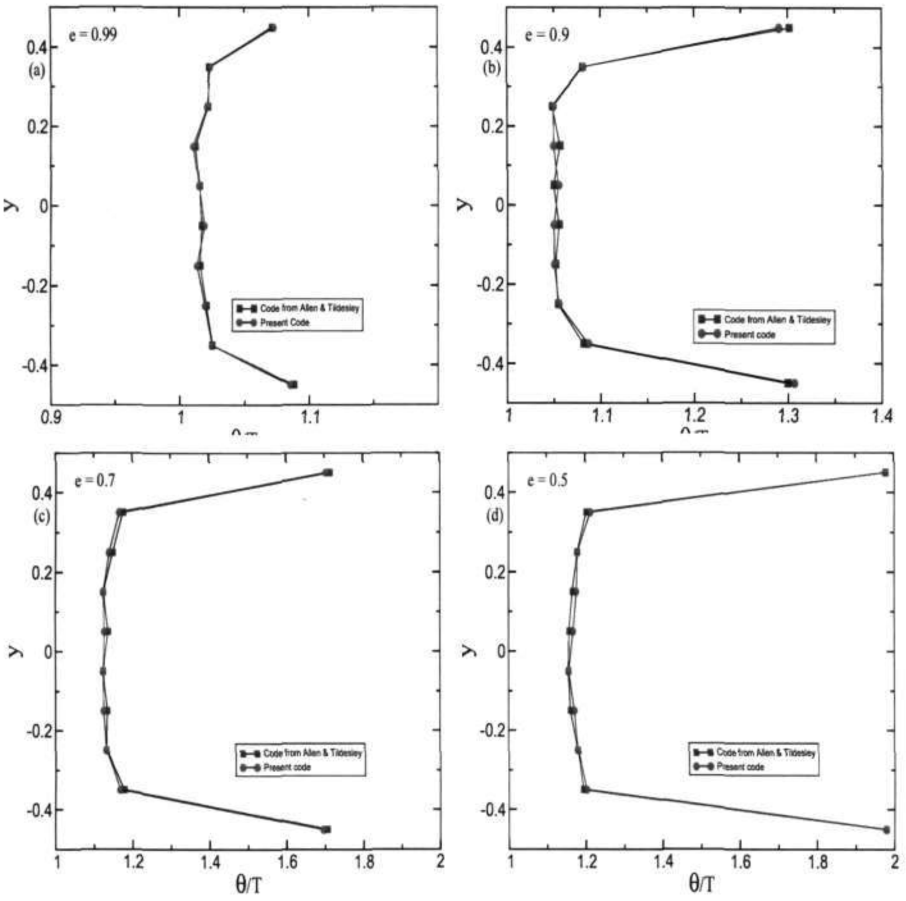

Figure 2.27: Temperature ratio across the channel height, with parameters values as in figure 2.20.

Chapter 3

BOLTZMANN LIMIT: VELOCITY FLUCTUATION AND CORRELATION

Granular flow at a very low density, well known as granular gas, is studied in this chapter. In the low density limit, the granular fluid behaves like a gas. Here all results are presented for a particle volume fraction $\phi = 0.01$, with the number of particles being N = 8000. For a few representative cases, the results were checked by using N = 4000 and 16000.

Before discussing correlations and distribution functions of fluctuating velocities, we present results on various mean-field quantities to check whether the flow is homogeneous or not. To check whether the particles are homogeneously distributed or not, we probe the distribution of mean density (volume fraction of particles) by dividing the computational box into 10x10x10 cells such that there are about eight particles in each cell. In the main panel of figure 3.1, the probability distribution of density and the effect of dissipation on it are shown. It is observed that there is no dissipation-induced density inhomogeneity in the system; for all dissipation levels the local density varies from 0.003 to 0.017 in about 90% cells. Two left insets show the projected snapshots of all particles (at steady state after 60000 collisions per particle) in the xy and yz-planes which suggest that no clustering is visible even at $e = 0.5$ and $\beta = 0$, and the particles are homogeneously distributed over the domain. In the top and bottom right insets, the probability distributions of translational and rotational temperatures are shown, respectively; these distributions also remain relatively unchanged (except tail regions) with increasing dissipation.

In figure 3.2, we show the effect of particle roughness on Knudsen number. We define Knudsen number as $Kn = l/L$, where the mean free path, l, is computed by averaging the distance ($l = \sqrt{\delta x^2 + \delta y^2 + \delta z^2}$) covered by particles during successive collisions over a large number of collisions and L is the length of the simulation box. In figure 3.2 the maximum Kn occurs at $\beta \sim 0$ and at other two limits, $|\beta| = 1$,

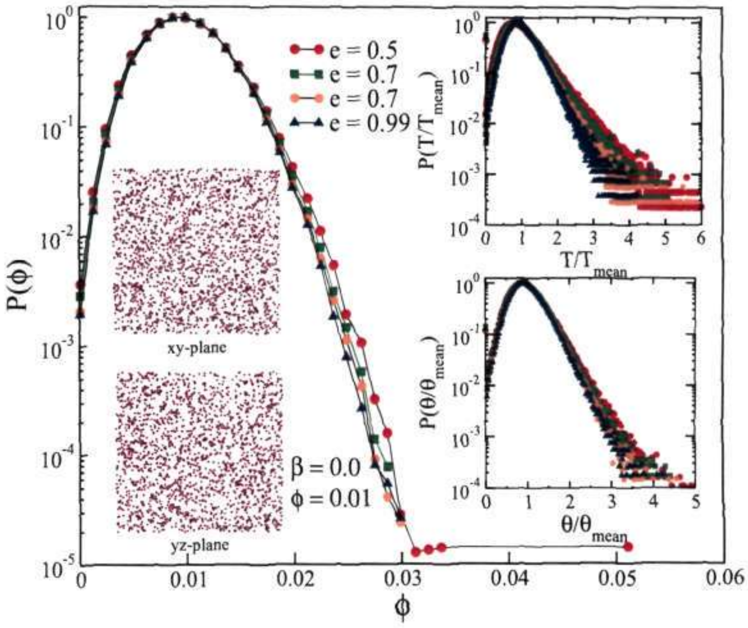

Figure 3.1: Probability distributions of mean density(mean panel), rotational (right upper inset) and translational temperature (right lower inset) for $\phi = 0.01$, $N = 8000$ and $\beta = 0$ for different values of e. Two left insets show projected particle snapshots in the xy- and yz-planes at steady state for $\beta = 0$ and $e = 0.5$.

it attains minimum values. The increases of Kn with dissipation can be explained from the similarity between the behavior of granular particles with gas molecules. At higher energy state ($e \sim 1$) the agitation of particles is more due to the increment in their random motion and hence the collision frequency increases. This leads to smaller mean-free time which is responsible for smaller mean-free path, ($Kn = l/L$) at $e = 1$. The probability distribution of free path (l) has been plotted for $\beta = -0.999$ and $\beta = 0$ in bottom left and right insets in figure 3.2. In the smooth limit, the tail of $P(l)$ is exponential for $e = 1$ as in a molecular gas (Reif (1985)). With increasing dissipation, the tail follows a power law distribution.

3.1 Velocity Distribution Function (VDF)

The fluctuating velocities, $C_i = c_i - \langle c_i \rangle$, are calculated based on *cell-wise* averaging as discussed in chapter 2. The VDF for translational velocity is plotted in the main panel of figure 3.3. In this plot, three data sets for $e = 0.5$, 0.7 and 1 have been

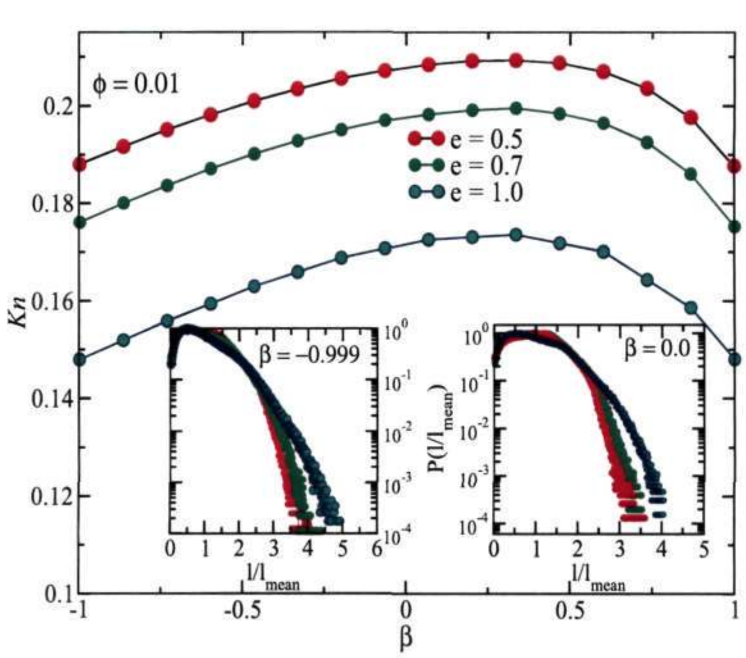

Figure 3.2: Effect of particle roughness on Knudsen number Kn (mean panel)for $\phi =$ 0.01 for different values of e. Two middle insets show Probability distributions of mean free path for $\beta = -0.999$ and $\beta = 0$, respectively.

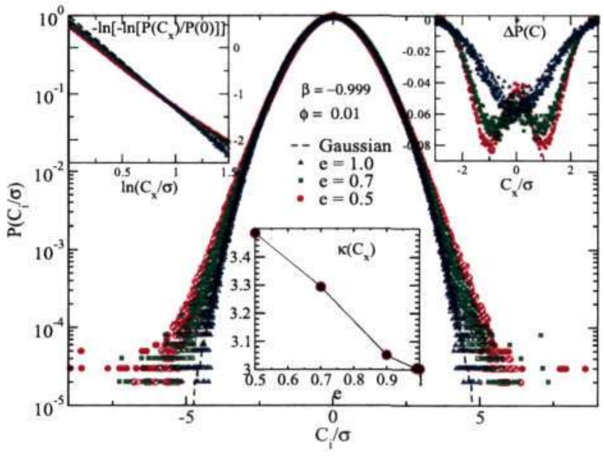

Figure 3.3: Translational velocity distribution (main panel) for $\beta = -0.999$ and $\phi = 0.01$. Top left inset shows $-ln[-ln[P(C_x/\sigma)/P(0)]]$ with $ln(C_x/\sigma)$ and top right inset depicts deviation at low-velocity region. The bottom inset shows the effect of e on the kurtosis of the distribution.

superimposed, and the black dashed line represents a Gaussian distribution. Note that the horizontal axis of the velocity distribution is scaled by σ, the standard deviation of the given quantity, and the vertical axis has been scaled such that $P(0) = 1$. For the elastic case ($e = 1$), $P(C_i)$ closely follows a Gaussian distribution and the deviation starts increasing as we increase inelasticity. The tails of the distribution follow an stretched exponential:

$$P(x) \sim exp(-\gamma x^{\alpha}), \quad \text{with} \quad x = C, \Omega \tag{3.1}$$

where γ and α are the prefactor and exponent for the distribution, respectively; for a Gaussian distribution, $\gamma = 1/2$ and $\alpha = 2$. The upper left inset in figure 3.3 shows the variation of $-ln[-ln[P(C_x/\sigma)/P(0)]]$ with $ln(C_x/\sigma)$; the slope of this straight-line provides the value of the exponent α. For the low-velocity region, the deviation from Gaussian can be calculated by $\Delta P(x) = P(x) - exp(-x^2/2)$, with $x = C/\sigma, \Omega/\sigma$. In the top right inset of figure 3.3, the deviation $\Delta(P(C/\sigma))$ is plotted in linear scale which becomes more pronounced with increasing collisional dissipation.

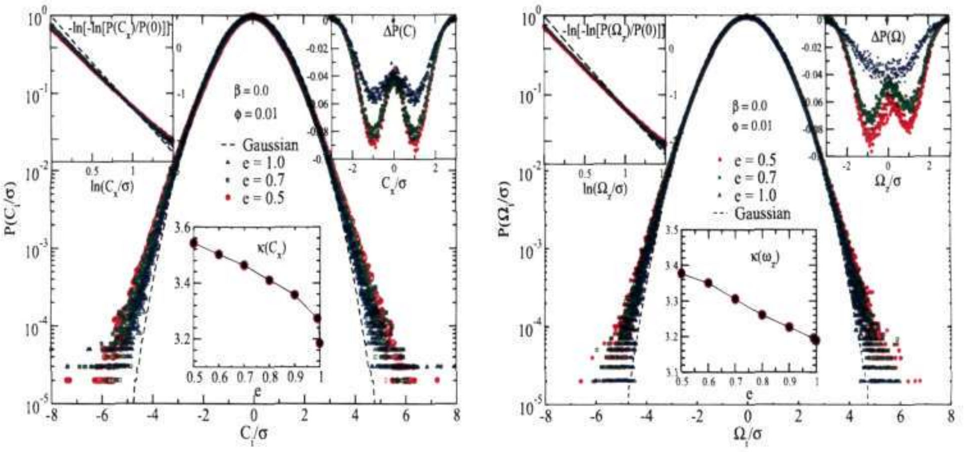

(a) (b)

Figure 3.4: (a) VDF for C_i (main panel) for $\beta = 0$ and $\phi = 0.01$. Top left inset shows $-ln[-ln[P(x/\sigma)/P(0)]]$ with $ln(x/\sigma)$ and top right inset depicts deviation at low-velocity region. The bottom inset shows the effect of e on the kurtosis of the distribution. (b) same as (a), but for Ω_i

In order to quantify the deviation from Gaussian distribution, we have calculated the kurtosis of distribution:

$$\kappa = \frac{\mu_4}{\mu_2^2}, \tag{3.2}$$

where

$$\mu_4 = \int_{-\infty}^{\infty} (x - \bar{x})^4 f(x)dx, \ \ \mu_2 = \int_{-\infty}^{\infty} (x - \bar{x})^2 f(x)dx$$

are the fourth and second moments about the mean of the distribution, respectively. The kurtosis for Gaussian distribution is 3. The dependence of kurtosis on dissipation is studied in the bottom inset of figure 3.3 and it varies almost linearly with e. For elastic collisions ($e = 1$), $\kappa(C_i) \sim 3.0$ which indicates that the distribution is nearly Gaussian. In the smooth limit ($\beta \sim -1$), the VDFs for all rotational velocities Ω_i are nearly Gaussian (not shown here). Note that we do not find any discernible difference among the VDFs of all three components of each velocity (C_i and Ω_i with $i = x, y, z$) and each velocity component follows the same distribution for a given e.

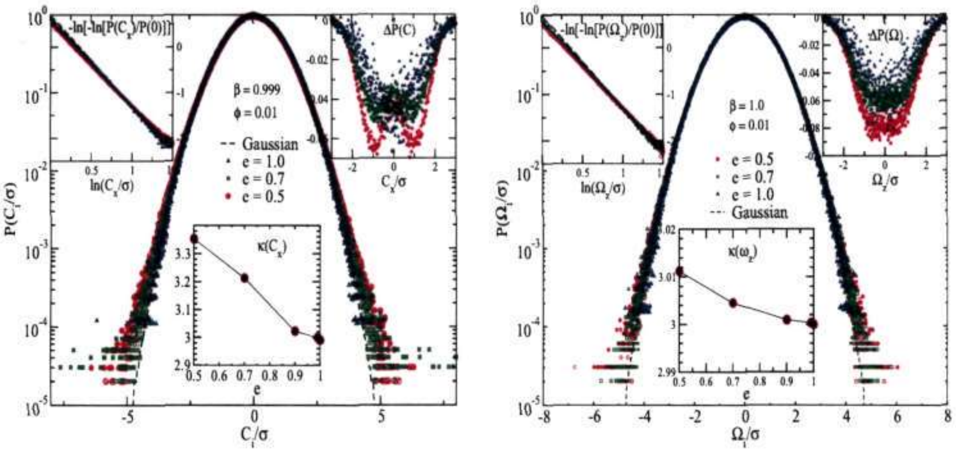

(a) (b)

Figure 3.5: Same as figure 3.4, but $for \beta = 1$

Next we study VDFs for C_i and Ω_i for $\beta = 0$ in figures 3.4(a) and 3.4(b), respectively. Beside $P(C_i)$, in the VDFs of Ω_i the deviation is observed due to rotational dissipation at $\beta = 0$. Even for $e = 1$, the deviation at tail regions of both $P(C_i)$ and $P(\omega_i)$ is visible and found to follow stretched exponentials. The deviation in the head region of $P(\Omega_z)$ is slightly asymmetric (see top right inset of figure 3.3 (b)) at higher dissipation ($e = 0.5$). This asymmetry vanishes as we move towards elastic limit. The effect of e on $\kappa(\Omega_z)$ is shown in the bottom inset of figure 3.4(b). The translational VDFs in figure 3.4(a) follow a similar behavior as that for $\beta \sim -1$, but the deviations at low and high-velocity regions are more pronounced than for the VDFs of C_i at smooth limit. Both the translational and rotational velocity distributions deviate from a Gaussian even in the elastic limit ($e = 1$) for $\beta = 0$. This is due to the additional rotational dissipation.

The VDFs of both translational and rotational velocity at perfectly rough limit $\beta = 1$ are shown in figure 3.5(a)-(b). The deviations of $P(C_i)$ and $P(\Omega_i)$ from a Gaussian are less as compared to any other roughness ($-1 < \beta < 1$).

The effect of particle roughness on the exponent and prefactor of a distribution of the form $P(x) \sim exp(-\gamma_x x^{\alpha_x})$ (with x = C, Ω) is studied in figure 3.6(a)-(b).

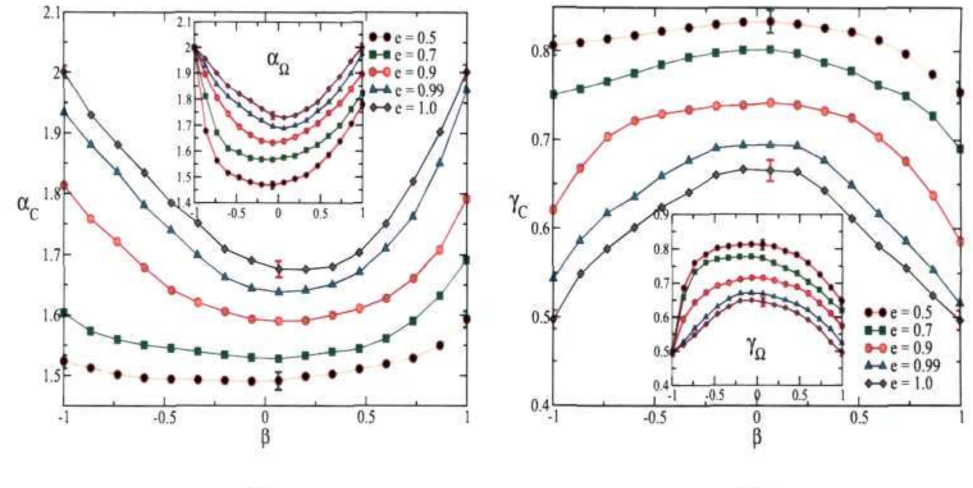

(a) (b)

Figure 3.6: (a) Variation of exponent for the stretched exponential, α_i, with β; translational (main panel, α_C) and rotational (inset,α_Ω) velocity.(b) Variation of prefactor γ_i with β. Typical error-bars are shown on few data points.

The variations of exponents for translational velocity (α_C) and rotational velocity (α_Ω) are shown in main panel and inset of figure 3.6(a), respectively. It is clear that even for perfectly elastic collisions ($e = 1$) the tails of both translational and rotational VDFs deviate from a Gaussian (except at $\beta = \pm 1$ for which $\alpha_C = 2 = \alpha_\Omega$); this deviation is maximum at $\beta \sim 0$. Note that at $e = 1$ the functional

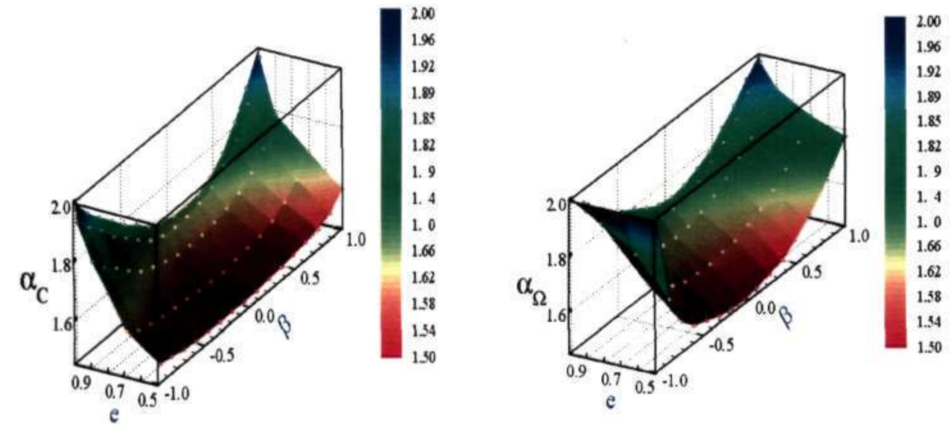

(a) (b)

Figure 3.7: (a) Surface plot for exponent of $P(C_x)$ varing β and e (b) Same as (a) for $P(\Omega_z)$

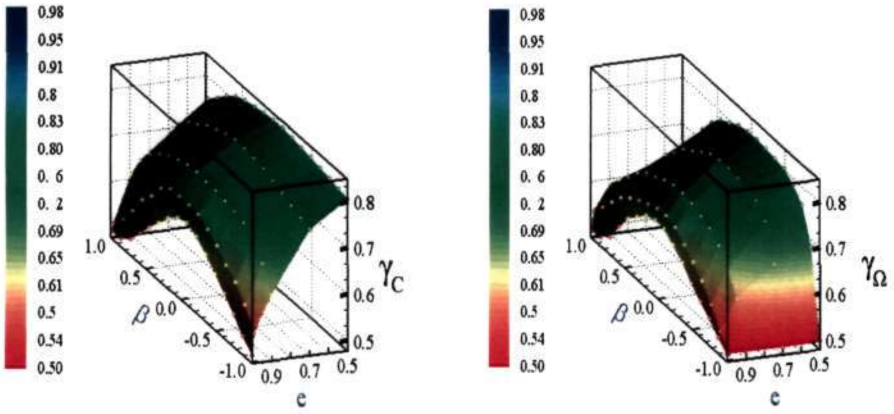

(a) (b)

Figure 3.8: (a) Surface plot for prefactor of $P(C_x)$ varing β and e, (b) Same as (a) for $P(\Omega_z)$

forms of α_C and α_Ω are asymmetric and symmetric (around $\beta = 0$), respectively. With increasing inelasticity, both α_C and α_Ω decrease sharply, and α_Ω also becomes asymmetric around $\beta = 0$. A least square fit to our data suggests that α_i follows a power-law relation with inelasticity:

$$\alpha_i = 2 - A_i(1 - e^2)^{B_i} \tag{3.3}$$

with $i = C, \Omega$, and $(A_C, B_C) \approx (5/8, 2/3)$ at $\beta = -1$ and $(A_C, B_C) \approx (3/4, 1)$ and $(A_\Omega, B_\Omega) \approx (3/8, 7/8)$ at $\beta = 1$. Similarly, the prefactors (γ_C) for translational (main panel) and rotational (γ_Ω) velocity (inset) are shown in figure 3.6(b). For a Gaussian distribution the prefactor γ_i is $1/2$. The deviation from Gaussian is pronounced at $\beta \sim 0$ for any value of normal restitution coefficient (even for perfectly elastic case, e = 1). The deviation starts decreasing if we move towards $\beta = \pm 1$. Same informations about α_i and γ_i are shown as surface plots in 3.7 and 3.8, respectively, as functions of e and β.

3.2 Density and Velocity Correlations

We have studied the effect of normal and tangential restitution coefficients on the pair correlation and the spatial correlation functions.

Pair Correlation Function

The pair correlation function $(g(r))$ is defined as the probability of finding another particle at distance r from a test particle. Thus $g(r)$ gives information about the local spatial ordering of particles. The expression for $g(r)$ is given below (Allen & Tildesley (1987)):

$$g(r) = \frac{2V}{N^2}\langle \sum_{i-1}^{N} \sum_{j>1}^{N} \delta(r - r_{ij}) \rangle \tag{3.4}$$

where V is the volume and N is the number of particles.

Spatial Velocity Correlation

The spatial velocity correlation is given by (Allen & Tildesley (1987)):

$$G_{\zeta\zeta}^{\chi\chi}(r) = \langle \zeta_\chi(R) \zeta_\chi(R + r) \rangle \tag{3.5}$$

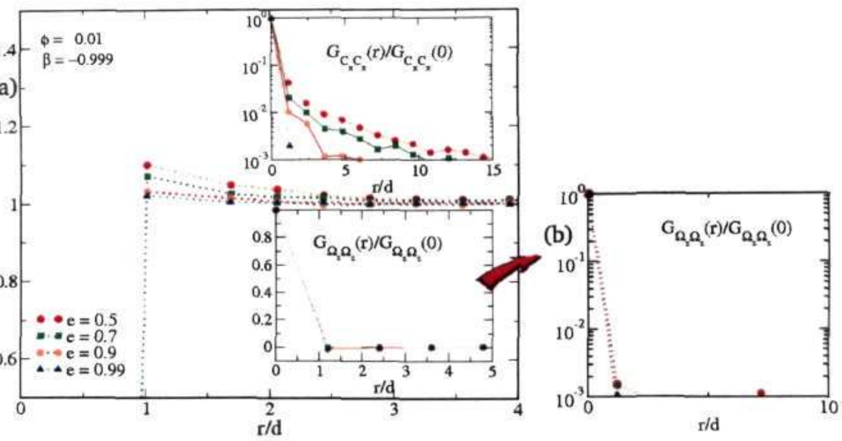

Figure 3.9: (a)Pair correlation function (main panel). Velocity correlation for streamwise translational (top inset) and spanwise rotational velocity (bottom inset) for $\beta = -0.999$ and $\phi = 0.01$. (b) Velocity correlation for spanwise rotational velocity, showing the absolute value.

where $\chi = \{x, y, z\}$ and $\zeta = C, \Omega$. When particle velocities are random , the correlation is zero; a non-zero value of $G^{\chi\chi}_{\zeta\zeta}$ indicates correlation. In figure 3.9(a)

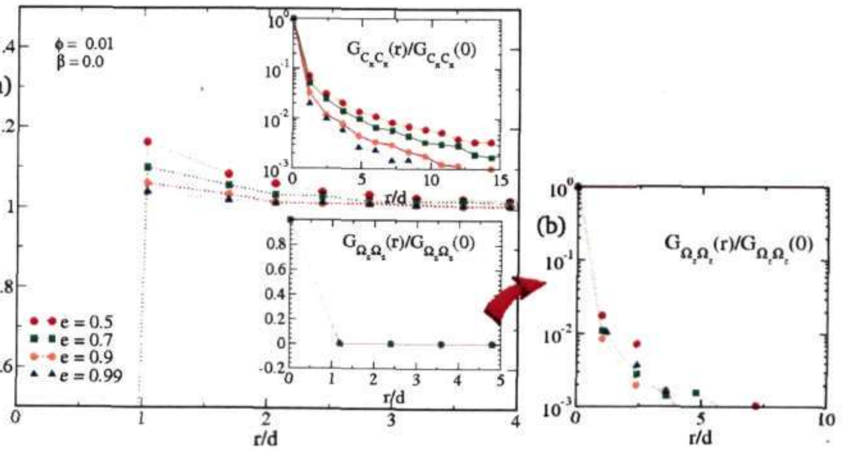

Figure 3.10: Same as in the figure 3.9, but $\beta = 0$

(main panel), the pair correlation function is shown for a dilute granular gas ($\phi = 0.01$) at smooth limit $\beta \sim -1$. No significant correlation for density is observed for any value of e; it behaves almost like a gas. But significant correlation of streamwise velocity, G^{xx}_{CC}, is observed in the top right inset of figure 3.9. This velocity correlation is more pronounced with increasing collisional dissipation. The

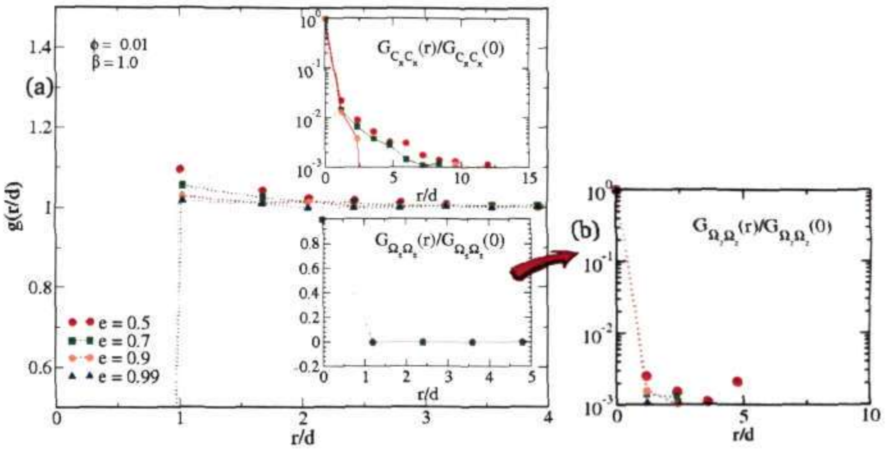

Figure 3.11: Same as figure 3.9 but for $\beta = 1$

correlation for spanwise rotational velocity is shown in the bottom inset of figure 3.9(a). In figure 3.9(b) we have plotted the absolute value of $G^{zz}_{\Omega\Omega}$ which shows that considerable amount of negative correlation exists for Ω_z.

The variation of roughness also has pronounced effect on streamwise velocity correlation (see figures 3.10 and 3.11). Even for quasi-elastic limit ($e \sim 1$) with $\beta = 0$, pronounced velocity correlation for streamwise translational velocity is observed in figure 3.10 as compared to perfectly rough and smooth limits.

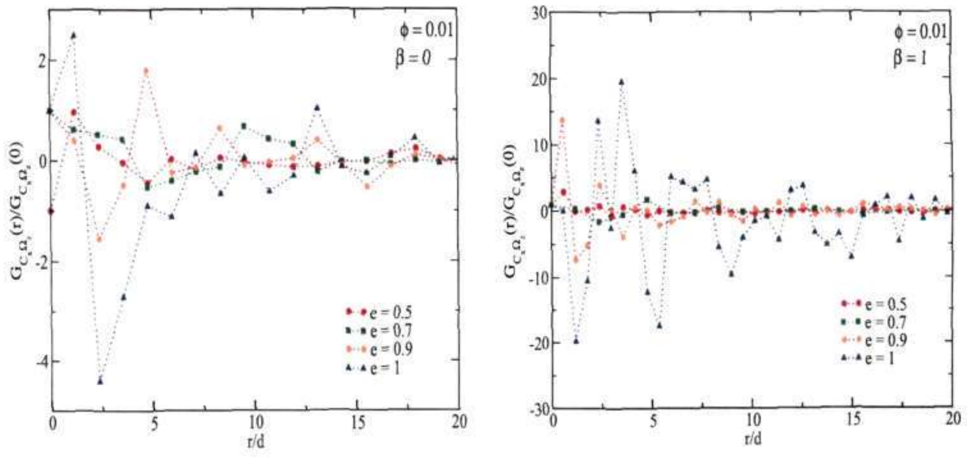

(a) (b)

Figure 3.12: Velocity cross correlation function $G^{xz}_{C\Omega}$ for dilute system with (a) $\beta = 0$ and (b) $\beta = 1$

The velocity correlation between streamwise translational velocity and spanwise rotational velocity $G^{xz}_{C\Omega}$ is shown for $\beta = 0$ and 1 in figure 3.12(a) and (b), respectively. This correlation shows an oscillatory behaviour for nearly elastic system, and the oscillations decrease with increasing dissipation.

3.3 Orientational/Directional Correlation

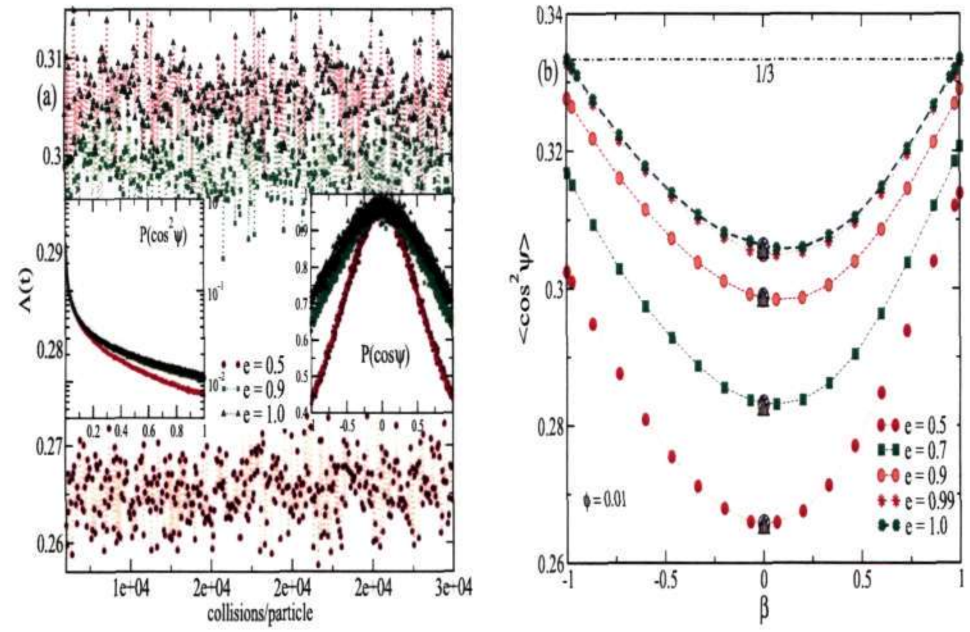

Figure 3.13: (a) Variation of $\Lambda(t) = cos^2\Psi$ with time for different values of e with $\beta = 0, \phi = 0.01$ and $N = 8000$. Left and right insets show the distributions of $cos^2\Psi$ and $cos\Psi$, respectively. (b) Variation of $< cos^2\Psi >$ with β for different e. Larger symbols (triangle and hatched-cycle) at $\beta = 0$ for each e correspond to simulations with $N = 4000$ and 16000, respectively.

The translational and rotational fluctuating velocities are not "directionally" correlated in a molecular gas, but such an "orientational" correlation has recently been found in a freely cooling granular gas (Brilliantov *et al.* (2007)). According to Brilliantov *et al.* (2007), the orientational/directional correlation between translational and rotational velocities is quantified in terms of the mean square of the cosine of the angle Ψ, between $\mathbf{C} = \mathbf{c} - < \mathbf{c} >$ and $\mathbf{\Omega} = \omega - < \omega >$:

$$\Lambda(t) = \frac{1}{N} \sum_{i=1}^{N} \frac{(\mathbf{C}_i \cdot \mathbf{\Omega}_i)^2}{(C_i^2 \Omega_i^2)} = \frac{1}{N} \sum_{i=1}^{N} cos^2 \Psi_i \tag{3.6}$$

For a molecular gas, Λ is $1/3$. In figure 4.27(a) the temporal evolution of $\Lambda(t)$ (main panel) for different values of normal restitution coefficient(e) is shown, with the tangential restitution coefficient being set to $\beta = 0$. The corresponding probability distributions of $cos^2\Psi$ and $cos\Psi$ are shown in left and right panels, respectively. $P(cos\Psi)$ is symmetric about the zero mean for all e, but its width becomes narrower with decreasing e. From the main panel and left inset, we find that even for perfectly elastic collisions ($e = 1$), the mean value of $\Lambda(t)$ deviates from $1/3$ (for a molecular gas), signaling the presence of *orientational* correlation.

The variation of the temporal average of $\Lambda(t)$ with particle roughness, β, is shown in figure 4.27(b); the dot-dash line represents the limiting value of $1/3$ for a molecular gas. Note that the data points for $e = 1$ (thick blue dashed line) and $e = 0.99$ almost overlap with each other. For any value of e, the *orientational* correlation is maximum at $\beta \sim 0$ and it decreases *monotonically* as we approach the perfectly smooth ($\beta = -1$) and perfectly rough ($\beta = 1$) limits. This latter observation is in contrast to that in a freely cooling dilute granular gas (Brilliantov *et al.* (2007)) for which $< \Lambda >$ varies nonmonotonically with β for $-1 < \beta < 0$ and $0 < \beta < 1$. Most importantly, unlike in its freely cooling granular gas counterpart, the case of quasi-elastic collisions ($e \sim 1$) appears to be non-singular in a shear flow in the sense that the orientational correlation smoothly decreases to its uncorrelated value ($1/3$) for both the perfectly smooth ($\beta = -1$) and rough ($\beta = 1$) limits.

3.4 Effect of Coulomb friction: Variable-β model

Here we present results with coulomb friction model i.e. instead of constant-β model, the collision-angle dependent $\beta(\gamma)$ is used at the time of collision. The coefficient of friction is also an important parameter for the determination of β:

$$\beta(\gamma) = min \left\{ \beta_0, -1 + \mu(1+e) \left(1 + \frac{1}{K}\right) cot\gamma \right\}, \tag{3.7}$$

where β_0 is the critical value of particle surface roughness.

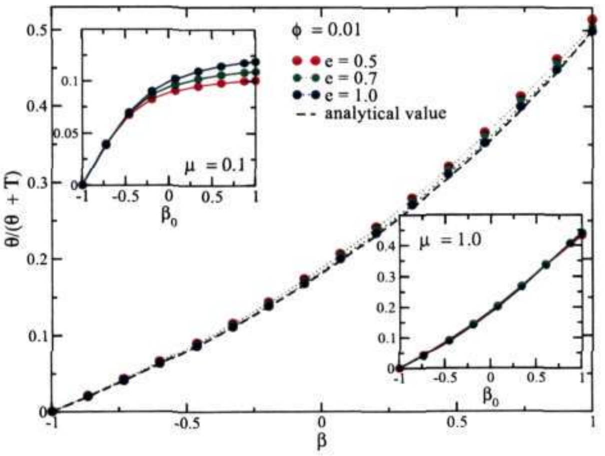

Figure 3.14: In main panel the effect of roughness on temperature ratio $\theta/(\theta+T)$ for different values of e for $\phi = 0.01$ with constant β model. Temperature ratio based on variable-β model for friction coefficient $\mu = 0.1$ and 1.0 in the top left and bottom right inset, respectively.

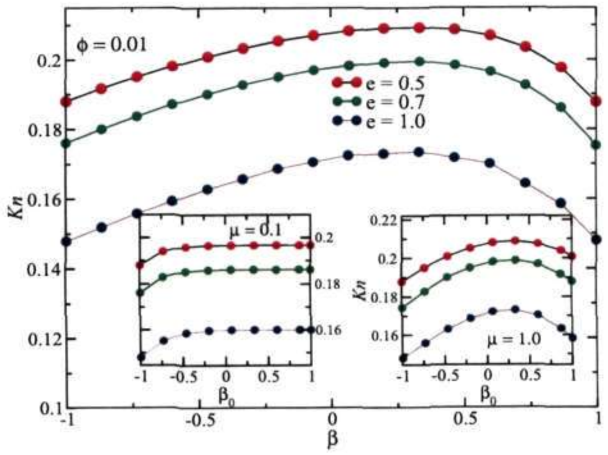

Figure 3.15: Effect of roughness on Knudsen Number Kn for different values of e for $\phi = 0.01$ in main panel for constant-β model. Insets for results based on variable-β model. Left and right insets for $\mu = 0.1$ and 1.0, respectively.

3.4.1 Effect of friction on temperature ratio and orientational correlation

The variation of temperature ratio, $\theta/(\theta+T)$, for different values of roughness parameter β, taken constant throughout the simulation, is shown in the main panel of figure 3.14. The black dashed line is representing the theoretical prediction for

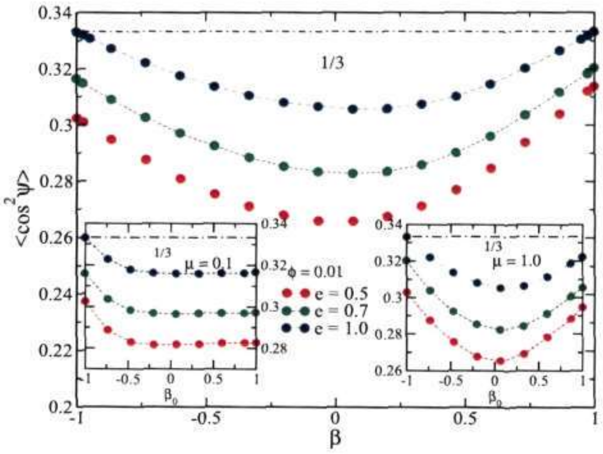

Figure 3.16: Effect of roughness on orientational correlation for different values of e for $\phi = 0.01$ in main panel for constant β model. Insets for results based on variable-β model. Left and right insets for $\mu = 0.1$ and 1.0, respectively.

temperature ratio (Huthmann & Zippelius (1997*b*),Lun & Savage (1986), Gayen & Alam (2006)). Now with variable-β model, the effect of critical roughness parameter β_0 on temperature ratio is plotted for different values of e, setting the coulomb friction $\mu = 0.1$, in the top left inset of figure 3.14. The same set of results is shown for $\mu = 1.0$ in the bottom right inset of figure 3.14. At lower value of Coulomb friction ($\mu = 0.1$), the value of temperature ratio monotonically increases with critical β_0 and starts deviating from the constant-β model for $0 < \beta_0 < 1$. This deviation is more if we increase collisional dissipation. For $\mu = 1.0$, the value of temperature ratio is independent of the normal restitution coefficient and the deviation from the constant-β model occurs only at higher values of β_0. If we further increase the value of μ, $\theta(\theta + T)$ based on both models agree with each other (not shown).

The variation of Knudsen Number, Kn, at any value of critical particle roughness β_0 depends on Coulomb friction. The main panel of figure 3.15 is the same as figure 3.2. At lower friction ($\mu = 0.1$) for any values of e, starting from smooth limit $\beta_0 \sim -1$, Kn increases with β_0 and then becomes constant. With increasing collisional dissipation, Kn increases and follow the same trend as we have seen in constant-β model. For $\mu = 1.0$ (right inset of figure 3.15), after reaching a maximum value, Kn starts decreasing monotonically as in the constant-β model.

The friction coefficient μ has a pronounced effect on orientational correlation $\Lambda(t)$. Figure 3.16 shows a comparison between constant-β and variable β models.

In the main panel the effect of roughness on $\langle\Lambda(t)\rangle$ is same as in figure 4.27(b). The left and right insets show the effect of friction coefficient on $\langle\Lambda(t)\rangle$. In the left inset of figure 3.16, Λ is calculated by varying the critical roughness β_0 for $\mu = 0.1$. After a certain value of $\beta_0 \sim -0.75$, Λ is independent of the critical roughness parameter, irrespective of normal restitution. For higher friction ($\mu = 1.0$), the orientational correlation follows the same trend with roughness as in the case of constant-β model (right inset of figure 3.16). Note that for elastic case ($e = 1$) and perfectly rough limit ($\beta_0 \sim 1$), there is considerable orientational correlation for $\mu = 1.0$. This correlation at elastic limit ($e \sim 1$) with $|\beta| \sim 1$ vanishes for larger values of friction coefficient.

3.4.2 Effect of Friction on Velocity Distribution Function

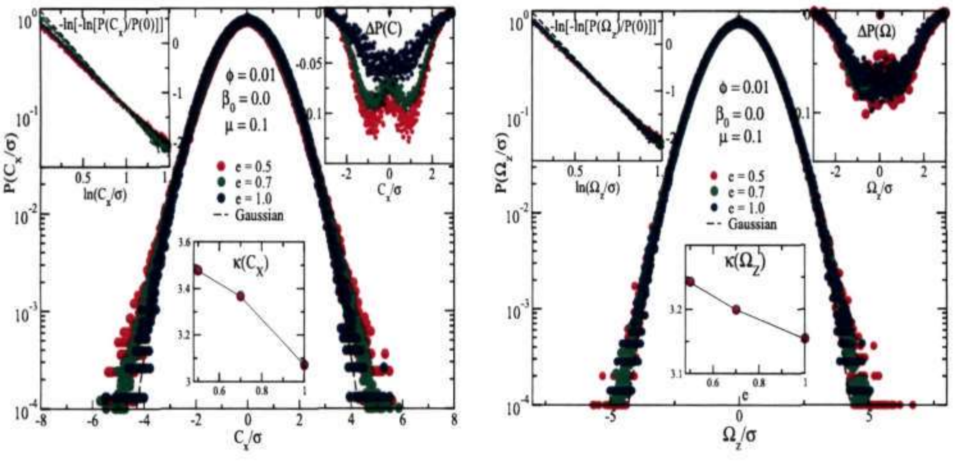

(a) (b)

Figure 3.17: (a) VDF based on variable-β model for C_i (main panel) for $\beta_0 = 0$, $\mu = 0.1$ and $\phi = 0.01$. Top left inset shows of $-ln[-ln[P(x/\sigma)/P(0)]]$ with $ln(x/\sigma)$; top right inset depicts deviation at low-velocity region. The bottom inset shows the effect of e on the kurtosis of the ditribution. (b) Same as panel (a) for Ω_z

Figures 3.17-3.19 show the effects of friction coefficient on VDFs for the critical roughness $\beta_0 = 0$. Results are taken for three particular values of friction parameter, $\mu = 0.1, 1.0$ and 10.0 as shown in figures 3.17, 3.18 and 3.19, respectively. In every figure the top left inset shows the variation of $-ln[-ln[P(x/\sigma)/P(0)]]$ with $ln(x/\sigma)$, with $x = C, \Omega$. The deviation in low velocity region in linear scale is depicted in the top right inset and the bottom inset shows the variation of kurtosis with normal restitution coefficient. If we increase the value of friction coefficient, the VDFs deviate more from a Gaussian. The asymmetry in the low velocity region of $P(\Omega_z)$ appears with increment of friction parameter, μ at $e = 0.5$. At large values of μ the VDFs for C_i and Ω_i fairly agree with the VDFs based on constant-β model. The deviation is more pronounced between two models at small values of friction coefficient and at a critical value of roughness close to $\beta_0 = 1$.

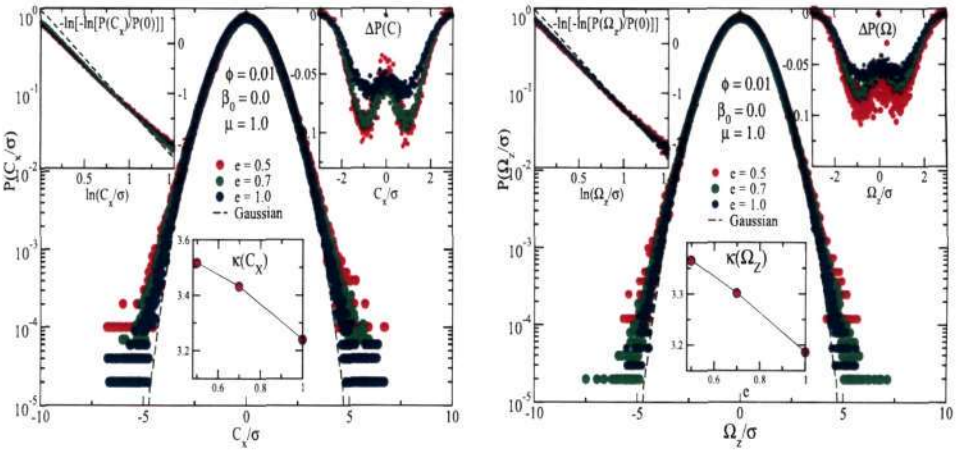

(a) (b)

Figure 3.18: Same as figure 3.17 but $\mu = 1$

The effects of Coulomb friction is summarised in figures 3.20 (a) and (b). Figure 3.20(a) shows the effect of friction coefficient on the kurtosis of $P(C_x)$ for different dissipation levels in the main panel and the inset shows the same for spanwise rotational velocity; critical roughness β_0 is set to 0. The kurtosis of both velocities increases with Coulomb friction and after reaching a large value it becomes a constant. Figure 3.20 (b) shows the variation of the exponents of tails of $P(C_x)$ and $P(\Omega_z)$ (main panel and bottom inset, respectively) over μ for different normal restitution coefficient e. With increasing value of μ, the exponents (α_C and α_Ω) decrease, signalling more deviation from a Gaussian. Therefore, in the variable-β model, μ is one of the essential parameters in energy transfer process between translational and rotational motions, along with critical roughness β_0.

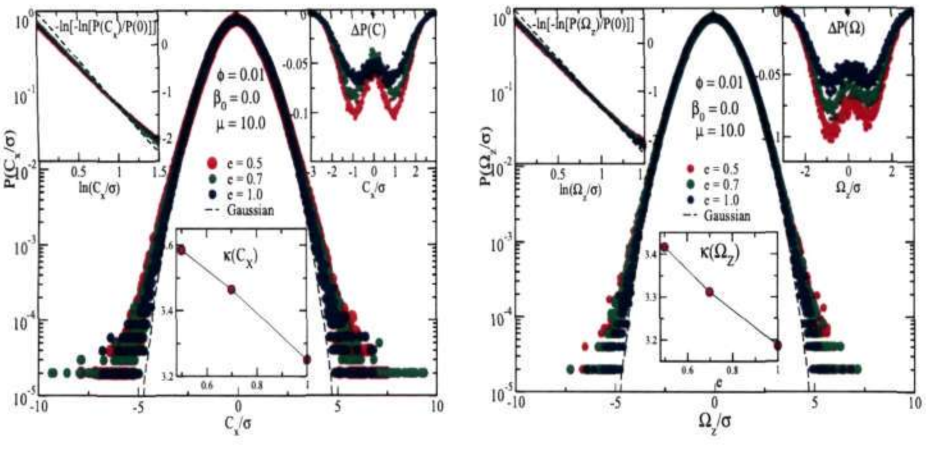

(a) (b)

Figure 3.19: Same as figure 3.17 but $\mu = 10$

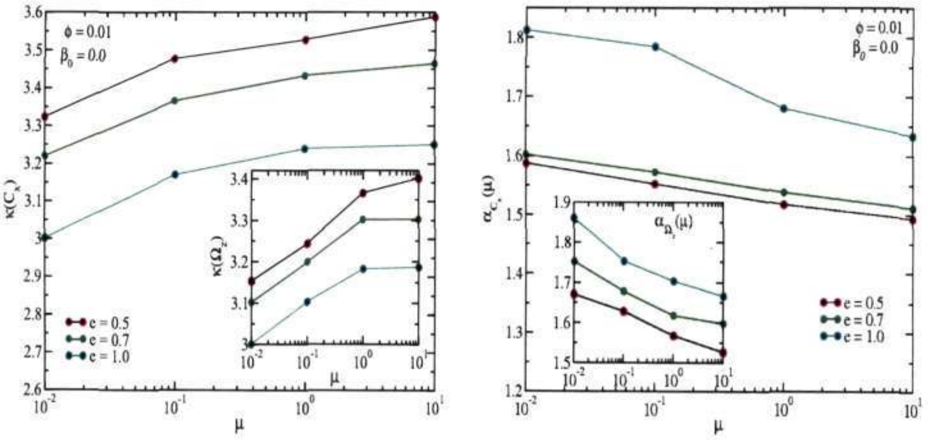

(a) (b)

Figure 3.20: (a) Variation of kurtosis for streamwise translational and spanwise rotational velocity on friction coefficient, μ, for different values of e in main panel and in the inset, respectively. (a) Effect of μ on exponent of streamwise translational and spanwise rotational velocity in main panel and inset, respectively.

Chapter 4

EFFECT OF DENSITY: VELOCITY FLUCTUATION AND CORRELATION

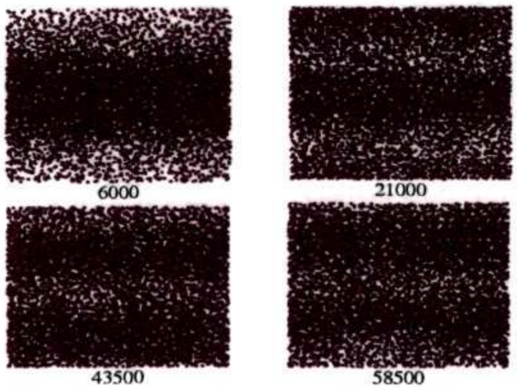

Figure 4.1: Projected particle snapshots in xy-plane at steady state for $\phi = 0.3$, $\beta = 0$ and $e = 0.5$. Number below each snapshot denotes time instant given in terms of collisions per particle.

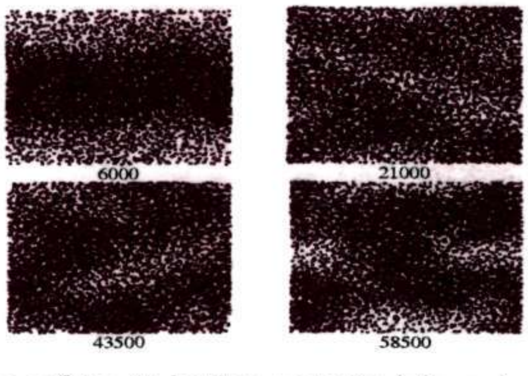

Figure 4.2: Same as figure 4.1 but here projection is in yz-plane.

In this chapter we investigate the effects of density (particle volume fraction) on velocity distribution functions and various correlations. The variation of system density not only changes the dynamics of the flow, but has great effects on various system properties, like local density distribution, orientational correlation, VDF, pair correlation and velocity correlation function.

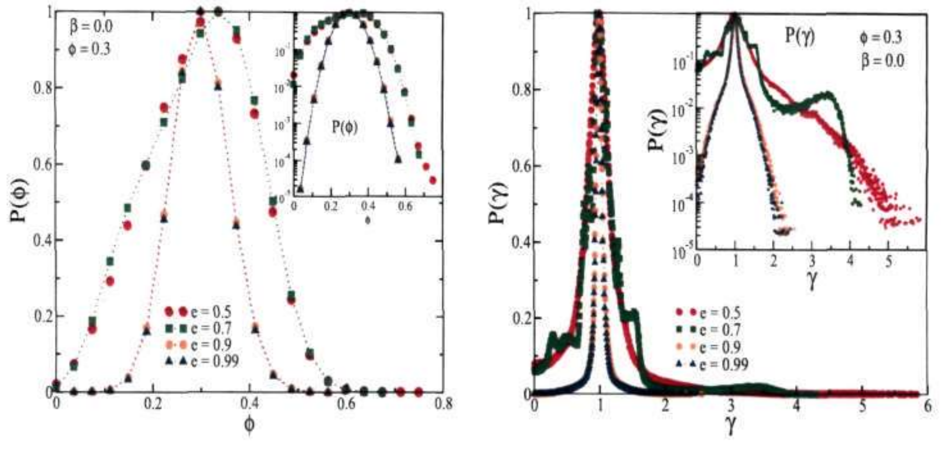

(a) (b)

Figure 4.3: (a) Probability distribution of local density for different normal restitution, e (main panel); inset is same as in main panel, but $P(\phi)$ is in log scale. (b) Local shear rate, $\dot{\gamma}$, distribution for different collisional dissipation in linear scale and log-scale in main panel and top right inset, respectively.

Figures 4.1 and 4.2 show some typical snapshots of particles projected in xy and yz-plane, respectively, for a moderate volume fraction $\phi = 0.3$, with $\beta = 0.0$ and $e = 0.5$. The local clusters, formed over the domain, make the system inhomogeneous both in xy and yz-plane. These clusters are unstable and change with time. This also indicates the multi-steady states possessed by the system. This type of dissipation-induced density-inhomogeneity is observed for moderately dense systems with large number of particles.

The probability distribution of mean-density, $P(\phi)$, is shown in figure 4.3(a); to calculate $P(\phi)$ we divide the computational into 10x10x10 cells and then take average over a few thousands snapshots. In the quasi elastic limit $e \sim 1$, the system is almost uniform. The local density varies significantly as we increase dissipation. Figure 4.3(a) shows that for higher dissipation level ($e = 0.5$) there is about 90% chance of finding local cells having density $\phi \sim 0.25 - 0.4$. The variation of local shear-rate $\dot{\gamma}$ for different collisional dissipation is shown in figure 4.3(b). At elastic limit $e \sim 1$, $P(\dot{\gamma})$ is symmetric about the mean of the distribution; this symmetry

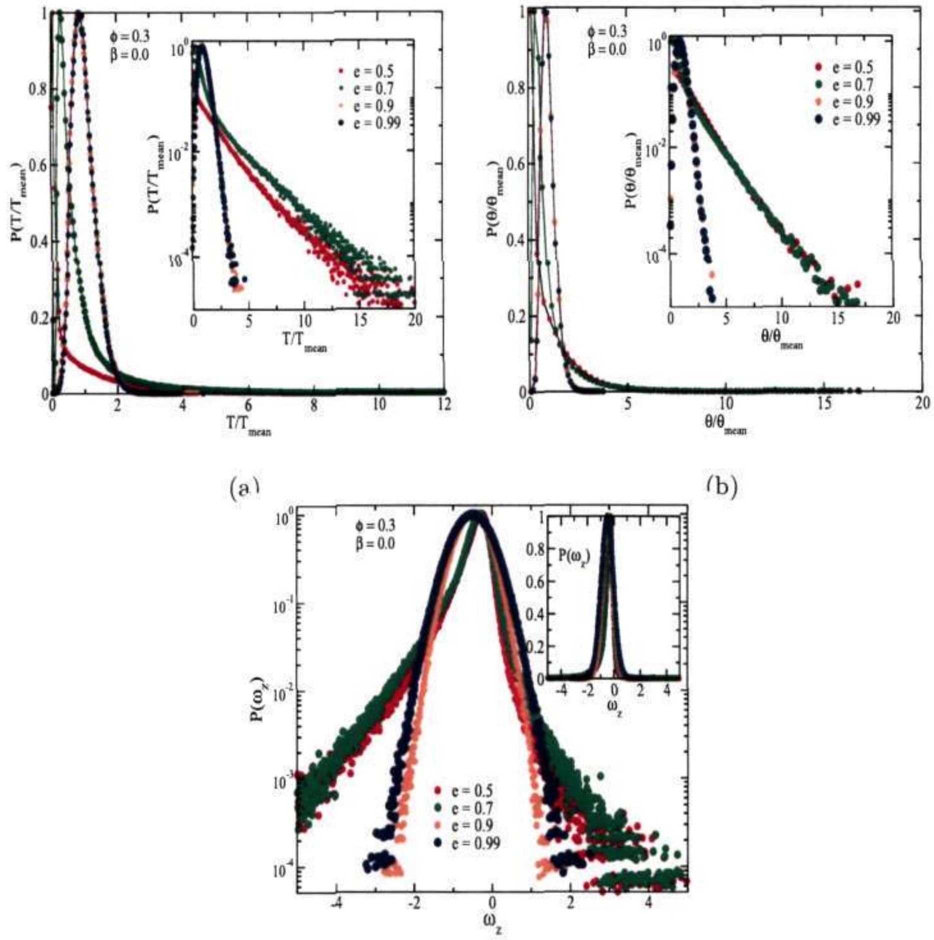

(a) (b)

(c)

Figure 4.4: (a) Probability distribution of local translational temperature for different normal restitution, e (main panel); inset is same as in main panel, but $P(\phi)$ is in log scale. (b) Probability distribution of local rotational temperature in linear scale and log-scale in main panel and top right inset, respectively. (c) Probability distribution for spanwise rotational velocity in log-scale (main panel) and in linear scale (inset).

breaks down with increase of inelasticity. The probability distribution function of T, θ and ω_z are shown in figures 4.4(a), 4.4(b) and 4.4(c), respectively. The shape of each distribution changes drastically for $e \leq 0.7$, signalling the onset of cluster formation.

4.1 Velocity Distribution Function (VDF)

In this secetion we represent results on velocity distribution functions (VDF) of dense flows for constant-β model. The results are presented for particle volume fractions of $\phi = 0.3$ and $\phi = 0.5$. Another set of results for a lower volume frction $\phi = 0.1$ look similar to those of $\phi = 0.3$ which is documented in Appendix I.

4.1.1 Moderately Dense Flow

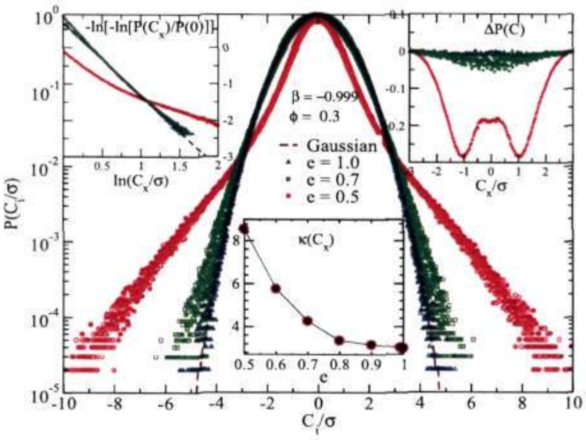

Figure 4.5: Translational velocity distribution for $\phi = 0.3$ for $\beta = -0.999$

Here we study moderately dense flow by fixing the volume fraction to $\phi = 0.3$. For smooth limit $\beta \sim -1.0$, the probability distribution of translational fluctuating velocity $P(C_i)$ is shown in figure 4.5 along with the variation of kurtosis (lower inset) for different values of e. For higher dissipation ($e = 0.5$), the deviation is pronounced with $\kappa(C_x) \sim 8.5$. The upper left inset in figure 4.5 shows the variation of $-ln[-ln[P(C_x/\sigma)/P(0)]]$ with $ln(C_x/\sigma)$. At low-velocity regions, the deviation from a Gaussian is calculated from $\Delta P(x) = P(x) - exp(-x^2/2)$, with $x = C/\sigma, \Omega/\sigma$, which is shown in the top right inset of figure 4.5. The deviation for low-velocities increases with increasing collisional dissipation.

The most dissipative case, $\beta = 0$, is studied in figure 4.6. An interesting observation is that the VDF of streamwise translational velocity undergoes a transition from an stretched exponetial to a Gaussian with under-populated tails with increasing e. The variation of kurtosis with normal restitution coefficient e, in the bottom

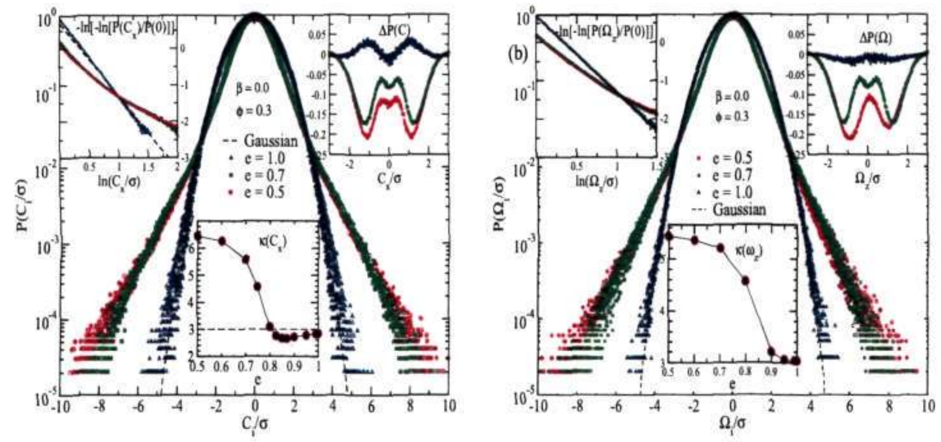

(a) (b)

Figure 4.6: (a) Translational and (b) rotational velocity distributions for $\phi = 0.3$ and $\beta = 0$

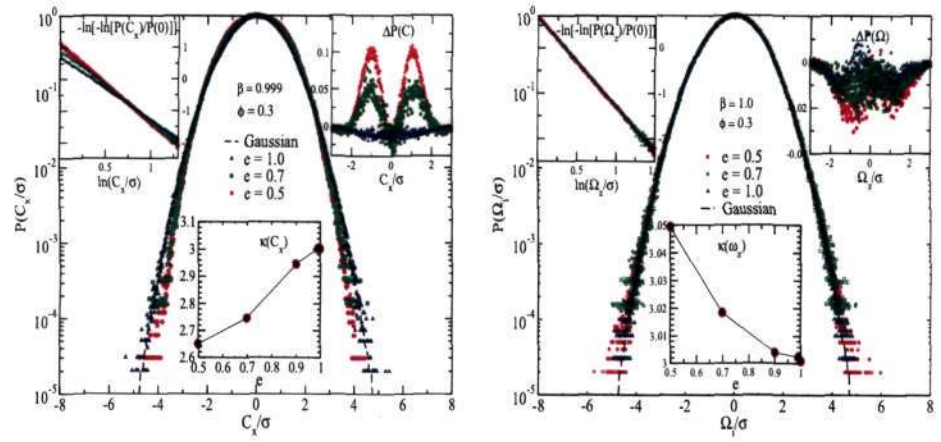

(a) (b)

Figure 4.7: (a) Translational and (b) rotational velocity distributions for $\phi = 0.3$ and $\beta = 1$

inset of figure 4.6(a), indicates that this transition occurs at $e \sim 0.8$. For $P(\Omega_z)$, a transition is observed from a Gaussian to an stretched exponential to an exponential with decreasing e as seen in the lower inset of figure 4.6(b). It may be pointed out that the kurtosis of an exponential distribution is 6 and that of a Gaussian is 3.

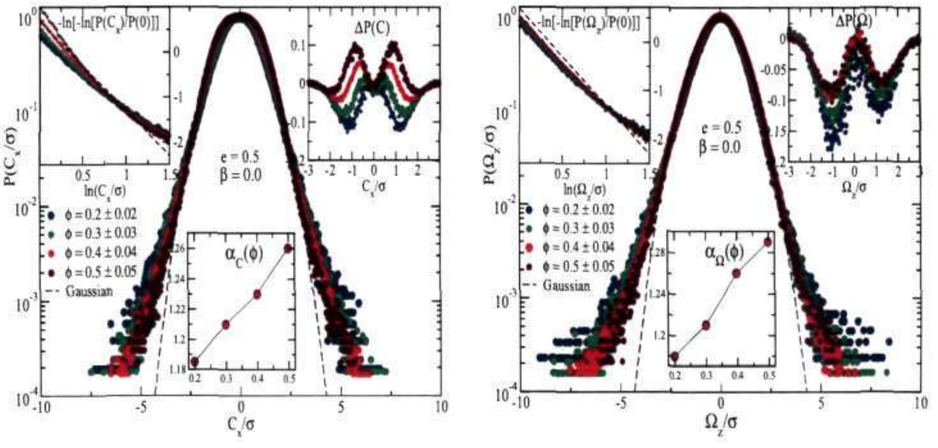

(a) (b)

Figure 4.8: "Local" velocity distribution with varying local cell-density for (a) translational and (b) rotational velocity for e = 0.5 and $\beta = 0.0$

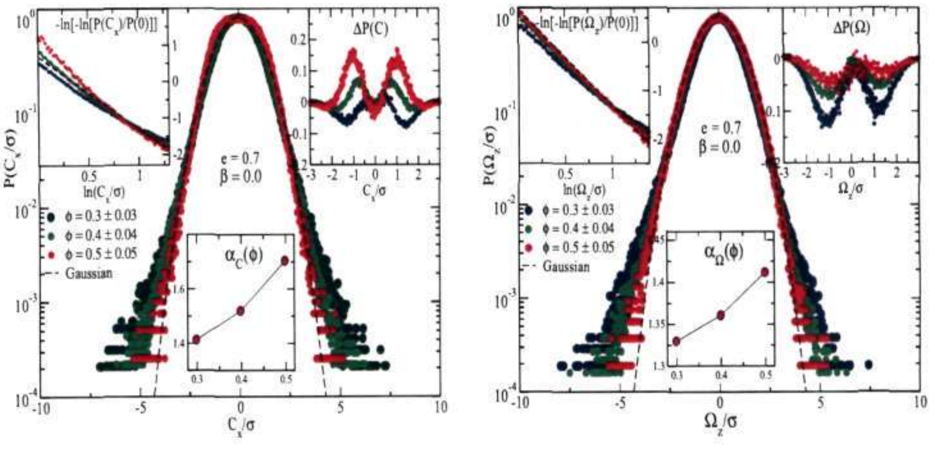

(a) (b)

Figure 4.9: "Local" velocity distribution with varying local cell-density for (a) translational and (b) rotational velocity for e = 0.7 and $\beta = 0.0$.

For perfectly rough limit ($\beta \sim 1$), $P(C_i)$ and $P(\Omega_i)$ are shown in figures 4.7(a) and 4.7(b), respectively. For $P(C_x)$ a transition from an under-populated tail to a Gaussian is observed with increasing e.

The above study of $P(C_i)$ and $P(\Omega_i)$ does not reveal true picture about 'local' VDFs since the system has a wide variation in local density (especially at $e = 0.5$,

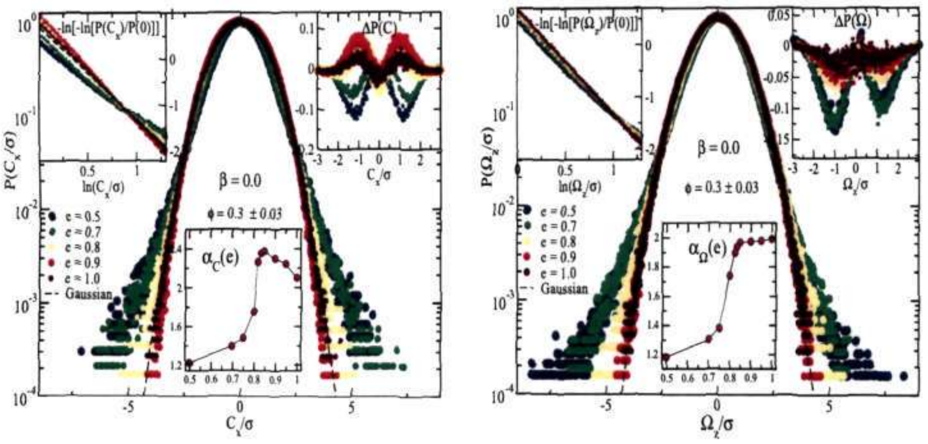

(a) (b)

Figure 4.10: Effect of e on local velocity distribution for $\beta = 0.0$ and local density $\phi = 0.3 \pm 0.03$ for (a) translational and (b) rotational velocity

0.7) as shown in 4.3. The results in figures 4.5-4.7 only provide a weighted probability distribution of $P(C_i)$ and $P(\Omega_i)$ taking the whole range of local density variation $(0.2 - 0.5)$ for a particular value of e. Note that this density variation is prominent for $e \leq 0.7$ for our system.

To study "local" VDFs we have chosen four specific values of local volume fraction $\phi = 0.2, 0.3, 0.4$ and 0.5. First we pick up those cells having an average local density of $0.2 \pm 10\%$, and calculate the probability distributions of C_i and Ω_i for particles belonging to those cells. Similarly we go for cases with local cell densities of $\phi = 0.3, 0.4$ and 0.5. The local probability distributions of C_x and Ω_z for $\beta = 0.0$ and $e = 0.5$ are shown in figure 4.8. The deviation of $P(C_x)$ and $P(\Omega_z)$ from Gaussian is more for lower density regions compared to denser parts of the system. The tails of both $P(C_x)$ and $P(\Omega_z)$ follow an stretched exponential

$$P(x) \sim e^{-\gamma_i x^{\alpha_i}}, \quad \text{with} \quad x = C_i/\sigma \quad \text{or} \quad \Omega_i/\sigma$$

where γ_i and α_i are the prefactor and exponent of distribution. There is a linear rise of exponent with increase of local cell density as shown in the bottom insets of figure 4.8. For $\Delta P(\Omega)$, an asymmetry is observed in the head-region for lower dense parts of the system as shown in the top right inset of figure 4.8(b). Similar

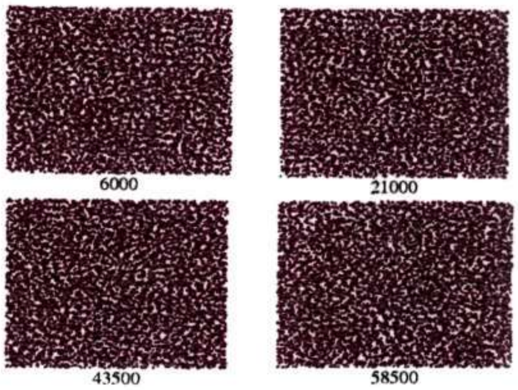

Figure 4.11: Projected particle snapshots in xy-plane at steady state for $\phi = 0.5$, $\beta = 0$ and $e = 0.7$. Number below any snapshot denotes time instant given in terms of collisions per particle.

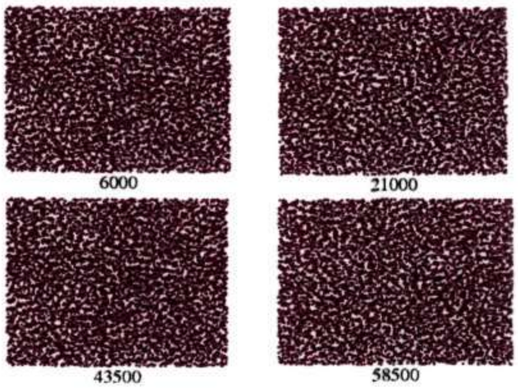

Figure 4.12: Same as figure 4.1 but here projection in yz-plane.

results for $P(C_x)$ and $P(\Omega_z)$ with $e = 0.7$ and $\beta = 0.0$ are shown in figure 4.9 by varying local cell-density $\phi \sim 0.3 - 0.5$ with 10% tolerance.

Now to summarize the case $\beta = 0.0$ we have taken all C_x and Ω_z in those cells having an average "local" density same as the "overall" system density i.e. $\phi = 0.3$ with 10% tolerance and varied the normal restitution coefficient e. The probability distributions of C_x and Ω_z are plotted in figure 4.10 for $e = 0.5, 0.7, 0.8, 0.9$ and 1.0. The most interesting observation is that there is a sharp transition from an stretched exponential tail ($\alpha_C < 2$) to an under-populated Gaussian tail ($\alpha_C > 2$) for $P(C_x)$ at $e > 0.8$, clearly seen in the bottom inset of 4.10(a). For $P(\Omega_z)$, however, the tails undergo a transition from an stretched exponential ($\alpha_\Omega < 2$) to a Gaussian ($\alpha_\Omega = 2$) with increasing e, see the bottom inset of figure 4.10(b). From

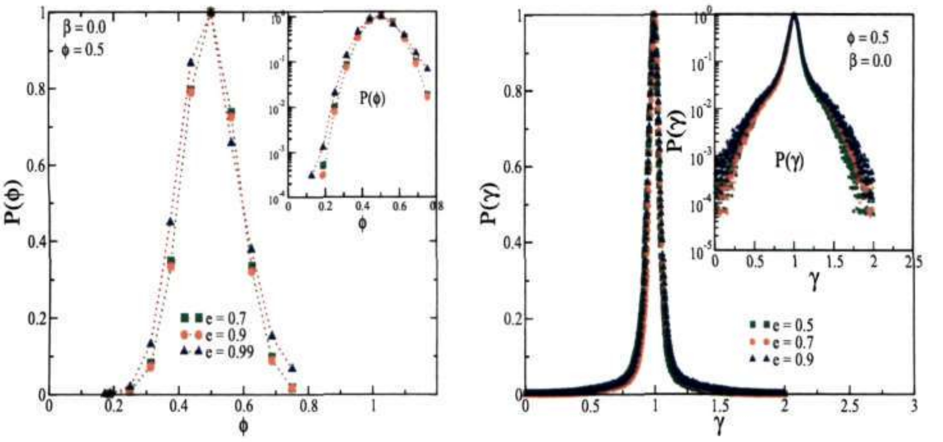

(a) (b)

Figure 4.13: Same as figure 4.3 but $\phi = 0.5$.

the right inset og figure 4.10(b), we find that the asymmetry for low velocities of Ω_z, (Ω_z), becomes prominent for $e \leq 0.7$.

4.1.2 Dense Flow

Here we briefly discuss the VDFs of dense flows by setting the overall system volume fraction to $\phi = 0.5$ which is close to the freezing-point density of hard spheres in three dimension. Figures 4.11 to 4.14 are analogues of figures 4.1 to 4.4 for $\phi = 0.5$. For dense flows, the main observation is that the system is almost homogeneous and there is no discernible dissipation-induced density inhomogeneity even at $e = 0.5$.

The VDFs for both translational and rotational velocities are shown in figures 4.15-4.17. For any value of particle roughness, β, the VDF of C_x follows a Gaussian with under-populated tails. The reason behind this under-populated distribution can be explained on the basis of system density. At higher system density, the random movement of particles is restricted which results in less fluctuations in the particle motion.

Figures 4.18 and 4.19 show the local VDFs of C_x and Ω_z for $e = 0.7$ and 0.9, respectively. The VDFs of C_x is more under-populated as we move towards the

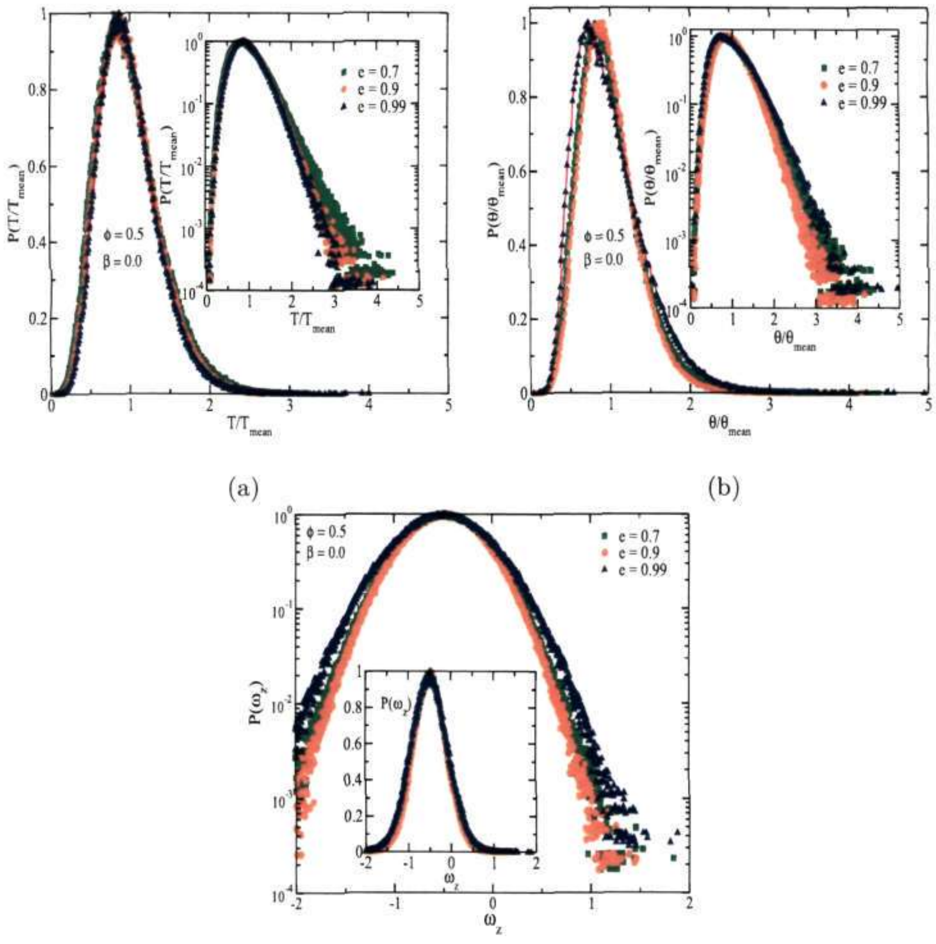

(a) (b)

(c)

Figure 4.14: Same as figure 4.4 but for system density $\phi = 0.5$.

denser zones of the same system (see the variation of exponents, $\alpha_C(\phi)$, with local density in the lower inset of figures 4.18(a) and 4.19(a)). For $P(\Omega_z)$, however, the tails are over-populated ($\alpha_\Omega < 2$) and approach a Gaussian with increasing local density. Another difference with results for $\phi = 0.3$ is that the deviation of $P(\Omega_z)$ at low velocities remain symmetric about $\Omega_z = 0$ as seen in right upper insets of figures 4.18(b) and 4.19(b).

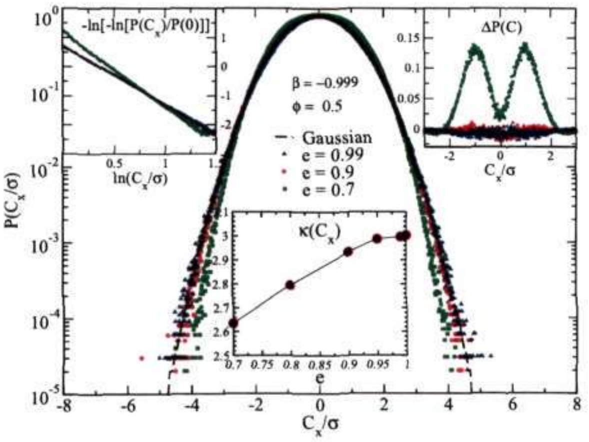

Figure 4.15: Translational velocity distribution for $\phi = 0.5$ and $\beta = -0.999$

4.2 Effect of Density on VDFs with Coulomb Friction

In this section, all results are presented for the 'variable-β' model which incorporates Coulomb friction. As in the dilute system, Coulomb friction has strong effects on temperature ratio, $\theta/(\theta + T)$, VDFs, etc.

In the main panel of figure 4.20, the effect of β on temperature ratio is shown for different values of e for 'constant-β' model. The black dashed line indicates theoretical prediction of temperature ratio. For the 'variable β' model, the variation of temperature ratio on critical roughness β_0 with $\mu = 0.5$ is plotted in the right inset, and the left inset shows the effect of friction coefficient, μ, on temperature ratio for which β_0 is set to 0. It is observed that for low values of friction coefficient ($\mu < 10^{-2}$) the temperature ratio is independent of both roughness and normal restitution coefficient. In the range $10^{-2} < \mu < 1$ with any value of critical roughness β_0, the temperature ratio sharply increases with μ; after $\mu > 1$ this ratio becomes a constant. Figure 4.20 also tells us that the temperature ratios based on both 'constant-β' and 'variable- β' models agree with each other upto a large value of β for higher friction coefficient μ. These observations mirror those in the recent work of Herbst *et al.* (2005) for a heated granular gas.

In figure 4.21, the "local" VDFs for C_x and Ω_z are shown with parameters as

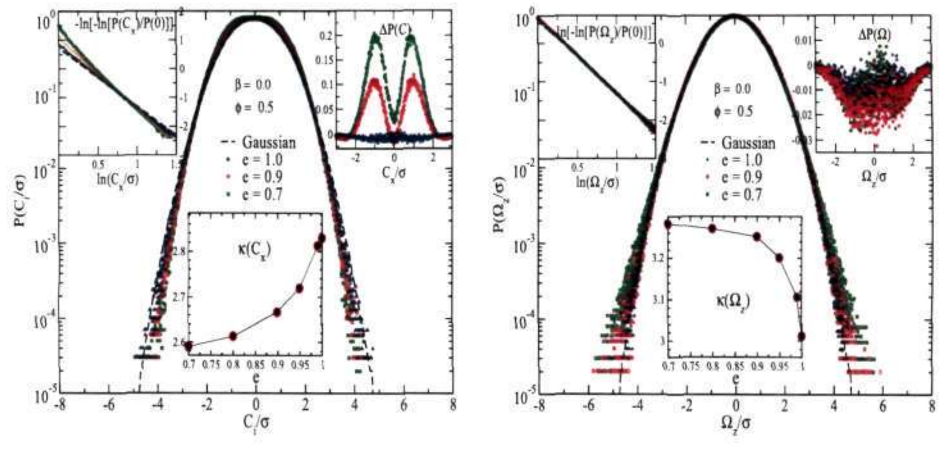

(a) (b)

Figure 4.16: (a) Translational and (b) rotaional velocity distribution for $\phi = 0.5$ and $\beta = 0$

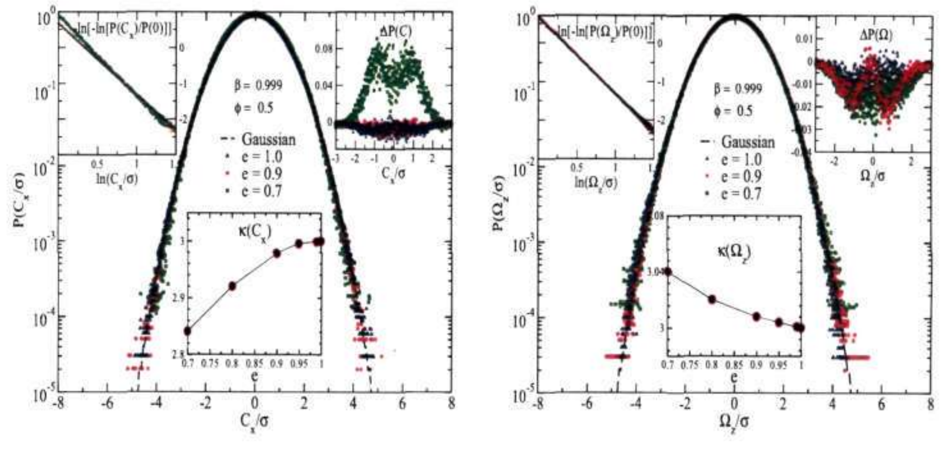

(a) (a)

Figure 4.17: (a) Translational and (b) rotational velocity distributions for $\phi = 0.5$ and $\beta = 1$.

in figure 4.8, but the value of the coefficient of friction, μ, is taken as 0.1 and other parameters are $\beta_0 = 0$ and $e = 0.5$. The same set of results for $e = 0.7$ is shown in figure 4.22. As before, the tails of $P(C_x)$ deviate more for lower local density compared to the denser zone. (This deviation also depends on μ that we will see later). A pronounced asymmetry between two tails is observed in the VDF of Ω_z

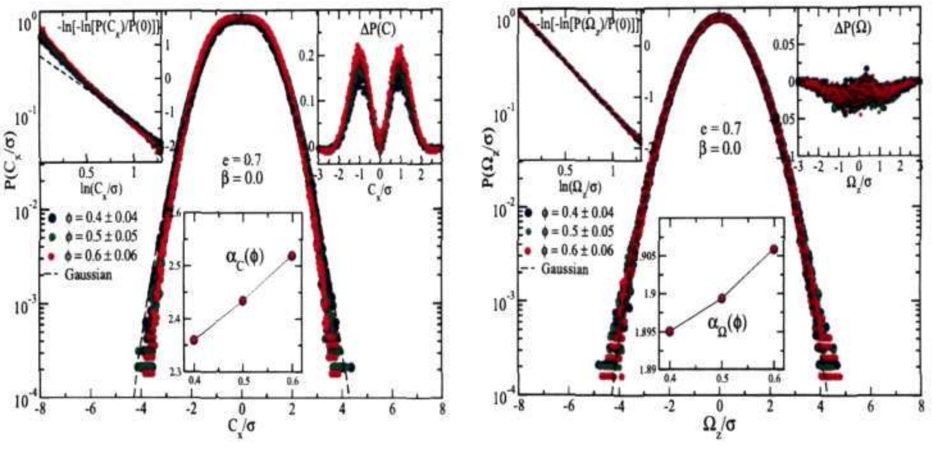

(a) (b)

Figure 4.18: Local velocity distributions with varying cell-density for $e = 0.7$ and $\beta = 0$

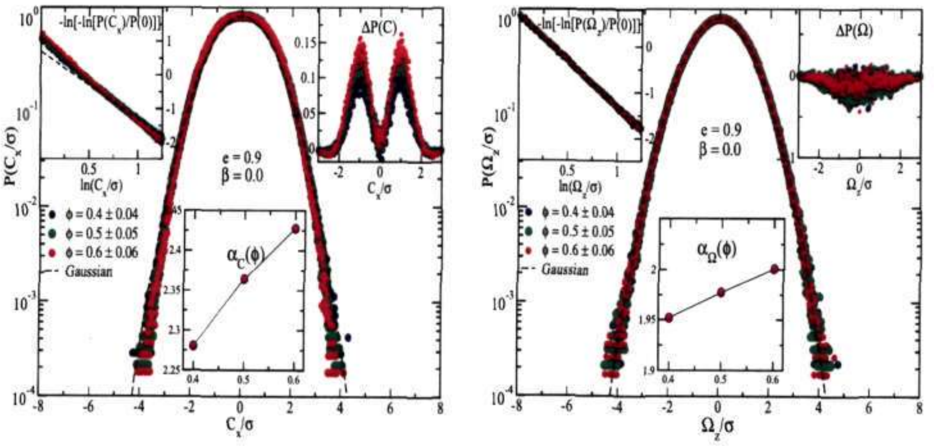

Figure 4.19: Same as figure 4.18 for $e = 0.9$

in figures 4.21(b) and 4.22(b). We calculate skewness (λ) to get an idea of this asymmetry quantitatively:

$$\lambda = \frac{\mu_3}{\mu_2^{3/2}}, \tag{4.1}$$

where

$$\mu_3 = \int_{-\infty}^{\infty} (x - \bar{x})^3 f(x) dx, \quad \mu_2 = \int_{-\infty}^{\infty} (x - \bar{x})^2 f(x) dx \tag{4.2}$$

are the third and second moments about the mean of the distribution, respectively. The variation of skewness on local ϕ is shown in the bottom insets of figures 4.21(b)

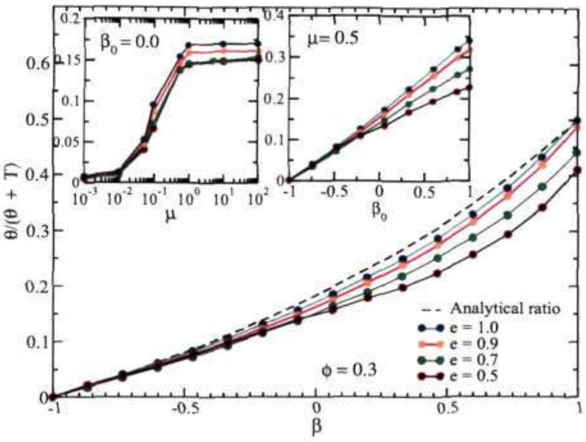

Figure 4.20: Main panel shows the effect of β on temperature ratio, $\theta/(\theta+T)$, for different values of e with $\phi = 0.3$. Black dashed line indicates theoretical temperature ratio based on 'constant β-model'. For 'variable β-model', the variation of temperature ratio over critical roughness β_0 for $\mu = 0.5$ is shown in the right inset, and in the left inset, the effect of friction coefficient, μ, on temperature ratio is shown for $\beta_0 = 0$.

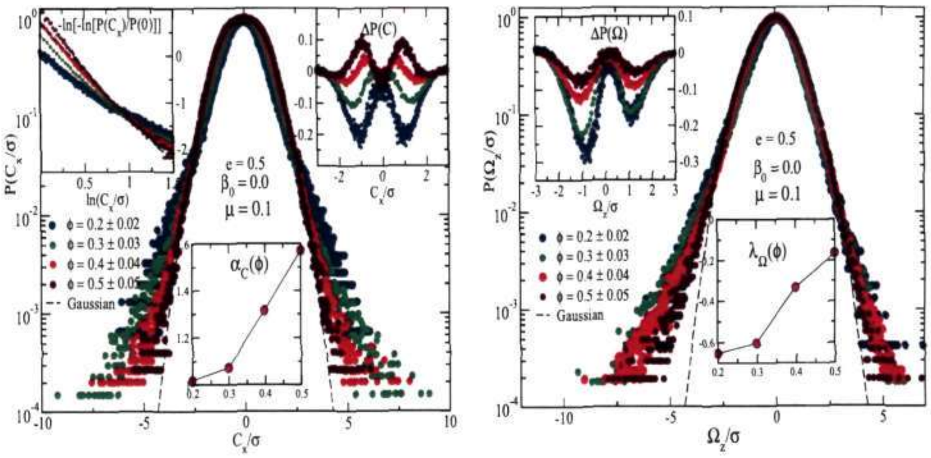

Figure 4.21: Local velocity distribution function for (a) translational and (b) rotational velocity, with varying local cell-density for $\phi = 0.3$, $e = 0.5$, $\beta_0 = 0$ and $\mu = 0.1$.

and 4.22(b). This asymmetry becomes more pronounced as we move towards the low dense regions of the domain. From the upper left insets of figures 4.21(b) and 4.22(b), we find that the low velocities of $P(\Omega_z)$ are also asymmetric as in the constant-β model.

In figure 4.23, the effect of e on the local VDFs of C_x and Ω_z are shown for

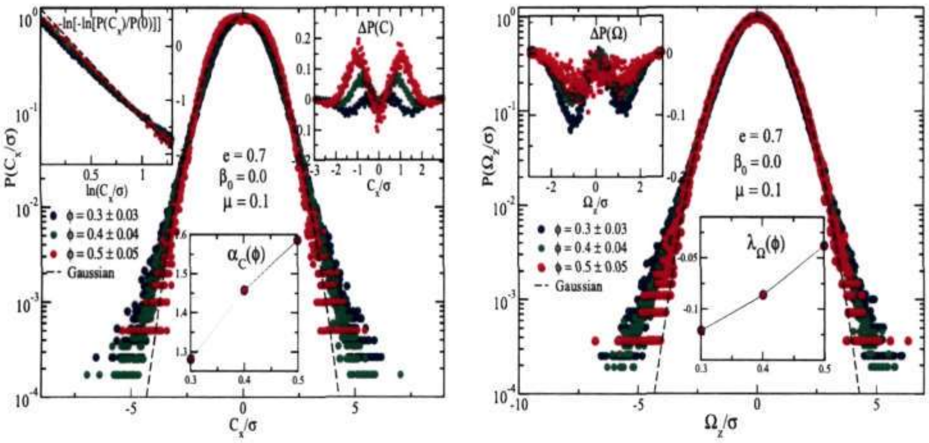

(a) (b)

Figure 4.22: Same as figure 4.21 but for $e = 0.7$.

cells where the "local" volume fraction is same as the system average density i.e. $\phi = 0.3$ with 10% tolerence. A transition is observed for the tails of $P(C_x)$ from an stretched exponential to an under-populated Gaussian distribution (see lower inset of figure 4.23(a)). For $P(\Omega_z)$ in figure 4.23(b), the asymmetry of tails increases for higher dissipative system. For elastic system, $e = 1$, $P(\Omega_z)$ agrees with a Gaussian.

Similar results are obtained by increasing the value of friction coefficient $\mu = 10.0$

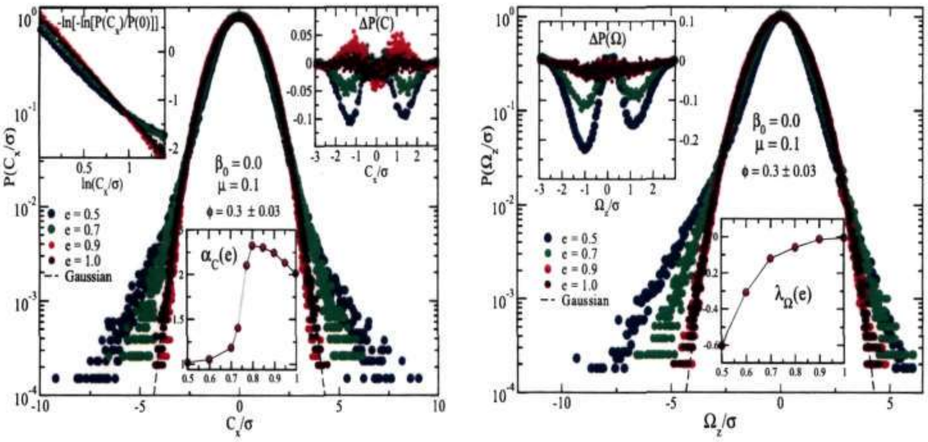

(a) (b)

Figure 4.23: Effect of e on local velocity distribution for $\beta_0 = 0$, $\mu = 0.1$ and $\phi = 0.3 \pm 0.03$ for (a) translational and (b) rotational velocity.

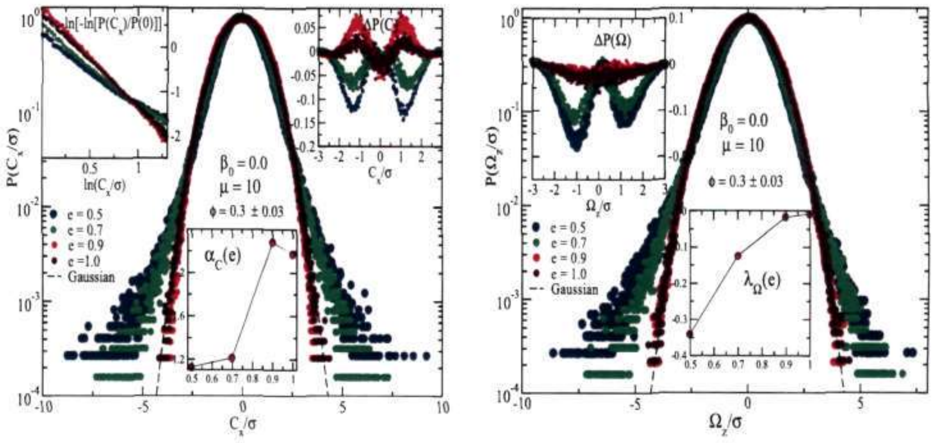

(a) (b)

Figure 4.24: Same as figure 4.23 but for $\mu = 10$.

as shown in figure 4.24; other parameters are as in figure 4.23.

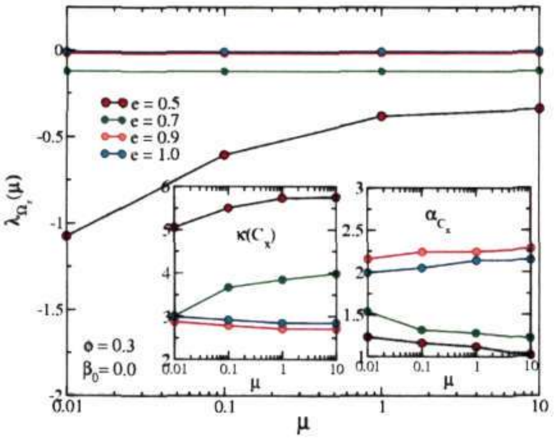

Figure 4.25: Variation of skewness for spanwise rotational velocity distribution on friction coefficient, μ, for different values of e (main panel). Left and right inset show the effect of μ on $\kappa(C_x)$ and α_C, respectively.

The effect of friction coefficient on local VDFs is summarized in figure 4.25 for $\phi = 0.3$ and $\beta_0 = 0$. The main panel shows the variation of skewness, λ_Ω, for spanwise rotational velocity on friction coefficient for different values of e. The left and right insets of figure 4.25 show the effect of μ on kurtosis and exponent of $P(C_x)$. From this figure it is clear that the effect of μ becomes more pronounced for dissipative system ($e = 0.5$); the skewness of $P(\Omega_z)$ decreases with increasing μ for $e = 0.5$. This can be explained from the energy transfer point of view. At higher value of friction coefficient, the energy transfer rate from translational to rotational motion increases. $P(C_x)$ deviates more from a Gaussian at higher collisional dissipation level, with the increase of μ. In the insets of figure 4.25, the variations of $\kappa(C_x)$ and α_C on μ supports the above idea.

4.3 Effect of Density on Orientational Correlation

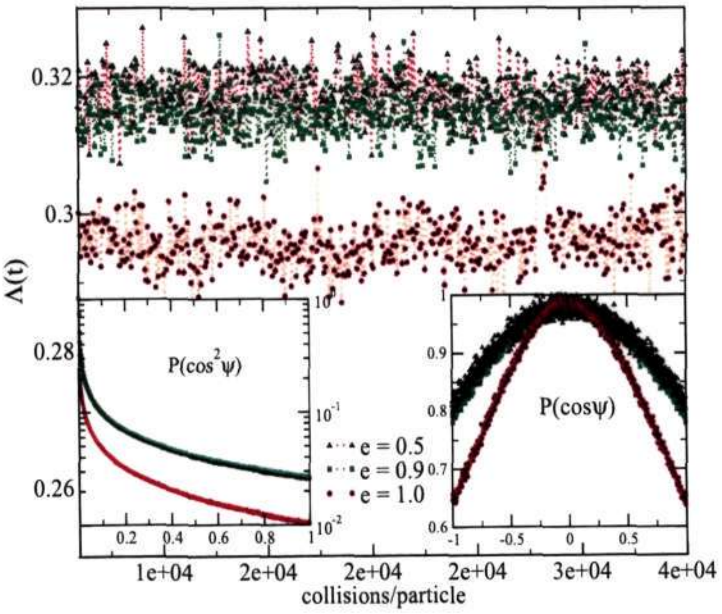

Figure 4.26: Temporal evolution of $\Lambda(t)$ at steady-state for $\beta = 0$ for three different values of e for a moderately dense system, $\phi = 0.3$. The left inset and right insets show the probability distribution of $cos\Psi$ and $cos^2\Psi$ respectively.

In main panel of figure 4.26 the temporal evolution of $\Lambda(t) = cos^2\Psi$ (see eqn 3.6 in chapter 3) for different values of normal restitution coefficient(e) is shown, with the tangential restitution coefficient being set to $\beta = 0$. Recall that Ψ is the average angle between the fluctuating translational ($\mathbf{C_i} = \mathbf{c_i} - \langle \mathbf{c_i} \rangle$) and rotational velocities ($\mathbf{\Omega_i} = \omega_i - \langle \omega_i \rangle$). The corresponding probability distributions of $cos^2\Psi$ and $cos\Psi$ are shown in left and right insets, respectively. $P(cos\Psi)$ is symmetric about the zero mean for all e, but its width becomes narrower with decreasing e.

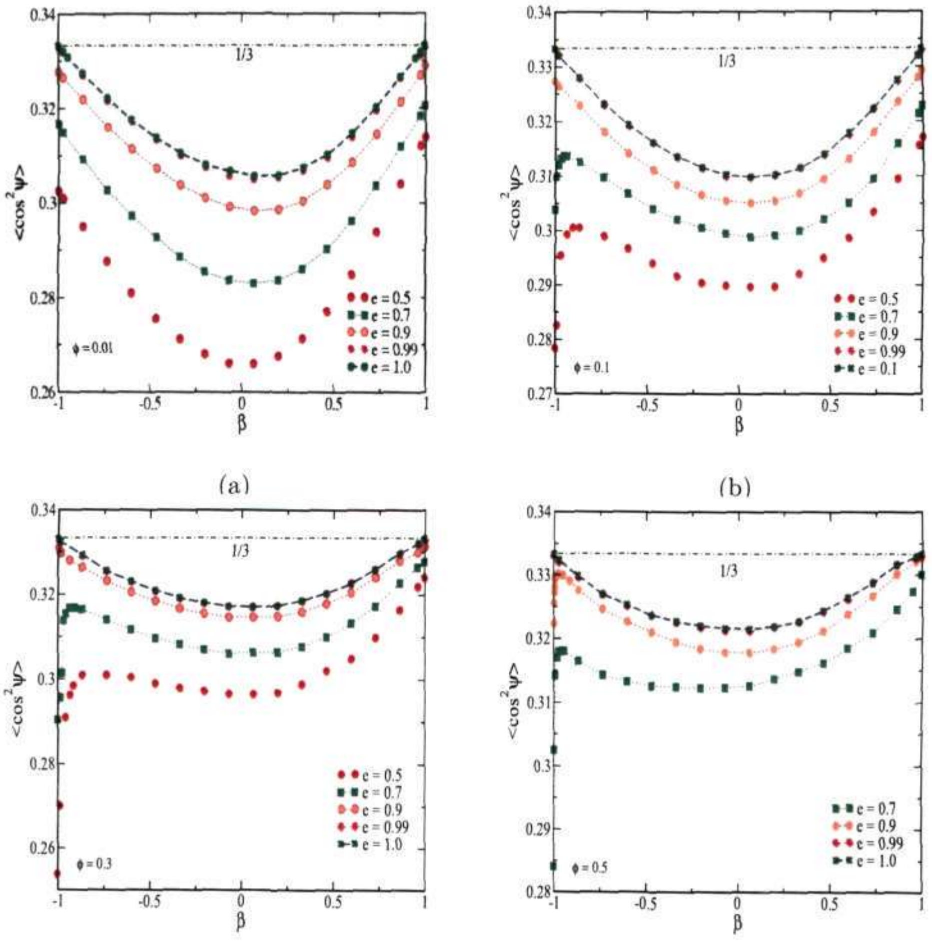

(a) (b)

(c) (d)

Figure 4.27: Effects of normal and tangential restitution coefficients on orientational correlation for granular system having volume fraction (a) 0.01, (b) 0.1, (c) 0.3 and (d) 0.5. Bold black dashed line indicates 1/3.

From the main panel and left inset, we find that even for perfectly elastic collisions ($e = 1$) the mean value of $\Lambda(t)$ deviates from 1/3 (for a molecular gas), signaling the presence of *orientational* correlation.

Figure 4.27 shows the dependence of $\langle\Lambda(t)\rangle$ on both restitution coefficients and volume fraction. In dilute limit, $\phi = 0.01$, for any value of normal restitution coefficient, the correlation increases from $\beta = -1$; the maximum correlation occurs for $\beta \sim 0.0$ where dissipation is maximum and for $\beta > 0.0$ the correlation starts

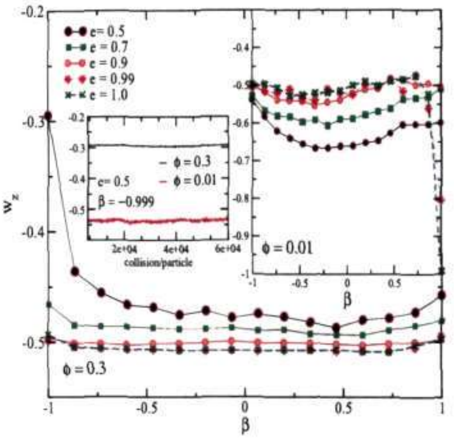

Figure 4.28: Effect of particle roughness on spanwise rotational velocity for moderately dense (main panel) and dilute system (right inset). Left inset shows the temporal evolution of ω_z at steady-state for dilute and dense system in smooth limit $\beta = -0.999$.

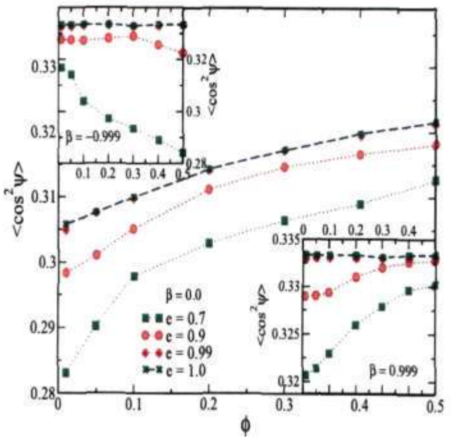

Figure 4.29: Effect of density on orientational correlation in main panel for different e with $\beta = 0$. The left and right insets show the same as in the main panel but for $\beta = -0.999$ and 0.999, respectively.

weakening upto the perfectly rough limit $\beta \to 1.0$. With the increase of system volume fraction, the translational motion of particles is more constrained towards the direction of shear-force and the rotational velocities shift their direction towards perpendicular to shear plane. This gives a lower correlation between two motions. On the contrary, at $\beta \sim -1$, with increasing system volume fraction $\langle \Lambda \rangle$ deviates more from $1/3$ with higher dissipation in collision. This strong correlation occurs in the smooth limit for inelastic particles due to the one-way energy transfer

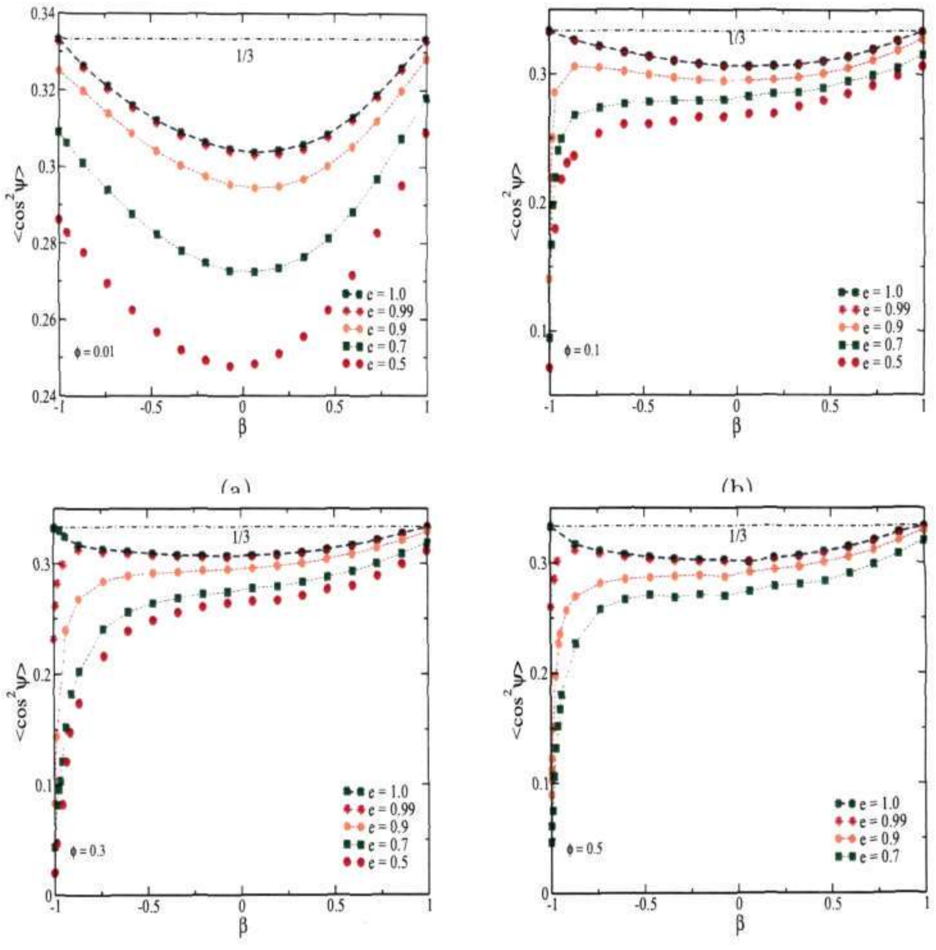

(a) (b)

(c) (d)

Figure 4.30: Orientational correlation based on instantaneous particle velocities, with parameters as in figure 4.27.

from translational to rotational mode, with translational velocities being the only source of momentum transfer during the collision process.

In figure 4.28, the main panel shows the variation of spanwise rotational velocity on particle roughness β for $\phi = 0.3$ for different values of e, and the top right inset shows the same as in the main panel but for a dilute system ($\phi = 0.01$). It is clear from this figure that for perfectly smooth limit $\beta \sim -1$ and at higher dissipation, the magnitude of the rotational velocity is lesser than its theoretical value (i.e. half of the shear-rate), as compared to the dilute limit. This supports the above fact of insufficient energy transfer from the translational to the rotational mode in a dense system at $\beta \sim -1$. At the other limit ($\beta = 1$),the orientational correlation weakens even for inelastic particles if we move towards the dense system.

The effect of system volume fraction and restitution coefficients on orientational correlation are summarised in figure 4.29. In the smooth limit, the inefficient exchange of energy process is more dominant than density effect and this leads to a high correlation between two motions. In other limits $\beta \sim 0$ and $\beta \rightarrow 1$, the density effect dominates.

Lastly, the orientational correlation is calculated based on instantaneous particle velocities $\mathbf{c_i}$ and ω_i. The dependence of volume fraction and two restitution coefficients on this correlation is shown in figure 4.30; the parameter values are as in figure 4.27. It is seen that the instantaneous particle velocities are more correlated in all respects than the correlation between the fluctuating velocities.

Chapter 5

RHEOLOGY OF FRICTIONAL GRANULAR SHEAR FLOW

This chapter is devoted to study the rheological properties of an unbounded sheared granular fluid. Parallelly we will go for test and validation of the available constitutive models (Lun (1991)) against the rhehological data obtained from our simulation. The effects of particle roughness and Coulomb friction on transport coefficient are elucidated in detail.

5.1 Equations of motion and constitutive model

In this section we briefly recall the equations of motion and constitutive model of a rough granular fluid which was originally derived by Lun (1991). Note that this constitutive model of Lun is based on the constant$-\beta$ model and does not incorporate Coulomb friction. Next we consider the uniform shear flow for which the mean field quantities and the expressions for various transport coefficients are explicitly written down.

5.1.1 Nondimensional Equations of Motion

We have non-dimensionalized all quantities via the following scaling:

$$\begin{aligned}
\mathbf{x}^* &= \frac{\mathbf{x}}{d}, \quad t^* = \dot{\gamma} t, \quad \mathbf{u}^* = \frac{\mathbf{u}}{d\dot{\gamma}}, \quad \mathbf{\Omega}^* = \frac{\mathbf{\Omega}}{\dot{\gamma}} \\
T^* &= \frac{T}{d^2\dot{\gamma}^2} \quad , \theta^* = \frac{\theta}{d^2\dot{\gamma}^2} \quad , \mathbf{\Psi}^* = \frac{\mathbf{\Psi}}{\rho_p d^2 \dot{\gamma}^2}, \quad \mathbf{P}^* = \frac{\mathbf{P}}{\rho_p d^2 \dot{\gamma}^2}, \quad \mathbf{L}^* = \frac{\mathbf{L}}{\rho_p d \dot{\gamma}^2} \\
(\mathbf{q}^*, \mathbf{q}_r^*) &= \frac{1}{\rho_p d^3 \dot{\gamma}^3}(\mathbf{q}, \mathbf{q}_r), \quad (\mathcal{D}^*, \mathcal{D}_r^*) = \frac{1}{\rho_p d^2 \dot{\gamma}^3}(\mathcal{D}, \mathcal{D}_r)
\end{aligned}$$

where d is the particle diameter, $\dot{\gamma}$ is the shear rate and ρ_p is the material density of particles. Here onwards, for convenience, we will omit the starred-superscript to denote nondimensional quantities. The resulting non-dimensional equations take the following form (Gayen & Alam 2006):

$$
\begin{aligned}
\frac{\partial\phi}{\partial t} &= -\nabla\cdot(\phi\mathbf{u}) && (5.1)\\
\phi\frac{\mathrm{D}\mathbf{u}}{\mathrm{D}t} &= -\nabla\cdot\mathbf{P}+\phi\mathbf{g} && (5.2)\\
\frac{K}{4}\phi\frac{\mathrm{D}\Omega}{\mathrm{D}t} &= -\nabla\cdot\mathbf{L}+\Psi && (5.3)\\
\frac{3}{2}\phi\frac{\mathrm{D}T}{\mathrm{D}t} &= -\nabla\cdot\mathbf{q}-\mathbf{P}{:}\nabla\mathbf{u}-\mathcal{D} && (5.4)\\
\frac{3}{2}\phi\frac{\mathrm{D}\theta}{\mathrm{D}t} &= -\nabla\cdot\mathbf{q}_r-\mathbf{L}{:}\nabla\boldsymbol{\Omega}-\mathcal{D}_r-\Omega\cdot\Psi && (5.5)
\end{aligned}
$$

The nondimensional forms of the stress tensor, the angular momemtum source, the translational and rotational heat fluxes are given by (Lun 1991; Gayen & Alam 2006):

$$
\begin{aligned}
\mathbf{P} &= [p-\xi(\nabla\cdot\mathbf{u})]\,\mathbf{1}-2\mu_s\mathbf{S}-\mu_r\mathbf{1}\times(2\Omega-\nabla\times\mathbf{u}) && (5.6)\\
\Psi &= -2\mu_r(2\Omega-\nabla\times\mathbf{u}) && (5.7)\\
\mathbf{q} &= -\kappa\nabla T-\kappa_h\nabla\theta && (5.8)\\
\mathbf{q}_r &= -\kappa_r\nabla T-\kappa_{rh}\nabla\theta, && (5.9)
\end{aligned}
$$

where $\mathbf{S}$ is the non-dimensional strain-rate deviator

$$
\mathbf{S}=\frac{1}{2}\left(\nabla\mathbf{u}+(\nabla\mathbf{u})^T\right)-\frac{1}{3}\left(\nabla\cdot\mathbf{u}\right). \qquad (5.10)
$$

The associated nondimensional transport coefficients have the following forms:

$$
\begin{array}{rclrcl}
p(\phi,T) &=& Tf_1(\phi), & \mu_s(\phi,T,\theta) &=& \sqrt{T}f_2(\phi,\theta/T)\\
\mu_r(\phi,T) &=& \sqrt{T}f_{2r}(\phi) & \xi(\phi,T) &=& \sqrt{T}f_3(\phi)\\
\kappa(\phi,T,\theta) &=& \sqrt{T}f_4(\phi,\theta/T) & \kappa_h(\phi,T,\theta) &=& \sqrt{T}f_{4h}(\phi,\theta/T)\\
\kappa_r(\phi,T,\theta) &=& \sqrt{T}f_{4r}(\phi,\theta/T) & \kappa_{rh}(\phi,T,\theta) &=& \sqrt{T}f_{4rh}(\phi,\theta/T)\\
\mathcal{D}(\phi,T,\theta) &=& T^{3/2}f_5(\phi,\theta/T) & \mathcal{D}_r(\phi,T,\theta) &=& -\,T^{3/2}f_{5r}(\phi,\theta/T),
\end{array}
$$

where p is the pressure, μ_s the shear viscosity, μ_r the rotational viscosity, ζ the bulk viscosity, κ_i's can be identified with various-types of thermal conductivity

(Lun 1991); $\mathcal{D}(\phi, T, \theta)$ and $\mathcal{D}_r(\phi, T, \theta)$ are the translational and rotational dissipations, respectively. In all above expressions, $f_i(\phi, \theta/T)$'s are the non-dimensional functions of density and temperature, related to different transport coefficients whose explicit forms can be found in Gayen & Alam (2006).

5.1.2 Steady Uniform Shear Flow

Here we consider the steady $(\partial/\partial t(\cdot) =)$, fully developed $(\partial/\partial x(\cdot) = 0)$ planer shear flow of rough, inelastic spheres, having no variation in the spanwise direction. For this case, the mass balance equation, the x- and z-components of the linear momentum equations and the x- and y-components of the angular momentum equations are identically satisfied. The only non-zero velocity field is the streamwise velocity which varies linearly with y, with constant density and granular energies throughout the flow-field. Thus, the base-state hydrodynamic-fields are given by

$$\left.\begin{array}{rcl} \phi & = & \text{constant} \\ \mathbf{u} & \equiv & (u_x, u_y, u_z)^T \;=\; (\dot{\gamma} y, 0, 0)^T \\ \Omega & = & (\omega_x, \omega_y, \omega_z)^T \;=\; (0, 0, -\dot{\gamma}/2)^T \\ T & \equiv & T(\phi, e, \beta) \;=\; \text{constant} \\ \theta & \equiv & \theta(\phi, e, \beta) \;=\; \text{constant} \end{array}\right\}, \tag{5.11}$$

where $\dot{\gamma}$ is the non-dimensional shear rate.

The base-state spin-velocity field, Ω, is obtained from the balance equation for angular momentum:

$$\begin{array}{rcl} \Psi & = & 0 \;=\; (2\Omega - \nabla \times \mathbf{u}) \\ \Rightarrow \;\Omega & = & \dfrac{1}{2}(0, 0, -\dot{\gamma})^T \;=\; (\omega_x, \omega_y, \omega_z)^T. \end{array} \tag{5.12}$$

Thus, the mean spin velocity in USF is equal to the rate of rotational bulk deformation. This, together with the balance equation of rotational granular energy, yields:

$$\begin{array}{rcl} \mathcal{D}_r & = & 0 \;=\; -T^{3/2} f_{5r} \\ \Rightarrow \;\dfrac{\theta}{T} & = & \dfrac{\eta_2}{(1 - \eta_2/K)}. \end{array} \tag{5.13}$$

If the translational and the rotational granular energies are equally partitioned (i.e. $T = \theta$), then it can be easily verified that

$$\beta \equiv 1,$$

which corresponds to perfectly rough particles. The other extreme of perfectly smooth particles ($\beta = -1$) yields $\theta = 0$, i.e. all the energies are contained in translational degrees of freedom. Thus, under general conditions, the *equipartition* principle does not hold for a granular system; this happens due to the transfer of momentum between the translational and the rotational degrees of motion.

The explicit expression for T is obtained by equating the production term due to the shear-work with the dissipation term in the balance equation for the translational kinetic energy:

$$\begin{aligned}
-\mathbf{P}{:}\nabla\mathbf{u} &= \mathcal{D} \\
\Rightarrow -P_{xy}\frac{\mathrm{d}u_x}{\mathrm{d}y} &= \mathcal{D} \\
\Rightarrow \mu_s\left(\frac{\mathrm{d}u_x}{\mathrm{d}y}\right)^2 &= \mathcal{D} = \mu_s \qquad (\text{since } \frac{\mathrm{d}u_x}{\mathrm{d}y} = 1) \\
\Rightarrow T &= \dot{\gamma}^2\frac{f_2(\phi,\theta/T;e,\beta,K)}{f_5(\phi,\theta/T;e,\beta,K)} \qquad (5.14)
\end{aligned}$$

By specifying the values for the particle volume fraction (ϕ) and the two restitution coefficients (e and β), we can calculate all transport coefficients (pressure, viscosity, thermal conductivity, etc.). These theoretical predictions on pressure and shear viscosity will be compared with our simulation results in the following section.

5.2 Stress Tensor: Pressure, Viscosity and Normal Stresses

The macroscopic stress, as measured in discrete particle simulations , is a byproduct of the particle-level mechanisms of momentum transfer. As in the hard-core model of dense gases, the stress is sum of its kinetic and collisional components. The former arises from the transport of momentum as the particles move through the system carrying their momentum, while the latter is due to direct interparticle collisions.

The non-dimensional total stress is calculated from (Alam & Luding (2003),2005)

$$\begin{aligned} \mathbf{P} &= \mathbf{P^k} + \mathbf{P^c}, \\ &= \frac{\pi}{6}\left[\sum_{i=1}^{N} \mathbf{C_i} \otimes \mathbf{C_i} + \frac{\mathbf{d}}{\tau_\mathrm{d}} \sum_{\textbf{collisions}} (\mathbf{J_{ij}} \otimes \mathbf{k})\right] \end{aligned} \tag{5.15}$$

where $\mathbf{P^k}$ and $\mathbf{P^c}$ are the kinetic and collisional contributions to the total stress $\mathbf{P}$, respectively, and $\mathbf{J_{ij}}$ is the collisional impulse. For the collisional stress, the sum is taken over all collisions during the averaging time window τ_d. Note that the trace of the kinetic part of the stress tensor is used to calculate the granular energy.

Now we decompose the total stress, defined in the compressive sense, in the following way:

$$\mathbf{P} = \mathbf{P^k} + \mathbf{P^c} = \mathbf{p1} + \mathbf{\Pi}, \tag{5.16}$$

where p is the pressure, Π the pressure deviator and $\mathbf{1}$ the unit tensor. From the off-diagonal components of the pressure deviator, we can calculate the shear viscosity which relates the shear stress to the rate of strain (Alam & Luding (2003)):

$$\begin{aligned} \Pi_{xy} &= -\mu_s \frac{du}{dy}, \\ \Rightarrow \mu_s &= = |\Pi_{xy}|. \end{aligned} \tag{5.17}$$

The diagonal components of the pressure deviator, could be different from zero, giving rise to normal stress differences (Alam & Luding (2003),2005);

$$\begin{aligned} \mathcal{N}_1 &= \frac{\Pi_{xx} - \Pi_{yy}}{p}, \\ \mathcal{N}_2 &= \frac{\Pi_{yy} - \Pi_{zz}}{p}. \end{aligned} \tag{5.18}$$

The former is called the first normal stress difference, and the latter the second stress difference. Note that we have scaled these quantities by pressure. For a Newtonian fluid, $\mathcal{N}_1 = 0$ and $\mathcal{N}_2 = 0$. Hence the non-zero values of $\mathcal{N}_1$ and $\mathcal{N}_2$ are indicators of the non-Newtonian character of the fluid.

From our simulation of unbounded granular shear flow, we will calculate pressure, shear viscosity and two normal stress differences. For all simulations in this chapter, we have considered a small system with 1000 particles so that we can eliminate the effects of dissipation-induced inhomogeneities and the system remains homogeneous. The homogeneity of the uniform shear flow alllows us to calculate the stress by averaging it over the whole computational box (Campbell (1990), Alam & Luding (2002), Alam & Luding (2003a)).

5.3 Results

5.3.1 Pressure and Shear Viscosity

Figure 5.1 shows the variations of pressure and shear viscosity with particle volume fraction for different values of e for perfectly smooth particles by setting $\beta = -1$. Figure 5.1(a) shows that for any value of normal restitution coefficient, pressure initially decreases with volume fraction and after reaching a minimum value at $\phi \sim 0.15$, it starts increasing. The reason behind this non-monotonicity is that the total stress is a combination of a collisional and a kinetic part (see eqn.5.15) . In dilute regime the collisional contribution is negligible and the kinetic contribution dominates. In dense limit, the collisional contribution dominates and the kinetic contribution is negligible. So, at two extreme values of volume fraction, one expects higher values of stress. The solid lines in the figure 5.1 indicates the theoretical prediction of the results taken from eqn. Lun' model. For elastic limit, $e \sim 1$, both simulation and theoretical results fairly agree with each other (except for higher volume fraction). The value of pressure decreases with decreasing e. Similar trends for viscosity are observed in figure 5.1(b) with particle volume fraction and normal restitution coefficient. The particle volume fraction has a large effect on viscosity.

The effect of surface roughness (β) on pressure and viscosity is studied in figures 5.2(a) and (b) for $\beta = 0.0$. For any value of normal restitution coefficient, both pressure and viscosity decrease for $\beta = 0$ as compared to perfectly smooth case ($\beta = -1$). The deviations from theoretical values are pronounced even for elastic particles ($e = 1.0$) with $\beta = 0$. This is tied to the assumptions in the constitutive model of Lun (1991) which is valid for $|\beta| \sim 1$. The simulation results in figure 5.3 agree well with theoretical predictions.

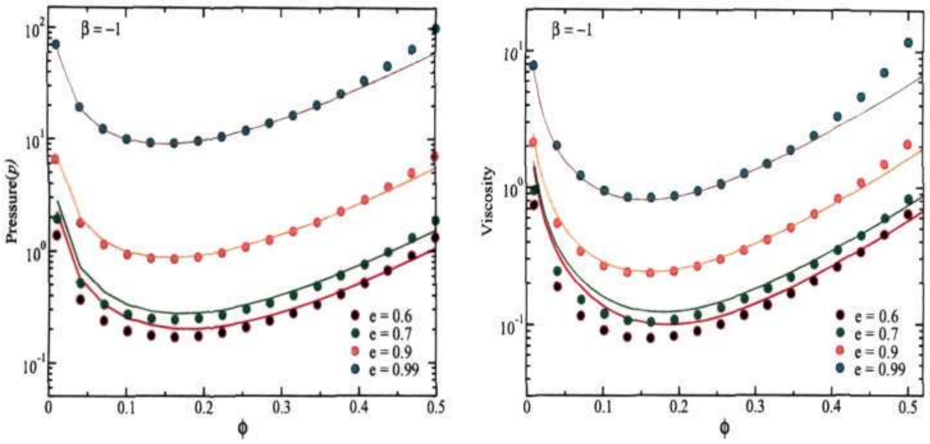

(a) (b)

Figure 5.1: Variation of (a) pressure and (b) viscosity with volume fraction, ϕ, for smooth particles $\beta = -1$. Continuous lines represent the theoretical prediction of Lun's model (1991).

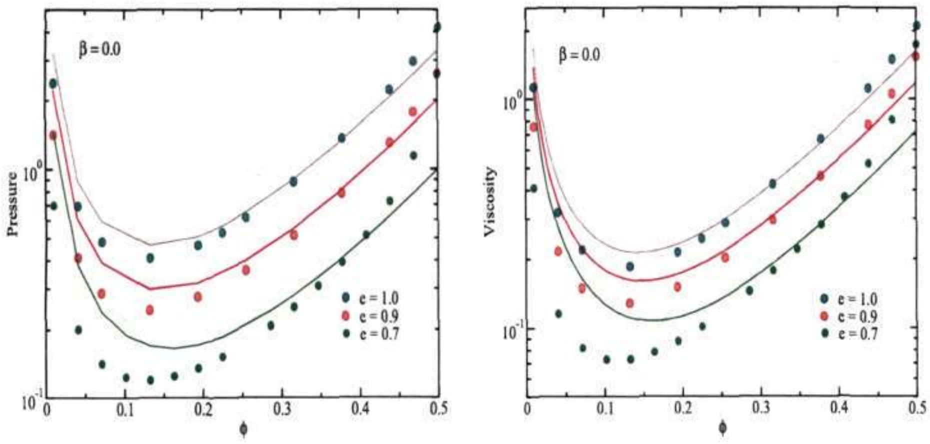

(a) (b)

Figure 5.2: Same as in figure 5.1, but for $\beta = 0$.

The effect of Coulomb friction on the pressure and viscosity is shown for the coefficient of friction $\mu = 0.1$ and 10 as in figures 5.4 and 5.5, respectively. It is observed that at lower values of Coulomb friction, the simulation results for pressure and viscosity deviate more from the theoretical model based on the constant-β model, as compared to higher values of μ.

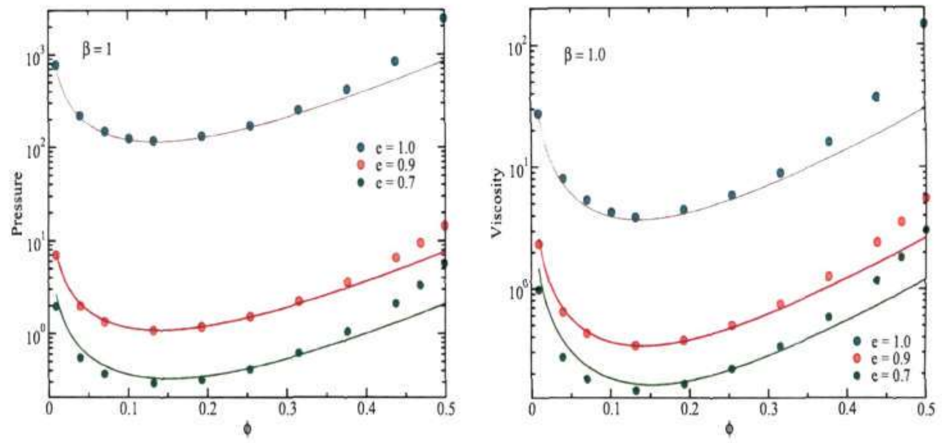

(a) (b)

Figure 5.3: Same as in figure 5.1, but for $\beta = 1$.

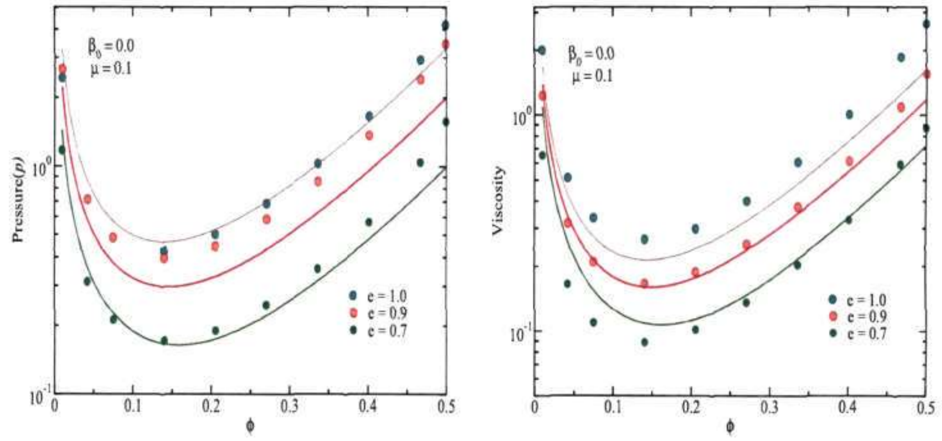

(a) (b)

Figure 5.4: Variation of (a) pressure and (b) viscosity with the volume fraction, ϕ for critical roughness $\beta_0 = 0$ with $\mu = 0.1$.

5.3.2 Normal Stress Difference

Figure 5.6 shows the variation of two normal stress differences ($\mathcal{N}_1$ and $\mathcal{N}_2$) with particle volume fraction for a normal restitution coefficient $e = 0.9$. In the right inset, the effect of volume faction on $\mathcal{N}_1$ is plotted for different values of normal restitution coefficients. The first normal stress difference $\mathcal{N}_1$ is always positive and has a maximum value at Boltzmann limit. It then decreases with volume fraction.

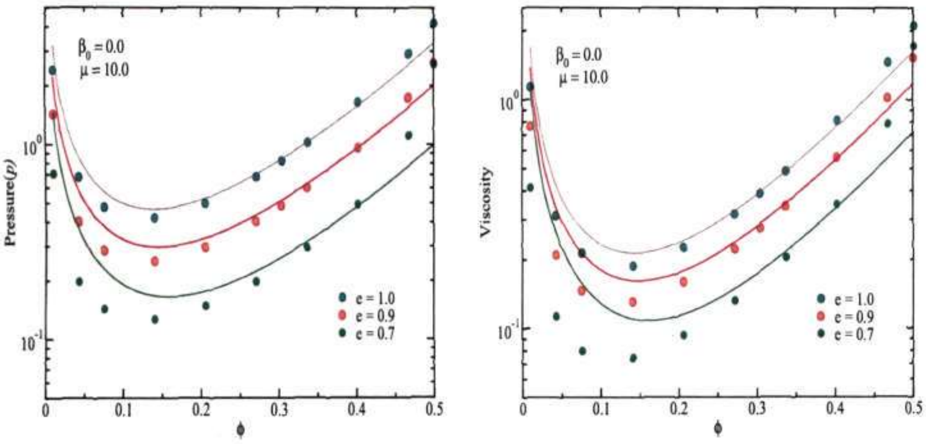

(a) (b)

Figure 5.5: Same as in figure 5.4 but for $\mu = 10.0$

A "sign-reversal" of $\mathcal{N}_1$ occurs at higher volume fraction (Alam & Luding (2003)). The value of $\mathcal{N}_1$ increases with increase in the collisional dissipation. It is noted that $\mathcal{N}_1$ changes its sign at $\phi \sim 0.468$ for $e = 0.99$; the sign reversal of $\mathcal{N}_1$ occurs at higher volume fractions for system with higher collisional dissipation. This sign reversal of $\mathcal{N}_1$ was noted by Alam & Luding (2003), and was subsequently tied to the microstructural reorganization of particles, leading to the formation of directed "force-chains".

Figure 5.6 shows that the second normal stress difference, $\mathcal{N}_2$, is negative in Boltzmann limit and changes its sign from negative to positive in dilute limit ($\phi \approx 0.130$); then it monotonically increases with increasing ϕ. At very low densities, the contribution of collisional components to the stress is less as compared to the kinetic counterpart. At moderate density, the collisional stress becomes important which dominates in the dense limit. Thus, the behaviour of $\mathcal{N}_1$ and $\mathcal{N}_2$ are dictated by kinetic and collisional stresses in the dilute and dense limits, respectively.

For perfectly smooth particles we can compare our results with the work of Sela & Goldhirsch (1998) who derived constitutive expressions for the stress tensor upto the Burnett-order for a dilute granular fluid ($\phi \to 0$). For uniform shear flow,

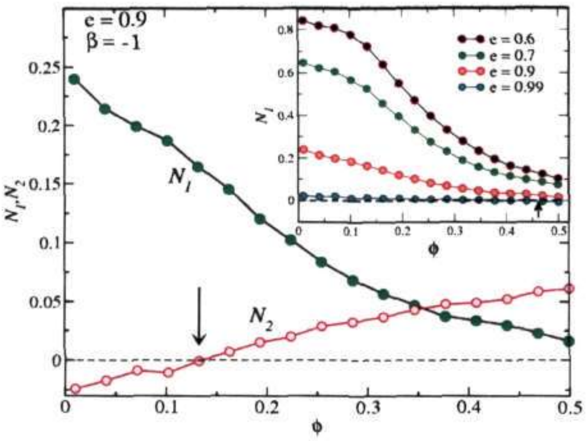

Figure 5.6: Constant-β model: In main panel the variations of $\mathcal{N}_1$ and $\mathcal{N}_2$ with solid volume fraction are shown for restitution coefficient $e = 0.9$ and $\beta = -1$. The arrow indicates the critical volume fraction where N_i changes sign. Right inset shows the variation of $\mathcal{N}_1$ with volume fraction for different values of e.

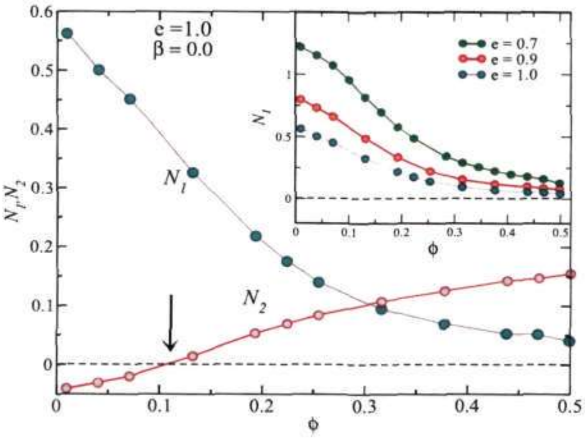

Figure 5.7: Same as figure 5.6 but for $e = 1$ and $\beta = 0$ with constant-β model.

it can be verified (Sela & Goldhirsch (1998); Alam & Luding (2005a)) that the expressions for normal stress differences take the following forms:

$$\mathcal{N}_1 = \frac{1.6735\epsilon - 0.04315\epsilon^2}{1.2996 + 0.0966\epsilon} \tag{5.19}$$

$$\mathcal{N}_2 = -\frac{0.14189\epsilon - 0.003659\epsilon^2}{1.2996 + 0.0966\epsilon} \tag{5.20}$$

where $\epsilon = (1 - e^2)$ is the degree of inelasticity. Clearly, for a given inelasticity

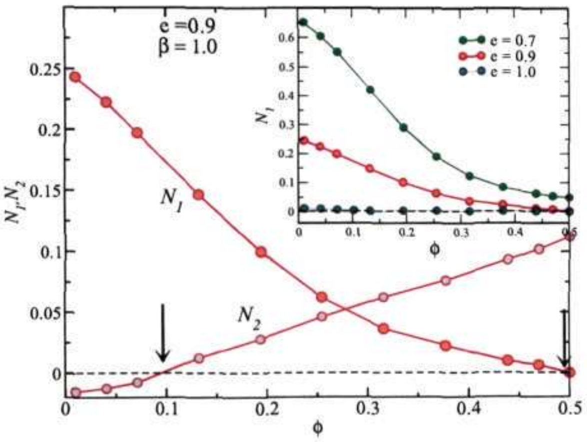

Figure 5.8: Same as figure 5.6 but for $e = 0.9$ and $\beta = 1$ with constant-β model.

$\epsilon \neq 0$, $\mathcal{N}_1 > 0$ and $\mathcal{N}_2 < 0$ in the Boltzmann limit. For example, for $e = 0.9$, the values of normal stress differences are $\mathcal{N}_1 \approx 0.24$ and $\mathcal{N}_2 \approx -0.0203$; the corresponding results from our simulation are $\mathcal{N}_1 \approx 0.2401$ and $\mathcal{N}_2 \approx -0.0240$ at a volume fraction of $\phi = 0.01$.

The same set of results on $\mathcal{N}_1$ and $\mathcal{N}_2$ are shown for $\beta = 0.0$ in figure 5.7. It is noted that even for elastic collisions $e = 1$, $\mathcal{N}_1$ does not undergo a sign-reversal even at $\phi = 0.52$. It is also observed that the value of $\mathcal{N}_1$ increases at $\beta = 0.0$ as compared to the perfectly smooth case, $\beta = -1$. The effect of Coulomb friction on

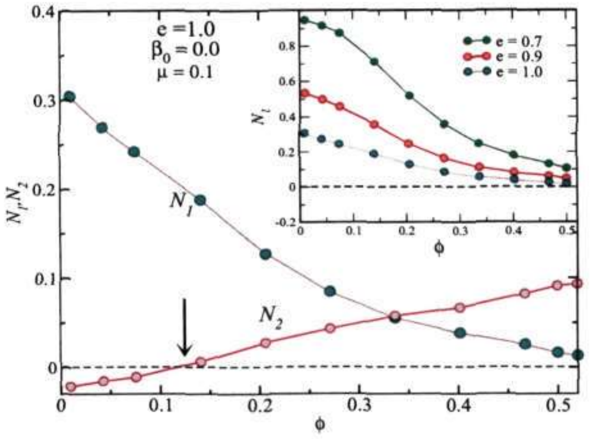

Figure 5.9: Variable-β model: In main panel the variation of $\mathcal{N}_1$ and $\mathcal{N}_2$ with solid volume fraction, for restitution coefficient $e = 1.0$ and $\mu = 0.1$. The arrow indicates the critical volume fraction where N_i changes sign. Right inset shows the variation of $\mathcal{N}_1$ with volume fraction for different values of e.

both the normal stress differences is depicted in figures 5.9 and 5.10 for $\mu = 0.1$ and $\mu = 10.0$, respectively. With increase of Coulomb friction, the magnitudes of both $\mathcal{N}_1$ and $\mathcal{N}_2$ increase. As a result, $\mathcal{N}_1$ changes its sign at a higher volume fraction for the system having a large value of friction coefficient μ.

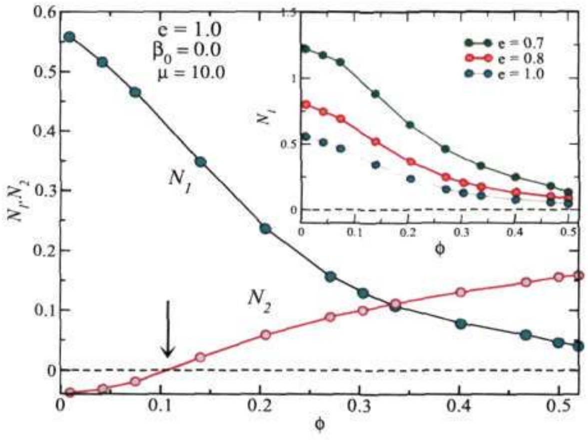

Figure 5.10: Same as figure 5.9 but with $\mu = 10.0$.

Chapter 6

SUMMARY

In the present thesis, an efficient event-driven molecular dynamics code has been developed which is based on the paper of Lubachevsky (1991) and the book by Rapaport (1995). The computational approach employed in this study mainly consists of initialization, book-keeping and diagnostic parts. This code is very fast and can handle a large number of particles ($N \sim 10^6$) and has been generalized to three dimensions (3D). It can be used to simulate various kind of plane granular flows (Couette flow, Poiseuille flow, Chute flow, etc.) with rough, frictional particles. For the simplest model of rough, inelastic spheres, two material parameters are needed to characterize the collision process: the normal coefficient of restitution, e, and the tangential coefficient of restitution, β. For a more realistic collision model of rough particles, we have taken into account the effect of Coulomb friction which helps to distinguish between the sliding and the rolling contacts, resulting in a contact-angle (γ) dependent tangential restitution coefficient $\beta(\gamma)$. This code has been tested and validated for both unbounded and bounded granular shear flows. For the latter case of bounded flow, the wall-particle interactions are modeled using the same collision dynamics of particle-particle interaction. For either case, the system is allowed to reach a 'non-equilibrium' steady-state condition by monitoring the temporal evolution of system's kinetic energy.

The rest of the thesis dealt with investigating various microscopic and macroscopic propreties of "unbounded" granular shear flow. We have studied various aspects of granular flow like the velocity distribution function (VDF), density and spatial velocity correlations, orientational correlation and rheology.

In the Boltzmann limit ($\phi = 0.01$), no dissipation-induced density inhomoheneity is observed in our system even for the most dissipative case (at $e = 0.5$ and $\beta = 0$) that we have studied. We have thoroughly examined the effects of particle roughness and rotation on the probability distributions of fluctuating translational and rotational velocities as well as density and spatial velocity correlations. The

VDFs of translational velocity (C_i) and rotational velocity (Ω_i) folllow an stretched-exponential distribution having the shape

$$P(x) \sim exp(-\gamma x^{\alpha}), \quad \text{with} x = C, \Omega, \tag{6.1}$$

where γ and α are the prefactor and exponent for the distribution, respectively. The deviations from a Gaussian, both at the tail and low velocity regions, have been found oberved for inelastic system. Even for an elastic system ($e = 1$), the deviation is pronounced for rough particles with $\beta = 0$; for two limiting cases of perfectly smooth ($\beta = -1$) and rough ($\beta = 1$) particles, the velocity distributions agree with a Gaussian. Strong spatial velocity correlations for streamwise translational velocity have been observed even for elastic system with $\beta = 0$. Unlike a molecular gas, the translational and rotational velocities of a granular gas are shown to be *directionally* correlated. This *orientaional* correlation is a smooth function of particle roughness for any level of collisional dissipation. It is maximum at $\beta \sim 0$ and monotonically decreases towards two extreme limits of $\beta = \pm 1$. Orientational and spatial velociy correlation are responsible for non-Gaussian distributions of translational and rotational velocities.

With increasing system density, the dissipation-induced density inhomogeneity is observed over the whole domain. A pronounced asymmetry about the mean value is observed for the probability distributions of local density, local shear rate and local spanwise rotational velocity. Therefore the calculation of "local" VDF is a proper way to study such inhomogeneous systems. For a moderately dense system ($\phi = 0.3$), an interesting phenomenon is observed for the local VDF of streamwise translational velocity: its tails undergo a transition from an stretched exponential to an under-populated Gaussian distribution with decreasing dissipation and finally to a Gaussian for no dissipation. The VDF of spanwise rotational velocity makes a transition from stretched exponential tails to a Gaussian with decreasing dissipation. For the dense system ($\phi = 0.5$) with dissipation, the VDF for streamwise translational velocity is a Gaussian with under-populated tails. The effect of Coulomb friction on VDFs has been studied for different values of friction coefficient μ for $\phi = 0.3$ with the critical roughness being set to $\beta_0 = 0$. With the incorporation of Coulomb friction, a pronounced asymmetry of the tails of the VDF of rotational velocities is seen and the skewness of the distribution increases with increasing dissipation.

Lastly, we have investigated the rheologoical properties of unbounded shear flow of rough, frictional particles. Our simulations results on pressure and shear viscosity compare well with the predictions of Lun's (1991) rheological model at small dissipations. The model predictions deteriorate with increasing dissipation which is tied to the inherent assumptions of the underlying model which is valid for quasi-elastic ($e \sim 1$) particles in the prefectly smooth and rough ($|\beta| \sim 1$) limits. Our results on normal stress differences ($\mathcal{N}_1$ and $\mathcal{N}_2$) suggest that a non-Newtonian constitutive model is required for moderately dissipative rough, frictional particles.

Appendix I

RESULTS FOR VOLUME FRACTION $\phi = 0.1$

Here we present some results on VDFs for a particle volume fraction of $\phi = 0.1$. These results are similar to those for $\phi = 0.3$ as disscussed in chapter 4.

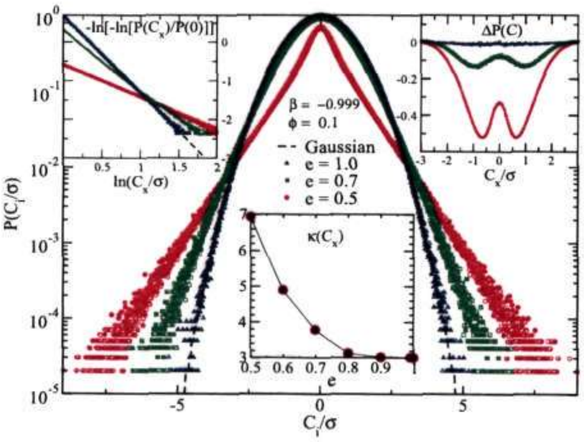

Figure I.1: Translational velocity distribution for $\phi = 0.1$ for $\beta = -0.999$

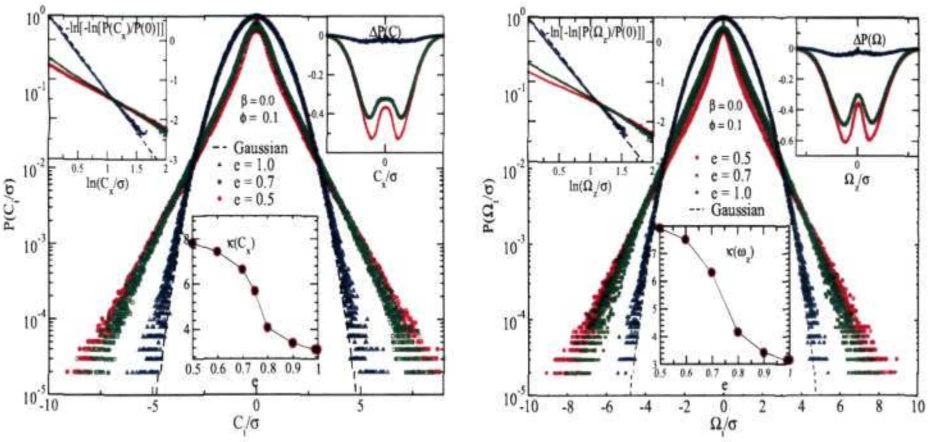

(a) (b)

Figure I.2: (a) Translational and (b) rotational velocity distributions for $\phi = 0.1$

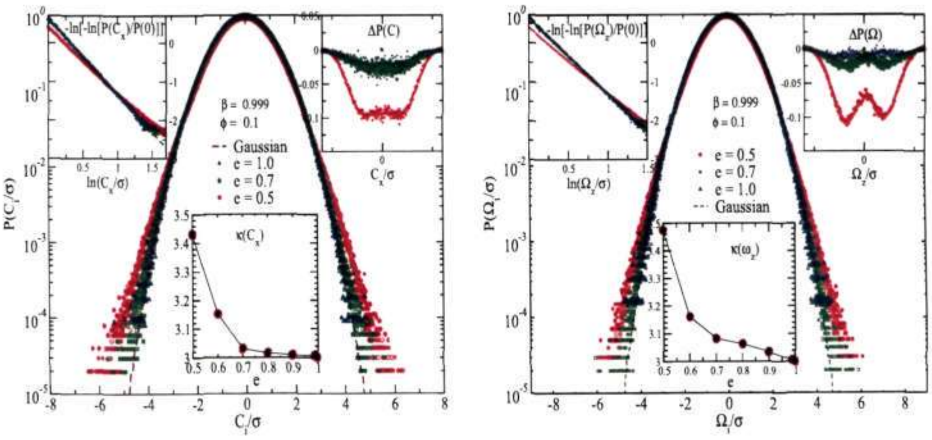

(a) (b)

Figure I.3: (a) Translational and (b) rotational velocity distributions for $\phi = 0.1$ and $\beta = 1.0$

Appendix II
DENSITY AND VELOCITY CORRELATIONS

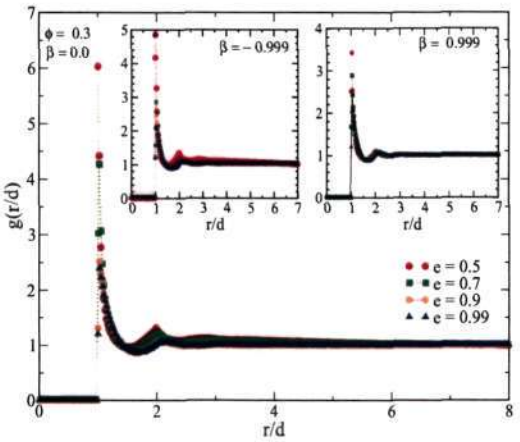

Figure II.1: Pair correlation function (main panel) for $\beta = 0$ and $\phi = 0.3$. Left and right insets show same as main panel but for $\beta = -0.999$ and 0.999, respectively

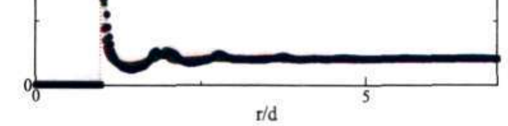

Figure II.2: Same as figure II.2 but for $\phi = 0.5$.

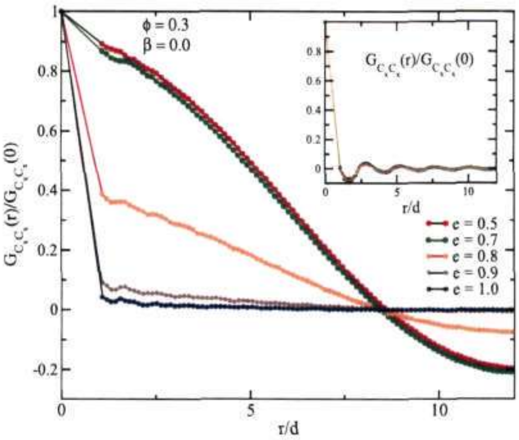

Figure II.3: Main panel shows the streamwise velocity correlation based binwise averaging method and inset for cellwise averaging method.

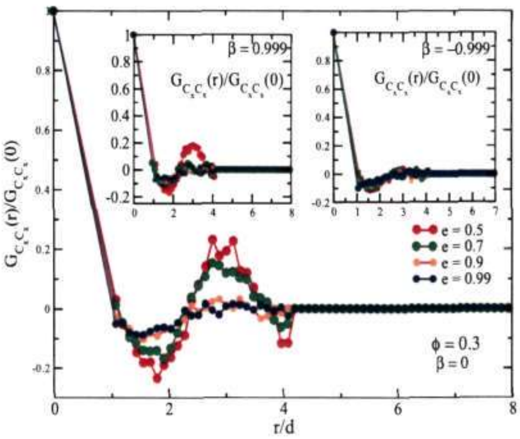

Figure II.4: Main panel shows the streamwise velocity correlation on the middle xz-plane for $\beta = 0$ and $\phi = 0.3$. Left and right inset show same as main panel but for $\beta = -0.999$ and $\beta = 0.999$, respectively. All are based on cellwise averaging.

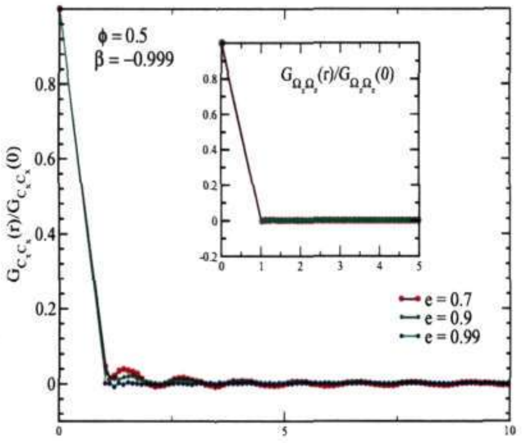

Figure II.5: Velocity correlation for streamwise translational (main panel) and spanwise rotational velocity (top inset) for $\beta = -0.999$ and $\phi = 0.5$. All are based on cellwise averaging.

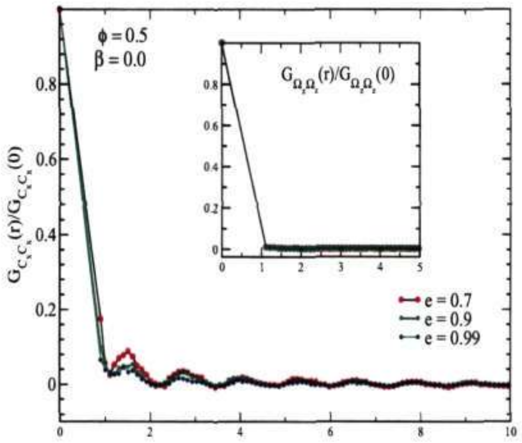

Figure II.6: Same as figure II.5 but for $\beta = 0.0$.

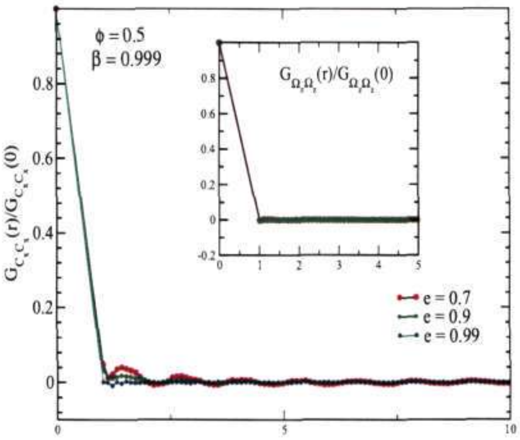

Figure II.7: Same as figure II.5 but for $\beta = 0.999$.

References

ALAM, M. 2006 Streamwise structures and density patterns in rapid granular couette flow: a linear stability analysis. *J. Fluid Mech* **553**, 1.

ALAM, M., ARAKERI, V. H., NOTT, P. R. & HERRMANN, H. J. 2005 Instability-induced ordering, universal unfolding and the role of gravity in granular couette flow.. *J. Fluid Mech.* **523**, 277.

ALAM, M. & LUDING, S. 2002 How good is the equipartition assumption for the transport properties of a granular mixture? *Granular Matter* **4**, 139.

ALAM, M. & LUDING, S. 2003 First normal stress difference and crystallization in a dense sheared granular fluid. *Phys of Fluids* **15**, 22982312.

ALAM, M. & LUDING, S. 2003a Rheology of bidisperse granular mixtures via event-driven simulations. *J. Fluid Mech.* **476**, 69.

ALAM, M. & LUDING, S. 2005 Energy nonequipartition, rheology and microstructure in sheared bidisperse granular mixtures.. *Physics of Fluids.* **17**, 1.

ALAM, M. & LUDING, S. 2005a Non-newtonian granular fluid: Simulation and theory. In *Powders and Grains* (ed. H. H. R. Garcia-Rojo & S. McNamara), p. 1141. Stuttgart, Deutschland: A. A. Balkema.

ALAM, M. & NOTT, P. R. 1997 Influence of friction on stability of unbounded granular couette flow. *J. Fluid Mech* **343**, 267.

ALAM, M., TRUJILLO, L. & HERRMANN, H. J. 2006 Hydrodynamic theory for reverse brazil nut segregation and the non-monotonic ascension dynamics. *Journal of Statistical Physics.* **124**, 587–623.

ALLEN, M. P. & TILDESLEY, D. J. 1987 *Computer Simulation of Liquids.* Oxford: Oxford University Press.

ARANSON, I. S. & TSIMRING, L. S. 2006 Patterens and collective behavior in granular media: Theoretical concepts. *Reviews of Mod. Phys.* **78**, 641.

BRILLIANTOV, N., PÖSCHEL, T., KRANZ, W. & ZIPPELIUS, A. 2007 Translations and rotations are correlated in granular gases. *Phy. Rev. Letter* **98**, 128001.

BURTALLY, N., KING, P. J. & SWIFT, M. R. 2002 Spontaneous air-driven separation in vertically vibrated fine granular mixtures. *Science.* **295**, 1877.

CAFIERO, R., LUDING, S. & HERRMANN, H. 2002 Rotationally driven gas of inelastic rough spheres. *Europhys. Lett.* **60**, 854.

CAFIERO, R., LUDING, S. & HERRMANNN, H. J. 2000 Two dimensional granular gas of inelastic sphere with multiplicative driving. *Phys. Rev. Lett* **84**, 6014.

CAMPBELL, C. S. 1990 Rapid granular flow. *Ann. Rev. Fluid Mechanics* **22**, 57.

CONDIFF, D. W. & DAHLER, J. S. 1964 Fluid mechanical aspects of antisymmetric stress. *Phys Fluids* **6**, 842.

CONWAY, S. L. & GLASSER, B. J. 2004 Density waves and coherent structures in granular couette flow. *Phys Fluids.* **16**, 509.

DAHLER, J. S. & THEODOSOPULU, M. 1974 Kinetic theory of dense polyatomic liquids. *Adv. Chem. Phys.* **30**, 155.i.

ESIPOV, S. & PÖSCHEL, T. 1997 The granular phase diagram. *J. Stat. Phys.* **86**, 1385.

FOERSTER, S. F., LOUGE, M. Y., CHANG, H. & ALLIA, K. 1994 Measurements of collision properties of small spheres. *J. Fluid Mech.* **258**, 335.

FORTERRE, Y. & POULIQUEN, O. 2002 Stability analysis of rapid granular chute flows: formation of longitudinal vortices. *J. Fluid Mech.* **467**, 361.

GARZO, V. & DUFTY, J. W. 1999 Dense fluid transport for inelastic hard spheres. *Phys. Review E.* **59**, 5895.

GAYEN, B. & ALAM, M. 2006 Algebraic and exponential instabilities in a sheared micropolar granular fluid. *J. Fluid Mech.* **567**, 195–233.

GOLDHIRSCH, I. 2003 Rapid granular flows. *Annu. Rev. Fluid Mech.* **35**, 267.

GOLDHIRSCH, I., NOSKOWICZ, S. H. & BAR-LEV, O. 2005 Nearly smooth granular gases. *Phys. Rev. Lett* **95**, 068002.

GOLDHIRSCH, I. & TAN, M. 1996 The single particle distribution function for rapid granular shear flows of smooth inelastic disks. *Phys. Fluid.* **8**, 1752.

GOLDHIRSCH, I. & ZANETTI, D. 1993 Clustering instability in dissipative gases. *Phys. Rev. Lett.* **70**, 1619.

GOLDSHTEIN, A. & SHAPIRO, M. 1995 Hydrodynamics of granular materials. *J. Fluid Mech* **282**, 75.

HAYAKAWA, H. 2001 Note on a micropolar gas-kinetic theory. In *In traffic and granular flows* (ed. M. Fukui, Y. Sugiyama, M. Schreckenberg & D. Wolf), pp. 485–490. Springer.

HERBST, O., CAFIRO, R., ZIPPELIUS, A., HERRMANN, H. J. & LUDING, S. 2005 A driven two-dimensional granular gas with coulomb friction. *Phys. Fluids.* **17**, 107102.

HERRMANN, H. J., HOVI, J. P. & LUDING, S. 1998 Physics of dry granular media. *Kluwer* .

HONG, D. C., QUINN, P. V. & LUDING, S. 2001 Reverse brazil nut problem: Competition between percolation and condensation. *Phys. Rev. Lett.* **86**, 3423–3426.

HOPKINS, M. A. & LOUGE, M. 1991 Inelastic micro-structure in rapid granular flows of smooth disks. *Phys. Fluids.* **3**, 47–57.

HUTHMANN, M. & ZIPPELIUS, A. 1997*a* Dynamics of inelastically colliding rough spheres:relaxation of translational and rotational energy. *Phys. Rev. E* **56**, R6275.

HUTHMANN, M. & ZIPPELIUS, A. 1997*b* Dynamics of inelastically colliding rough spheres:relaxation of translational and rotational energy. *Phys. Rev. E* **56**, R6275.

HUTTER, K. & RAJAGOPAL, K. R. 1994 On flows of granular materials. *Continuum Mech. Thermodyn* **6**, 81.

JAEGER, H. M., NAGEL, S. R. & BEHRINGER, R. 1996 Granular solids, liquids and gases. *Rev. Mod. Phys.* **68**, 1259.

JENKINS, J. T. & RICHMAN, M. W. 1985 Kinetic theory for plane flows of a dense gas of identical, rough, inelastic disks. *Phys Fluids* **28**, 3485.

JENKINS, J. T. & ZHANG, C. 2002 Kinetic theory for identical, frictional, nearly elastic spheres. *Physics of Fluids* **14** (3), 1228–1235.

KADANOFF, L. 1999 Built upon sand: theoretical ideas inspired by granular flows. *Rev. Mod. Phys* **71**, 435.

KANATANI, K. 1979 A micropolar continuum theory for the flow of granular materials. *Intl J. Engng Sci.* **17**, 419.

LEES, A. W. & EDWARDS, S. F. 1972 The computer study of transport processes under extreme conditions. *J. Phys. C* **5** (6), 1921.

LOSERT, W., COOPER, D., DELOUR, J., KUDROLI, A. & GOLLUB, J. 1999 Velocity statistics in excited granular media. *Chaos* **9**, 682.

LUBACHEVSKY, B. D. 1991 How to simulate billards and similar systems. *J. Comp. Phys.* **94** (2), 255.

LUDING, S., CAFIERO, R. & HERRMANN, H. 2003 Driven granular gases. In *In granular gas dynamics. Lectures notes in physics* (ed. T. Pöschel & N. Brilliantov), , vol. 624. Springer.

LUDING, S., HUTHMANN, M., MCNAMARA & ZIPPELIUS, A. 1998*a* Homogeneous cooing of rough dissipative particles: theory and simulations. *Phys. Rev. E* **58**, 3416.

LUDING, S., HUTHNANN, M., MACNAMARA, S. & ZIPPELIUS, A. 1998*b* Homogeneous cooling of rough, dissipative particles: theory and simulations. *Phys. Rev. E* **58**, 3416.

LUN, C. K. K. 1991 Kinetic theory for granular flow of dense, slightly inelastic, slightly rough spheres. *J. Fluid Mech.* **233**, 539–559.

LUN, C. K. K. & BENT, A. A. 1994 Numerical simulation of inelastic frictional spheres in simple shear flow. *J. Fluid Mech.* **258**, 335.

LUN, C. K. K. & SAVAGE, S. B. 1986 The effects of an impact velocity dependent coefficient of restitution on stresses developed by sheared granular materials. *Acta Mechanica* **63**, 15.

LUN, C. K. K. & SAVAGE, S. B. 1987 A simple kinetic theory for granular flow of rough, inelastic, spherical particles. *J. Appl. Mech.* **54**, 47.

LUN, C. K. K., SAVAGE, S. B., JEFFREY, D. J. & CHEPURNIY, N. 1984 Kinetic theories for granular flow: inelastic particles in couette flow and slightly inelastic particles in a general flowfield. *J. Fluid. Mech.* **140**, 223–256.

MAW, N., BARBER, J. R. & FAWCETT, J. N. 1981 The role of elastic tangential compliance in oblique impact. *ASME F: J. Lubrication Technol* **103**, 74.

MCNAMARA, S. & LUDING, S. 1998 Energy nonequipartition in systems of inelastic, rough spheres. *Phys. Rev. E* **58**, 2247–2250.

MIKKELSON, R., MEER, V. D., WAALE, K. V. D. & LOHSE, D. 2002 Competitive clustering in a bidisperse granular gas. *Phys. Rev. Lett.* **89**, 214301.

MIRARAI, N., HAYAKAWA, H. & NAKANISHI, H. 2002 Collisional granular flow as a micropolar fluid. *Phys. Rev. lett.* **88**, 174301.

MÖBIUS, M. B., LAUDERDALE, B. E., NAGEL, S. R. & JAEGER, H. M. 2001 Size separation of granular particles. *Nature.* **414**, 270.

MOKA, S. & NOTT, P. R. 2005 Statistics of particle velocities in dense granular flows. *Phys. Rev. Lett.* **95**, 068003.

MONTANERO, J. M., SANTOS, A., GARZO, V. & BREY, J. J. 1999 Kinetic theory of simple granular shear flows of smooth hard spheres. *J. Fluid Mech* **389**, 391.

MOON, S., SWIFT, J. & SWINNEY, H. L. 2004 Steady state velocity distribution of an oscillated garnular gas. *Phys. Rev. E* **69**, 011301.

VAN NOIJE, T. & ERNST, M. 1998 Velocity distributions in homogeneous granular fluids: the free and the heated case. *Gran. Matt* **1**, 52.

OTTINO, J. M. & KHAKHAR, D. V. 2000 Mixing and segregation of granular materials. *Annu. Rev. Fluid Mech.* **32**, 55–91.

RAPAPORT, D. C. 1980 The event scheduling problem in molecular dynamic simulation. *Journal of Comp. Physics* **34**, 184.

RAPAPORT, D. C. 1995 *The Art of Molecular Dynamics Simulation*. Cambridge: Cambridge University Press.

REIF, F. 1985 *Fundamentals of Statistical and Thermal Physics*. Singapore: McGraw-Hill.

REIS, P. M. & MULLIN, T. 2004 Granular segregation as a critical phenomenon. *Phys Rev. Lett.* **89**, 244301.

ROSATO, A., STRANDBURG, K. J., PRINZ, F. & SWENDSEN, R. H. 1987 Why the brazil nuts are on top: Size segregation of particulate matter by shaking. *Phys. Rev. Lett.* **58**, 1038–1040.

ROUYER, F. & MENON, N. 2000 Velocity fluctuations in homogeneous 2d granular gas in steady state. *Phys Rev. Lett.* **85**, 3676.

SAVAGE, S. B. 1984 The mechanics of rapid granular flows. *Adv. Appl. Mech* **24**, 289.

SELA, N. & GOLDHIRSCH, I. 1998 Hydrodynamic equations for rapid flows of smooth inelastic spheres to burnett order. *J. Fluid Mech.* **361**, 41.

Recd. on 08/2/08

TAN, M. L. & GOLDHIRSCH, I. 1997 Intercluster interactions in rapid granular shear flows. *Phys Fluids A* **9**, 856.

THEODOSOPULU, M. & DAHLER, J. S. 1974 Kinetic theory of dense polyatomic liquids. ii. the rough sphere, rigid ellipsoid, and square-well ellipsoid models. *J. Chem. Phys.* **60**, 4048.

UMBANHOWAR, P. B., MELO, F. & SWINNEY, H. L. 1996 Localized excitations in a vertically vibrated granular layer. *Nature.* **382**, 793.

VIJAYKUMAR, K. C. & ALAM, M. 2007 Velocity distribution and the effect of wall roughness in granular poiseuille flow. *Phys. Rev. E.* **75**, 051306.

WALTON, O. R. 1993 Numerical simulation of inelastic, frictional particle-particle interactions. In *Particulate two-phase flow* (ed. M. C. Roco), p. 884. Boston: Butterworth-Heinemann.